THE ROLE OF ENERGY AND SYMMETRY AT EPITAXIAL INTERFACES

AN INVESTIGATION INTO THE ROLE OF ENERGY AND SYMMETRY AT EPITAXIAL INTERFACES

By GABRIEL A. DEVENYI, B. ENG.

A Thesis Submitted to the School of Graduate Studies in Partial Fulfilment of the Requirements for the Degree Doctor of Philosophy

McMaster University © Copyright by Gabriel A. Devenyi, November 2013

McMaster University DOCTOR OF PHILOSOPHY (2013) Hamilton, Ontario (Engineering Physics)
TITLE: An Investigation into the Role of Energy and Symmetry at Epitaxial Interfaces
AUTHOR: Gabriel A. Devenyi, B.Eng. (McMaster University)
SUPERVISOR: Professor John S. Preston
NUMBER OF PAGES: xiv, 181

Abstract

Epitaxy is a key technological process for the production of thin films and nanostructures for electronic and optoelectronic devices. The epitaxial process has been traditionally studied through the lens of lattice-matched and chemically similar material systems, specifically the III-V quaternary material systems. This work investigates the role energy and symmetry play at epitaxial interfaces for cases far different than those of typical epitaxy. In the realm of energy, the impact of chemically dissimilar epitaxial interfaces was investigated, specifically between semiconductors and oxides, noble metals and oxides, and polar-on-nonpolar epitaxy. For symmetry at epitaxial interfaces, the role of symmetry breaking, through surface reconstructions and asymmetric surfaces was investigated. Investigations into energy found two key insights: 1) epitaxy is possible between materials which one would expect to be very weakly interacting (gold on oxides) and, 2) epitaxial interfaces, while promoting single crystal growth, can be weakly bonded enough to allow controlled liftoff of single crystal epitaxial thin films. Investigations into symmetry at epitaxial interfaces found three key insights: 1) intentional symmetry breaking of the growth substrate through steps can suppress twinning of zincblende thin films, 2) asymmetric (211)-oriented substrates can accommodate strain of mismatched zincblende thin films, and 3) reconstructed oxide substrates can provide unique epitaxial templates for thin films which significantly differ from their bulk lattice. The results of this investigation provide a path towards the improvement of epitaxy through the manipulation of symmetry at epitaxial surfaces, and the production of free standing thin films through the epitaxial liftoff process.

Acknowledgements

First of all, I must thank my wonderful wife Diana, she has been with me my entire academic career, now eleven years at McMaster. Her love and support has allowed me to pursue my research towards the successful thesis you see before. Our partnership in both life and academics has allowed us to both be more than the sum of our parts.

Second, I must thank my supervisor Dr. John Preston. Dr. Preston's careful balance of supervision, providing instruction and guidance when it was needed but also extensive leeway to follow my own ideas and experiments. Dr. Preston also provided the funding necessary to undertake new experiments while never worrying about expense. His urging to always "try the experiment" has driven many surprising discoveries and instilled in me a risk taking attitude to always experiment.

This work, in many senses is a collaboration. Many colleagues participated in conversations, assisted with measurements and provided their unique insights to this work. I make an effort here to name and thank my direct collaborators and those have contributed directly to my work, however this will omit many who have contributed at the lunch table or late nights at the Phoenix. Dr. Robert Hughes, my first collaborator and in many ways my first mentor, gave me the opportunity to contribute early and substantially in the work of the research group, and taught me to recognize publishable units, a skill that has resulted in the production of many articles. My collaborators and colleagues Steffi Woo, Stephen Jovanovic, Dr. Kristoffer Meinander, Vicky Jarvis, Matthew Minnick and Joshua Rideout.

Finally, I must thank my parents. Their loving and encouraging household gave me the opportunities which allowed me to develop my skills and interests and to follow my academic career. Their financial support at the start of my academic career allowed me to avoid burdening myself allowing me to keep my focus on learning.

Contents

1 Introduction **1**
1.1 Major Themes 4
1.1.1 Symmetry 4
1.1.2 Energy 5
1.2 Secondary Themes 5
1.2.1 Combined Reciprocal Space and Real Space Characterization . . 5
1.3 Organization 6

I Background **7**

2 Theory **9**
2.1 Introduction 10
2.2 Epitaxy 10
2.2.1 Homoepitaxy — Separating Thermodynamics from Kinetics . . 10
2.2.2 Heteroepitaxy 13
2.2.3 Clusters and Nucleation 17
2.3 Surface Reconstructions 21
2.3.1 Cuts Along High-index Planes 24
2.3.2 Thermodynamics, Kinetics and Stability of Surface Reconstructions 26
2.3.3 Nomenclature for Surface Reconstructions 27
2.4 Atomic Bonding — Attraction Between Atoms 30

3 Experimental **33**
3.1 Introduction 34
3.2 X-Ray 34

3.2.1 2DXRD — Reciprocal Space Mapping 37
3.2.2 High Resolution XRD 46
3.3 Electron Microscopy 48
3.3.1 SEM 50
3.3.2 TEM 52
3.3.3 STEM 55
3.4 Growth Techniques 56
3.4.1 PLD 57
3.4.2 MBE 59

II III-V Materials on Silicon 61

4 The Role of Vicinal Surfaces in Epitaxial Twin Formation 63
4.1 Introduction 64
4.2 Background 65
4.3 Experimental 66
4.4 Results 67
4.5 Discussion 73
4.6 Implications for Symmetry and Energy at Epitaxial Surfaces 78

5 Tilted Epitaxy on (211) Oriented Substrates 81
5.1 Introduction 82
5.2 Background 82
5.3 Experimental 83
5.4 Results 84
5.5 Discussion 88
5.6 Implications for Symmetry and Energy at Epitaxial Surfaces 91

III Semiconductors on Oxide Substrates 93

6 CdTe Growth on Sapphire Substrates and Liftoff Phenomenon 95
6.1 Introduction 96
6.2 Background 96
6.3 Experimental 97

6.4 Results . . . 98
6.4.1 Epitaxial Interface Characterization . . . 102
6.5 Discussion . . . 104
6.6 Implications for Symmetry and Energy at Epitaxial Surfaces . . . 105

7 CdTe Growth on Reconstructed $SrTiO_3$ 107
7.1 Introduction . . . 108
7.2 Experimental . . . 108
7.3 Results and Discussion . . . 109
7.4 Implications for Symmetry and Energy at Epitaxial Surfaces . . . 118

8 CdTe Nanowire Growth on Sapphire 119
8.1 Introduction . . . 120
8.2 Experimental . . . 120
8.3 Results and Discussion . . . 121
8.4 Implications for Symmetry and Energy at Epitaxial Surfaces . . . 131

IV Noble Metals on Oxides 133

9 Nanostructured Gold on Spinel 135
9.1 Introduction . . . 136
9.2 Experimental . . . 136
9.3 Results and Discussion . . . 137
9.4 Implications for Symmetry and Energy at Epitaxial Surfaces . . . 146

V Closing Discussions 147

10 Future Work 149
10.1 Surface Reconstructions . . . 150
10.1.1 Twinning Control . . . 150
10.1.2 Lattice Matched Growth on Reconstructions . . . 150
10.2 Epitaxial Liftoff . . . 151
10.2.1 Other II-VI Liftoff . . . 151
10.2.2 III-V Liftoff . . . 152

10.2.3 Physics of Liftoff 153
10.2.4 Engineering of Liftoff 153
10.3 Gold on Spinel 153

11 Conclusions 155

A Lattice Matching Calculations 177

List of Figures

1.1 Bandgap versus lattice constant . . . 3

2.1 Kinetic Processes of atoms on surfaces . . . 11
2.2 Unit cell strain visualization . . . 14
2.3 Critical thickness dependence on strain . . . 15
2.4 Atomic model of polar on non-polar epitaxy . . . 16
2.5 Young's equation . . . 19
2.6 Nucleation phase diagram of surface energy and strain . . . 20
2.7 Simple surface reconstruction . . . 22
2.8 Silicon dimer surface reconstruction . . . 23
2.9 Silicon single and double step surface reconstructions . . . 25
2.10 Terrace length of reconstructed stepped surface due to offcut of α. . . . 25
2.11 Silicon surface reconstruction phase diagram . . . 27
2.12 2D Surface Nets . . . 28
2.13 Examples of surface reconstructions . . . 29
2.14 Energy potentials between two atoms . . . 31

3.1 Ewald sphere . . . 36
3.2 Typical 2DXRD experimental implementation . . . 38
3.3 X-Ray Beam Width . . . 40
3.4 Example 2DXRD frame . . . 41
3.5 Mapping of pole sphere to pole figure . . . 43
3.6 Comparison of WinWulff simulation and experimental single crystal silicon pole figure. . . . 44
3.7 Example simulated pole figures . . . 45
3.8 Electron interactions with materials . . . 49

3.9 PLD chamber schematic . . . 57

4.1 Pole figures of nominal and vicinal substrates . . . 68
4.2 Simulated pole figure of twinned III-V on nominal silicon . . . 69
4.3 Integrated x-ray intensities from pole figures . . . 70
4.4 TEM images of III-V on silicon . . . 71
4.5 TEM of GaSb on silicon . . . 72
4.6 Model of twins on a (100) surface . . . 74

5.1 Measured and simulated pole figure of thin film on 211 silicon . . . 84
5.2 TEM of thin film on 211 silicon . . . 86
5.3 Atomic model of tilted thin film on 211 silicon . . . 89
5.4 Colourmap of tilt and intrinsic lattice mismatch of thin films on 211 substrates . . . 90

6.1 Geometric model of cubic CdTe crystal structure fit on hexagonal c-plane sapphire surface. . . . 97
6.2 Toppled CdTe nanowire . . . 99
6.3 Generalized CdTe liftoff process . . . 100
6.4 a) As-grown on sapphire and b) released on epoxy carrier CdTe pole figures, area of scaled intensity shows secondary phases present from twinning. . . . 101
6.5 CdTe on sapphire STEM images used for polarity determination. . . . 103
6.6 CdTe on sapphire STEM images used for polarity determination. . . . 103

7.1 AFM of $SrTiO_3$ surfaces . . . 109
7.2 Pole figures of CdTe grown on $SrTiO_3$ . . . 110
7.3 Simulated pole figures of CdTe on $SrTiO_3$ surfaces . . . 111
7.4 CdTe grains on (100) $SrTiO_3$ . . . 112
7.5 Simulated pole figure of CdTe on reconstructed $SrTiO_3$ . . . 112
7.6 Projection of (211) CdTe unit cell on $SrTiO_3$ surface . . . 114
7.7 CdTe on c(4×2) $SrTiO_3$ surface . . . 115
7.8 CdTe on c(6×2) $SrTiO_3$ surface . . . 116

8.1 SEMs of seeds and resulting wires. . . . 122
8.2 Pole figure of CdTe nanowires . . . 122

8.3 SEM image of CdTe nanowires . . . 123
8.4 CdTe nanowire dimension colourmap . . . 124
8.5 CdTe nanowire lateral growth . . . 124
8.6 CdTe nanowires with slanted tops . . . 125
8.7 SEM image showing tapered CdTe nanowires. . . . 125
8.8 Simulated CdTe nanowire dimension distributions . . . 128

9.1 SEM images of gold nanostructures . . . 138
9.2 SEM of gold nanostructure growth progression . . . 139
9.3 Model of gold nanostructure faceting . . . 142
9.4 Simulated gold nanostructure growth . . . 142
9.5 Simulations of square and rectangular base gold nanostructures . . . 144
9.6 Comparison of AFM and simulated gold nanostructure topography . . . 145

10.1 Pre- and post-liftoff ZnTe pole figures. . . . 152

List of Abbreviations and Symbols

2DXRD Two Dimensional X-ray Diffraction

γ Surface Energy

a,b,c Crystal Unit Cell Lengths

APB Anti-Phase Boundary

APD Anti-Phase Domain

d Crystal Plane Spacing

FIB Focused Ion Beam

h,k,l Reciprocal Crystal Indices

HAADF High Angle Annular Dark Field

HRXRD High Resolution X-ray Diffraction

MBE Molecular Beam Epitaxy

PLD Pulsed Laser Deposition

RHEED Reflection High Energy Electron Diffraction

SAD Selected Area Diffraction

SCCM Standard Cubic Centimetres per Minute

SEM Scanning Electron Microscopy

SFE Stacking Fault Energy

SNR Signal to Noise Ratio

STEM Scanning Transmission Electron Microscopy

TEM Transmission Electron Microscopy

VLS Vapour Liquid Solid

XRD X-ray Diffraction

Declaration of Academic Achievement

The work presented here is the result of research performed by myself during the years 2009–2013. Results which have substantial contributions from other authors are clearly prefaced and the contributions of those authors are indicated.

Chapter 1

Introduction

Epitaxy has been a dominant technological feature since near the inception of the semiconductor age. It has also been intimately entwined with the dominant semiconductor up till the present day, silicon. Silicon has been a dominant player in almost every field of semiconductor research for the better part of 40 years, becoming the most well understood material in the world. This focus on silicon has also greatly influenced the thinking of what were at the time fledgling fields, most notably epitaxy. *Epi-taxis* or “above — in an ordered manner” is the Greek root of the term epitaxy and as it is originally defined, it has been narrowly interpreted by most of the research field. Silicon on silicon epitaxy, or homoepitaxy, has been the dominant type of epitaxy both for research and production, due to its relevance to semiconductor chip manufacturing. This idea of the ‘ideal’ epitaxy as modelled by silicon homoepitaxy has pervaded the thinking of research into the field, with the material systems being most similar as a result being the most researched, and the most successful.

One of the material systems most similar to homoeptiaxy (besides other homoepitaxy) are the III-V group semiconductors, specifically the Al/Ga/In-P/As/Sb binary/ternary/quaternary family as in Figure 1.1. These zincblende semiconductors through the manipulation of exact atomic concentration, can be grown from exactly lattice matched to strongly mismatched. These material systems all have covalent or primarily covalent bonds with strongly preferred atomic sites for the atomic species. When parameters are optimized, epitaxial growth in such systems is orientationally commensurate with the underlying substrate and dominated by strain effects.

Beyond the III-V homologous growth systems, the next most investigated epitaxial process is when these materials are grown on silicon. In addition to the always-present issue of strain due to the intrinsic lattice mismatch between the III-V family and silicon, the diamond structure of silicon results in an issue of polar (zincblende, bonds with non-equal electron sharing) on non-polar (diamond, bonds with equal electron sharing) epitaxy[2] where group III and group V atoms cannot differentiate between sites on the silicon surface. Such site non-specificity has been an issue of great interest to the epitaxy research community resulting in numerous attempts, some successful[2] to improve growth of such a chemically dissimilar system.

Outside the extensive research into the epitaxy of silicon and the III-V systems, work into epitaxy has mostly been on a material-by-material basis. Material systems of interest are examined on an issue-by-issue basis with the goal of producing high quality material for some application, rather than examining the generalized epitaxy

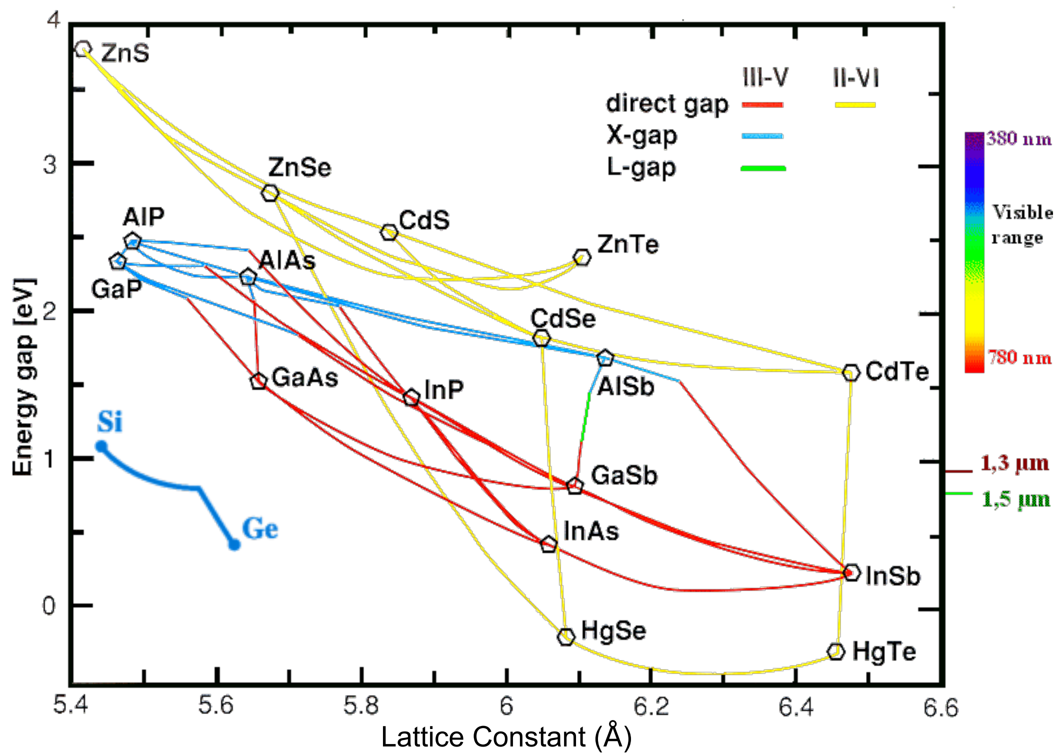

Figure 1.1: Bandgap versus lattice constant for the most common semiconductors (used with permission after [1]).

phenomenon. In this work, the goal has been to expand the understanding of epitaxy through an experimental exploration of several model systems which are corner cases of epitaxy, and to show other conditions under which high quality epitaxy can occur. Through this work, two key themes were examined in epitaxial systems, the role of symmetry and the role of energy at epitaxial interfaces. These themes were examined through investigations into three model material systems, III-V semiconductors on silicon, II-VI semiconductors on crystalline oxides, and noble metals on crystalline oxides. Investigations into III-V semiconductors on silicon focused on the role of vicinal surfaces, surface reconstructions, and higher order crystal surfaces. Vicinal (or offcut) surfaces of substrates, truncated and reconstructed, were found to have a strong effect on twinning during epitaxial growth, a potential method of improving quality of material growth. (211), a higher order substrate orientation was found to allow accommodation of strain by tilting of a growing epitaxial layer. Investigations into II-VI semiconductors concentrated on the role of surface reconstructions, and the role of bond strength in epitaxial interfaces. A new epitaxial relationship between temperature stable surface reconstruction and CdTe was observed and atomically modelled. Such stable surface reconstructions may offer a new route for lattice matched epitaxial growth. In addition, growths of CdTe on sapphire substrates were found to show a unique liftoff phenomenon, where single crystal films are weakly bonded to the substrate and can be removed while maintaining crystalinity. Finally, investigations into noble metals on oxide surfaces concentrated on the properties of epitaxy in the weak bonding regime. Epitaxial growth of gold on spinel, a complex oxide, was found to be possible, despite the weak reactivity of both the noble metal and the oxide substrate. The results from these investigations and the main contribution of this work is to show that epitaxy is possible for symmetrically and chemically dissimilar model systems, and to experimentally examine the implications to epitaxy that such systems have.

1.1 Major Themes

1.1.1 Symmetry

The 2D (and as we shall later see sometimes 3D) interface that separates the epitaxial substrate from the growing crystal has a symmetry relationship which relates the

substrate to the crystal. These surface symmetries are different than the bulk symmetry of the substrate and crystal. In the simplest treatment of surfaces, the surface of a given substrate is simply a truncation of the crystal in a given orientation, exposing a plane of atoms which then present a subsymmetry of the bulk crystal. Any truncation through a bulk crystal is highly likely to be unstable, since the once buried atoms are now exposed at a surface, this surface can resolve this instability in a variety of ways. As will be seen later there are many complications to this model and it is in these complications that we find changes in symmetry, breaks in symmetry and distortions of this 2D surface into a more complex 3D interface. It is these changes to the surface symmetry, and its interaction with the growing crystal which have profound and useful implications for epitaxy. The first major theme investigates the implications of unique interface symmetries, broken symmetries and 3D interfaces on the epitaxial process.

1.1.2 Energy

While the symmetry of a surface describes the spatial distribution of the potential landscape presented to a growing epitaxial crystal, energy describes the magnitude of that potential landscape. Strong energy landscapes cause the symmetry of a given substrate to have its influence felt strongly, while a weak landscape can have a subtle effect on growth. Whether atoms are bonded via physisorption (Van der Waals), covalent bonding, or ionic attraction determines the magnitude of the interface landscape. The magnitude of the energy landscape at the epitaxial interface can vary over a large range, and the role of these strengths has not been examined extensively. The second major theme of this work investigates the implications of energy landscapes outside the typical heteroepitaxy regime, specifically relating to the weaker energies.

1.2 Secondary Themes

1.2.1 Combined Reciprocal Space and Real Space Characterization

The investigations into epitaxy discussed throughout this thesis have relied upon a variety of techniques to reveal the patterns behind these processes. The most fruitful of the techniques utilized in this work has been the combined use of reciprocal space

mapping via 2DXRD and the direct imaging of samples using TEM/STEM. These techniques, when used individually, often lead to ambiguity in the results. STEM/TEM, being a small-area sampling technique can frequently miss information, or cause false interpretations of "common" results, when a given sample may be unique or atypical. Similarly, the use of reciprocal space mapping alone gives a picture which convolves all of the data in the sampling area together, providing little insight about its spatial distribution. The most effective example of this combined technique revealing features is the examination of twinning on reconstructed vicinal substrates in Section 4.1, these material systems have been examined many times before in literature, but only the combined examination presented here captured and effectively explained the role the substrate offcut played in twin formation. When these two techniques are combined, the two datasets must be successfully reconciled for a given model of the underlying system to be coherent. Such consistency requirements allow competing explanations to be discriminated from one another based on predictions they make about the data, leading to more complete and less ambiguous models. Such a combination of techniques has also encouraged collaboration. One cannot be an expert in the operation and interpretation of both measurement systems without compromising the time spent on research into the research topic originally intended for investigation.

1.3 Organization

This thesis is organized into four broad parts. In the first part, the theoretical and experimental background necessary for the understanding and reproduction of the thesis is provided, as well as references to provide comprehensive background. In part two, investigations involving the growth of III-V semiconductors on silicon substrates is examined, in the context of symmetry and symmetry breaking at epitaxial interfaces. In part three, the growth of CdTe on single crystal oxide substrates is examined in the context of chemically dissimilar interfaces, and the role of surface reconstructions. In fourth part, epitaxial growth of single crystal noble metals is examined on oxide substrates in the context of weak bonded epitaxy. Finally, future work is proposed in each of these respective investigations and conclusions are drawn based on the combined results of these investigations.

Part I

Background

Chapter 2

Theory

2.1 Introduction

As this thesis is primarily an exploration of epitaxial interfaces using a wide array of experimental techniques, the background material here will cover the theoretical concepts that are regularly drawn upon to support the growth models presented elsewhere. Models presented later in the document are primarily of a conceptual nature and as such background here will also be presented in that manner. Mathematics will be used where applicable but will be generally avoided, as the restricted assumptions are of little use to the work presented later.

There are a few key theoretical concepts which must be understood to best describe the expanded epitaxial model proposed here. The first, and most integral to the discussion is an examination of the model of epitaxy as now defined in the literature. This is integral to differentiate where the material systems examined diverge from the idealized models presented in the literature. As part of the examination of epitaxy, particular attention will be given to nucleation and clusters on surfaces as this examination hinges on the role of the epitaxial interface. Beyond epitaxy, the other key subjects which require background exposition are surface reconstructions, which describe the properties of the substrate side of the epitaxial interface, and atomic bonding, the connections which reach across the epitaxial interface.

2.2 Epitaxy

2.2.1 Homoepitaxy — Separating Thermodynamics from Kinetics

The most basic form of epitaxy that can be conceived of is homoepitaxy, that is, where a material is grown on an existing single crystal of that same material. In this growth process, the crystal structure, lattice constants and chemistry are identical across the epitaxial interface. Despite this ideal situation, the growth of perfect homoepitaxial crystals is not guaranteed. The fact that a homoepitaxial growth can be defective in a number of ways is due to the difference between the thermodynamics and kinetics of the epitaxial growth process. Thermodynamically, one would expect that the lowest energy state for the system would be the continuation of the existing single crystal via

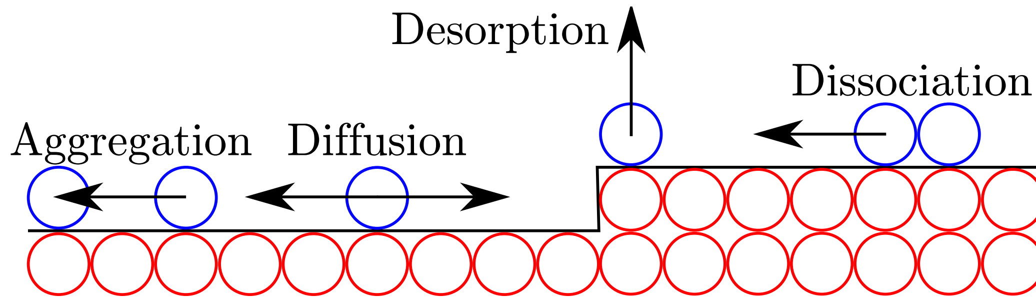

Figure 2.1: Common kinetic processes in epitaxy with reaction rates of the Arrhenius form.

the homoepitaxial growth process, however, due to kinetics, the exact conditions of growth process can have a substantial impact on the resulting crystal.

The homoepitaxial growth process is an excellent model system to separate the role of thermodynamics in growth from that of the kinetics. Kinetics refers to the role time plays in an epitaxial growth process, usually examined via rates. There are two fundamental kinetic rates involved in epitaxial growth, those which can be directly controlled and those which are primarily properties of the material system and can only be indirectly influenced by the experimenter. The most important kinetic processes in epitaxy are shown as Figure 2.1.

The most common experimentally controlled rates in an epitaxial growth are the rate of addition of atoms to the growth interface, and the indirect rates controlled by the temperature of the substrate. The rate of atom addition, or the impingement rate is a key parameter and in homoepitaxial growth, can reveal the role kinetics plays in growth. If the rate at which atoms are added to an epitaxial interface is extremely high, the atoms will have no time to move towards their thermodynamically preferred (global minimum) location. The resulting material that grows will consist of layers of atoms stacked randomly where they first hit the substrate or in local energy minimia, and are immediately covered by more atoms. Such a configuration is not an epitaxial growth, rather the film is likely to be amorphous or fine-grained polycrystalline, yet there are no material limitations per-se that are causing the poor growth, it is purely kinetic. As the impingement rate is lowered, adatoms are allowed more time to move via diffusion, they may register in some regions, but not in others, resulting in a partially crystalline growth. As the deposition rate is further reduced, depending upon the material, the film may grow in a fully crystalline nature, but be twinned or contain stacking faults. The bonding along {111} directions in a zincblende crystal is susceptible to faults due

to their rotational symmetry, the exact susceptibility is known by the Stacking Fault Energy (SFE)[3]. Stacking fault energies in semiconductor materials vary from as low as single digit mJ/m^2 (CdTe 9 mJ/m^2), to over 200 mJ/m^2 (C 285 mJ/m^2)[4]. This energy is a measure of the cost of making such a defect in a crystal, so crystals with low SFE are very susceptible to twinning during growth. At yet lower impingement rates the adatoms have time to find their low energy states with respect to twins, finally arriving at a single crystal.

While adjustment of the directly controlled deposition rate seems to be severely limited by defect formation and random stacking of adatoms, there are large number of kinetic processes during growth that can be indirectly influenced by an experimenter through the control of temperature. The other kinetic processes fundamental to growth are all of the Arrhenius type, as shown in Equation (2.1). The Arrhenius rates are exponential, with a pre-factor (A_0) and an activation energy (E_0). For crystalline surfaces, the pre-factor can be further defined as an attempt frequency or attempt rate (v) and the surface lattice spacing (a) as in Equation (2.2)[5]. As such, these processes have an exponential dependence on the temperature at which growth occurs.

$$A = A_0 e^{-\frac{E_0}{kT}} \tag{2.1}$$

$$A = -va^2 e^{-\frac{E_0}{kT}} \tag{2.2}$$

Among the other kinetic processes involved in growth the most common are surface diffusion, bulk diffusion, desorption, aggregation(nucleation) and dissociation. Through the increase in temperature the rates of all of these processes increase (except nucleation, which decreases with temperature). This has a strong impact on the epitaxial process. The key kinetic factor to the improvement of epitaxial growth is the increase in the surface diffusion rate. Surface diffusion of adatoms during growth is the process by which a newly adsorbed atom from the impinging atoms finds its lowest energy position on the epitaxial surface. Increases in temperature increase the rate at which these adatoms move, increasing the probability that they will find their lowest energy position before they are encapsulated by additional atoms. While increases in temperature will improve the mobility of adatoms, increases in temperature also increase other processes. Bulk diffusion is the process by which adatoms at the epitaxial interface diffuse into the substrate through exchange with other atoms or travel interstitially. In homoepitaxy this process is irrelevant, but in any chemically dissimilar growth such

a process distorts the sharp interface, which is generally not preferred. Furthermore, as temperature increases, adatoms can begin to desorb, leaving the epitaxial interface, slowing growth and under extreme circumstances, the substrate itself can also begin to lose atoms. Finally, at very high surface diffusion rates, adatoms may never attach to others, preventing nucleation of new layers of crystal.

The kinetics of growth are thus balanced between the impingement rate, determined by the delivery of atoms to the epitaxial interface, and a temperature that is high enough to ensure single crystal growth, but not too high to cause breakdown of the epitaxial process, which is a delicate balance.

2.2.2 Heteroepitaxy

Heteroepitaxy covers a wide range of A on B epitaxy systems, as such, the following treatment will start from the basics established in homoepitaxy and gradually add the levels of complexity found in real-world systems and consider how they add to the model.

2.2.2.1 Strained Heteroepitaxy

The first step in the complication from homoepitaxy to heteroepitaxy is to introduce a difference in the lattice constants between the substrate and the growing epitaxial crystal, while maintaining the crystal structures and chemical composition. When there is a strong chemical bond between the two crystals across the interface, both feel a distortion from their ideal crystal structures, one is compressed slightly, while the other is tensioned[6]. Nature has provided an ideal model system which perfectly fits these requirements, the $\mathrm{Si}_{1-x}\mathrm{Ge}_x$ system grown on silicon[7]. In $\mathrm{Si}_{1-x}\mathrm{Ge}_x$, germanium substitutes into the silicon lattice randomly, maintaining the same valence and diamond structure. The lattice constant varies quadratically between silicon and germanium as in Equation (2.3).

$$a_{Si_{1-x}Ge_x} = 0.5431 + 0.01992x + 0.0002733x^2 \tag{2.3}$$

The fundamental physical parameter describing such mismatched system is strain, that is, the distortion of atoms from the thermodynamic equilibrium positions, due to bonding to a mismatched substrate. Strain can be conceptualized as energy stored within the stretched bonds of the epitaxial layer, like a spring displaced from its

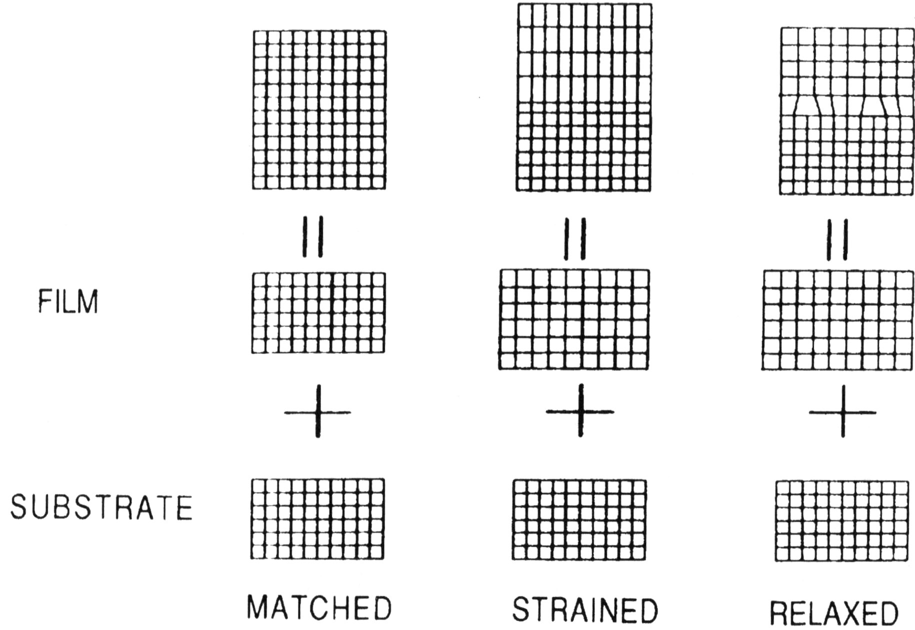

Figure 2.2: Effects of strain on unit cell of epitaxial crystal a) matched, no strain b) strained, but pseudomorphic, lattice is only distorted c) highly strained resulting in dislocations to relax strain (used with permission from [8]).

equilibrium position, increasing the internal energy within the epitaxial crystal. The difference between lattice constants of crystals is expressed as the lattice mismatch as in Equation (2.4), where a_f is the film lattice constant and a_s is the substrate lattice constant. Negative values indicate that the growing layer is strained in tension by bonding to the substrate, while positive values indicate that growing layer is strained in compression by bonding to the substrate.

$$f = \frac{a_f - a_s}{a_s} \tag{2.4}$$

Through the examination of the $Si_{1-x}Ge_x$ system grown on silicon, the effect of pure compressive strain on an epitaxial process has been examined. As an epitaxial crystal of $Si_{1-x}Ge_x$ is grown on a silicon substrate, the strain energy in the crystal increases with thickness. The growing epitaxial crystal maintains the lateral lattice constant of the substrate, and conserves its volume by changing its vertical lattice constant, this is known as pseudomorphic growth. Beyond a certain point, the energy required to add another layer of strained crystal is too much, and the strain is relieved through the introduction of defects in the form of dislocations. In a dislocation, the bonding

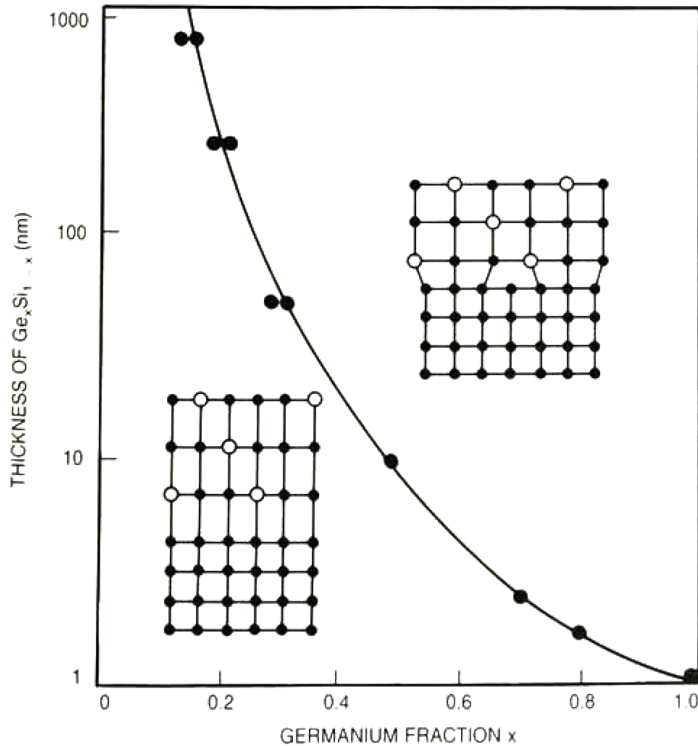

Figure 2.3: Critical thickness versus germanium fraction of $Si_{1-x}Ge_x$, showing regions of pseudomorphic growth and relaxed growth by dislocations (Reprinted with permission from Bean *et al.*[9]. Copyright 1986, American Institute of Physics).

between the epitaxial crystal and the substrate is broken to allow the crystal to expand, leaving a dangling bond at the substrate. Such a process is random so defects are located randomly at the interface. The exact thickness where a pseudomorphic growth will introduce defects in order to relieve strain is known as the critical thickness and is dependent upon several factors. These factors include the strength of the bonds across the epitaxial interface, the bond strength within the epitaxial layer, and the energetic cost of forming a dislocation in terms of atomic movement and dangling bonds. These last two factors are impacted by kinetics as there is often a large activation energy associated with defect formation. Figure 2.3 shows the experimental curve for the model system $Si_{1-x}Ge_x$ grown on Si including the dividing line between pseudomorphic and dislocated growth due to strain. The critical thickness model is qualitatively similar for other systems that have similar growth properties.

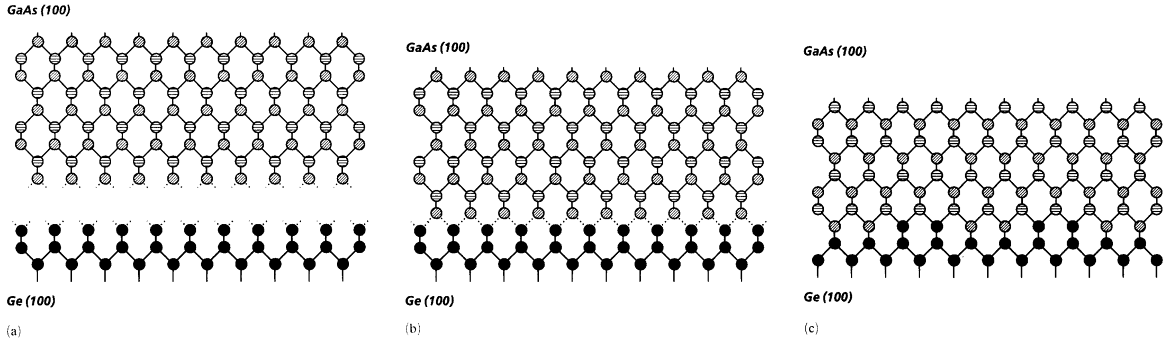

Figure 2.4: GaAs (polar) on Ge (non-polar) ideal epitaxy model a) separate crystals b) bonding showing surface charge c) atomic exchange resolving surface charge (used with permission from [11]).

2.2.2.2 Chemically Dissimilar Heteroepitaxy

On the other side of the heteroepitaxy spectrum are those epitaxial growths that have commensurate crystal structures but differ in their chemical compositions. There are few material systems which provide an ideal model for a lattice matched (zero strain), but chemically dissimilar epitaxial growth. The most well characterized model system available is a lattice matched III-V semiconductor on germanium, specifically GaAs, which has a small ($<$0.1%) lattice mismatch. GaAs is a binary semiconductor with the zincblende crystal structure, which is a cubic crystal identical to silicon and germanium's diamond structure, but with a two-atom basis (Ga, As). The crystal is covalently bonded as with Si, but has a $\sim$30% ionic character due to differences in electronegativity[10].

The zincblende crystal structure is due to two atoms of different valence (group III-group V), which forms a polar crystal structure, with the group-III atom supplying three electrons and the group-V atom supplying five electrons to the bonding structure. The two-atom basis of zincblende breaks the diamond crystal structure such that the structure is no longer centrosymmetric, meaning that opposite directions in the crystal are no longer symmetrically equivalent. This breaking of symmetry in the crystal means that the ordering of the group-III and group-V atoms at the epitaxial interface matters for crystal growth. This problem is known as "polar-on-nonpolar" epitaxy[2, 11].

If the truncated crystal surface of such a polar semiconductor is brought towards the truncated surface of a germanium crystal as in Figure 2.4, the interface that results,

while all bonds will be satisfied with no strain, will not be satisfied electronically. There will be a deficit (group-III) or excess (group-V) of electrons participating in bonding at the interface, leaving a layer of excess charge. Such excess charge would be massive as it forms across the entire interface. During growth of a crystal, rather than the thought experiment just discussed, we could expect that the surface charge would be a driving force for an atomic rearrangement at the interface as in Figure 2.4c. Experimental results have shown that several different rearrangements are possible. The interface region can become three dimensional with the substrate and epitaxial layer atoms swapping to balance the number of excess and deficient bonds, resulting in an overall neutral charge. Defects of different types can also form, resulting in dangling bonds which can compensate charge. Some orientations of the crystal substrate, such as (211) offer unique lattice sites such that the charge neutrality is maintained automatically, which has motivated some of the work presented in Section 5.1.

In addition to issues of charge neutrality at chemically dissimilar ideal epitaxial interfaces, there is a second issue. This issue only arises in practical growth situations, because real substrates are never perfectly aligned with their intended crystal orientation. These substrates, when offcut even the smallest amount from the intended orientation, will reconstruct into terraces of the primary crystal orientation separated by atomic height steps, the details of this process will be covered in Section 2.3. When those steps are single steps, that is, a/4 in height, adjacent terraces expose different sublattices of the diamond structure and these two sublattices have their exposed bonds rotated 90° relative to each other. When a crystal is grown atop such a substrate, the growth on adjacent crystals will also be offset by a/4. While such an offset is not detrimental to the substrate itself, the zincblende crystal structure with two different atoms, when offset by the same amount, will result in a misalignment of the growing crystal at the step edges. The step edge will contain III-III or V-V bonds, a section known as an anti-phase boundary, a defect that causes significant electrical defects and unintentional doping due to uncompensated bonds. Sufficient care must be taken when preparing substrates (as noted later in Section 2.3) to avoid these highly detrimental anti-phase boundaries.

2.2.3 Clusters and Nucleation

As will be noted throughout this document, the key factor in the growth of epitaxial crystals is the properties of the epitaxial interface. The two generalized properties

that impact this interface are the energy and symmetry at the interface. The initial stages of the epitaxial growth process is a key step which reveals the complex interplay of strain, energy and symmetry, through the form of the nucleation of the epitaxial crystal.

A key qualitative measure of the affinity of a given crystal to grow on another crystal is what is termed the nucleation mode of the epitaxial crystal. Qualitatively, the nucleation mode of a given epitaxial crystal A on a substrate B, describes the affinity for the atoms in A to wet (spread out and contact) the substrate versus sticking to each other. The wetting and dewetting of a given system is described by Young's equation, as in Equation (2.5). Young's equation describes the balance of three energies, the solid-liquid surface energy (γ_{SL}), the solid-gas surface energy (γ_{SG}) and the liquid-gas surface energy (γ_{LG}), through a parameter denoted the contact angle. The contact angle is the key parameter which determines wetting characteristics of a system.

$$\gamma_{SL} + \gamma_{LG} \cos \theta_c = \gamma_{SG} \tag{2.5}$$

Young's equation can be visualized as an isotropic droplet of the epitaxial crystal material sitting atop a substrate, making some contact angle with the substrate, as in Figure 2.5a. Contact angles of less than 90° are denoted as wetting a surface, while angles greater than 90° are denoted as dewetting a surface. Young's equation assumes the wetting material is isotropic, that is, has no preferred direction or orientation. Such a situation is common for polymers, liquids, and materials heated above their melting point. For crystalline materials, there are preferred close packed surfaces which have lower energy. These close packed surfaces provide an additional energy consideration to equilibrium shapes which now form Wulff shapes, balancing surface interface energies and the energy of exposed crystal facets[12] as visualized in Figure 2.5b.

Since Young's equation (and Wulff shapes) describe the preference of a given material to stick to a substrate or to itself, such wetting and dewetting can naturally be extended to describe the modes of growth when a film is deposited onto a substrate. During epitaxial nucleation, incoming atomic material is incorporated into thin films as one of three modes: island nucleation (Volmer–Weber), layer-by-layer nucleation (Frank–van der Merwe), and layer plus island (Stranski-Krastanov) or mixed-mode nucleation[12], as in Figure 2.6. These modes describe the preference for the deposited atoms to spread out (wet) the growth interface or bunch up (dewet).

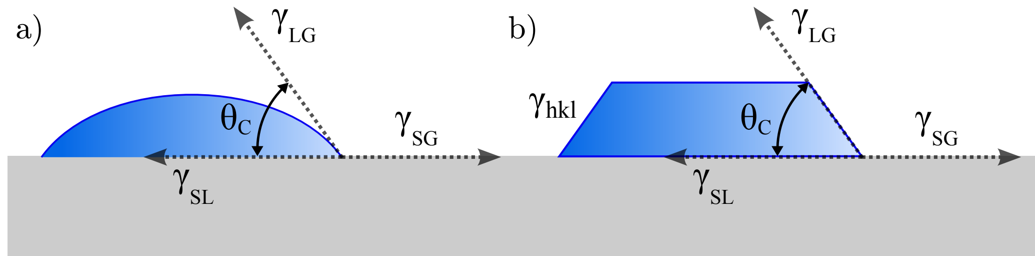

Figure 2.5: a) Young's equation visualized as an isotropic droplet sitting atop a substrate, with surface energies and contact angle labelled b) Minimum surface energy Wulff shape of a crystalline material atop a substrate, with surface energies, contact angle and crystal surface energy (after [13]).

The energies in Young's equation are intrinsic to the crystal and chemical relationship between the epitaxial crystal and the substrate, as well as possibly the overlying gas. Strain and chemical bonding are the two primary factors which influence the energy parameters which participate in the nucleation process. The regions have been mapped experimentally for several model systems, both chemically similar and strained, and the chemically dissimilar but unstrained, as shown in Figure 2.6. Layer-by-layer nucleation and growth is most readily achieved when the epitaxial crystal and substrate are chemically compatible and have minimal strain[12]. For chemically incompatible systems, nucleation is always island nucleation, as the epitaxial crystal would rather bond to itself than the substrate. With increasing strain, nucleation can begin as layer by layer, but may transition to island after several layers. Mixed mode growth is also common where the deposited atoms prefer to bond to the substrate much more strongly than to each other, resulting in an initial flat layer followed by island formation[12]. Nucleation modes also have a dependence on the rate of material deposition and the temperature of the substrate. Systems which would prefer to form islands during nucleation can be restricted to layer-like growth modes by increasing the deposition rate or reducing the temperature.

For a generalized epitaxial system, there are other factors not considered as part of this simple model. These nucleation modes do not consider the kinetics of the growth process. If atoms are delivered too quickly nucleation can form islands regardless of the predictions of Young's equation. The conditions for optimal nucleation may be different than those of growth, especially in the case of mixed-mode, where changes in growth parameters during growth may lead to better outcomes overall.

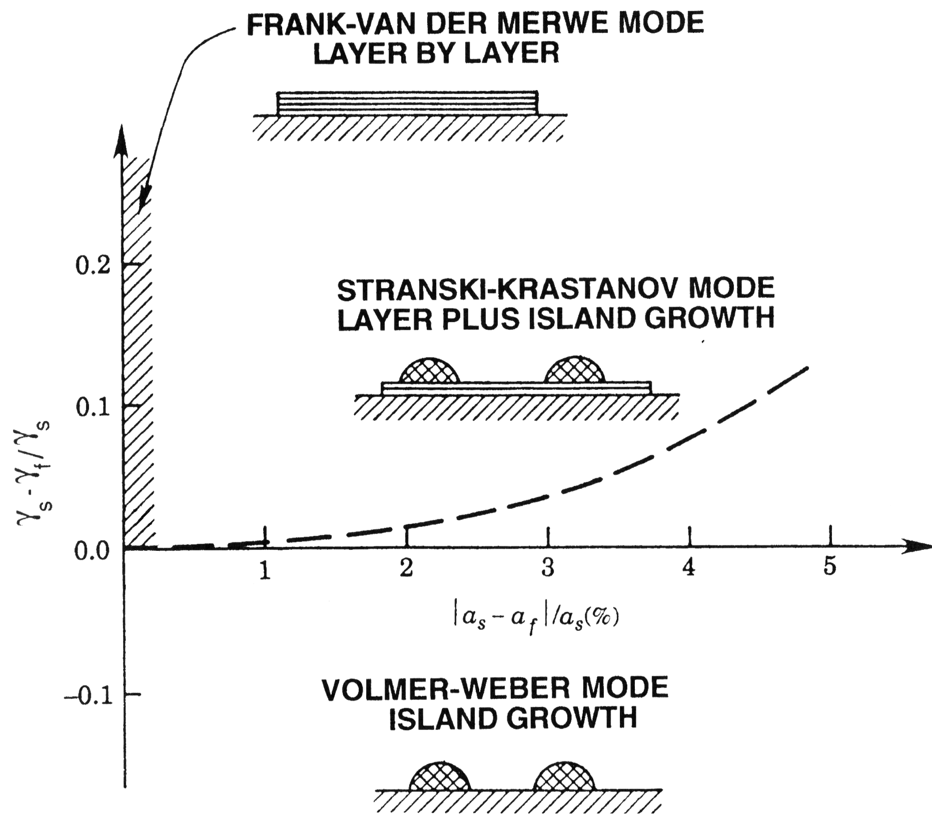

Figure 2.6: Phase diagram showing regions of different thin film nucleation modes, plotted with axes of lattice mismatch (strain) and ratio of surface energies (used with permission after [8]).

2.3 Surface Reconstructions

If one were to consider a crystal of infinite size, and then cut it along any direction, the resulting truncated crystal surface would have a very high energy surface. Bonds will be unsatisfied, there is likely to be an unbalanced charge, and the surrounding environment for each surface atom will be different than when it was in the bulk. This high energy condition is not the equilibrium state and must be resolved. The resolution of this high energy state that results when surfaces of a single crystal are exposed is called the surface reconstruction. While the name surface reconstruction implies changes to just the surface atoms, a surface reconstruction can extend a number of atomic layers into the crystal. Thus, the changes that occur at the surface of a crystal can result in a very different interface than the bulk crystal for the purposes of epitaxy.

The atoms on the surface of a newly cleaved crystal have a number of options for resolving their high energy configuration. The simplest of options for atoms in those high energy states to reduce their energy, is to move, that is, to change its position relative to other atoms. These movements happen both the in-plane and out-of-plane directions. Both atomic translations can cause additional shifts in the atomic layers below the surface. Both in-plane and out-of-plane atomic movement breaks the bulk symmetry of the original crystal, resulting in a surface with lower symmetry. In extreme cases, atoms can migrate and form islands or otherwise cause faceting on the surface in order to minimize energy[14, 15]. A schematic example of the simple atomic movement and relaxation for surface reconstructions as shown in Figure 2.7.

A more complex response resulting in a surface reconstruction that can arise is a change in the bonding in the upper layers of the crystal. Dimers and higher order bonding can form at the surface of the crystal, partially resolving the dangling bonds present on the surface. This dimerization of the surface can reduce the chemical activity of the surface since the electronic structure has been satisfied internally to the crystal[14]. One common example of the dimerization is that of the silicon (100) surface, as shown in Figure 2.8.

Finally, a surface can reconstruct by ejecting some of the atoms which originally formed the surface. The removal of such atoms can allow what was once a close-packed surface to have less density than the parent crystal lattice. This is typical in reconstructions of materials where gaseous are materials integrated into the lattice.

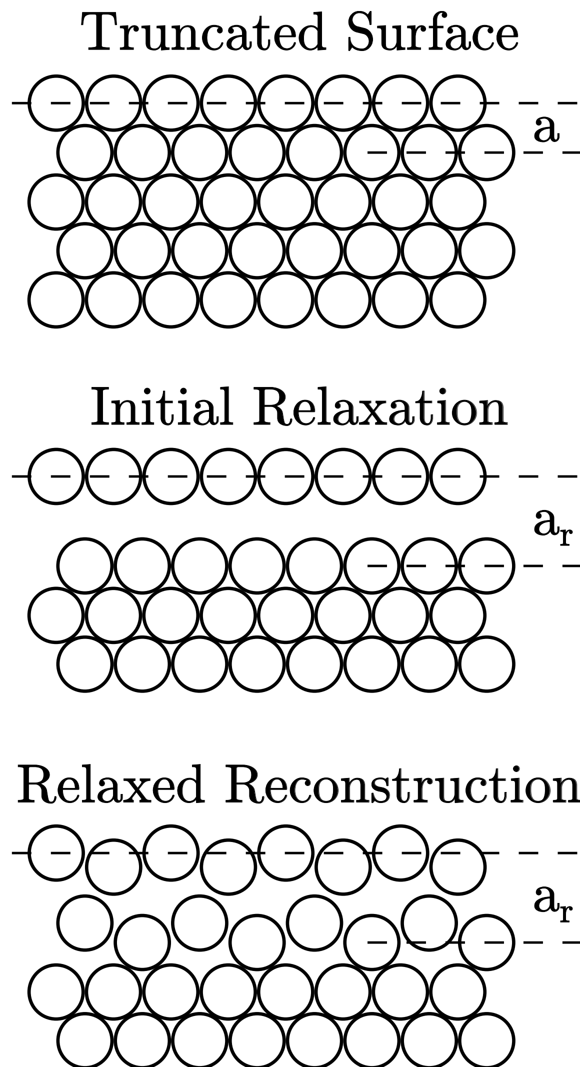

Figure 2.7: The process of surface reconstruction with atomic movement a) truncated crystal b) layer movement due to no overlayer c) atomic roughening of surface to reduce total energy, with a_r labelled as the reconstructed perpendicular lattice spacing (after [8]).

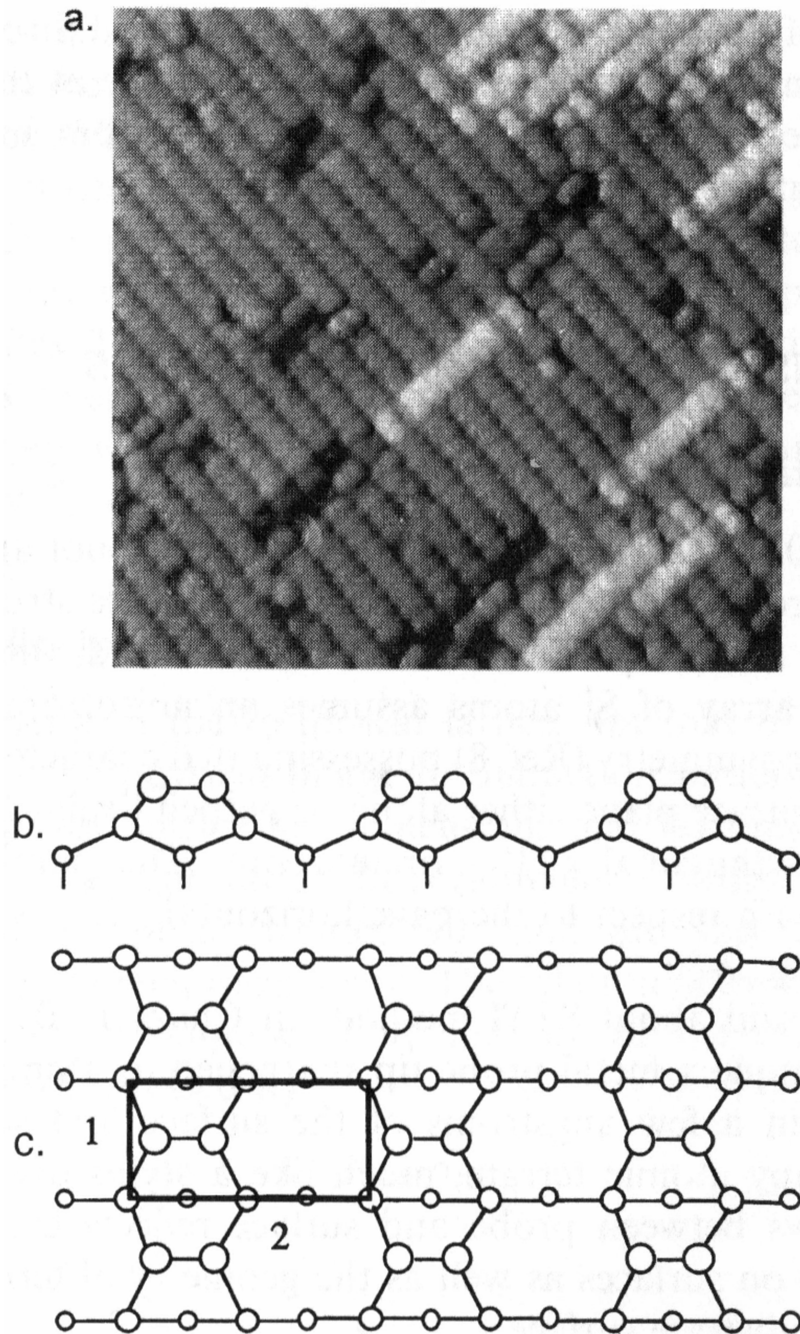

Figure 2.8: a) STM of silicon surface reconstruction showing Si dimers b) cross sectional view of model (2×1) surface reconstruction c) top view showing reconstructed surface unit cell (used with permission from [16, 17]).

The resulting reconstruction can be multiple layers thick, progressively containing fewer atoms from the bulk to the surface. Similarly, if reconstructions are formed in the appropriate atmosphere, the reconstruction can integrate additional atoms into the reconstruction.

2.3.1 Cuts Along High-index Planes

When crystals are cut along low index planes (for example {100}, {111}, {110} in cubic structures), surface reconstructions happen directly on these surfaces. When crystals are cut along high index planes, there is additional energy associated with exposing non-close-packed planes. These high index planes are highly unfavourable and do not have stable reconstructions. The high index surface instead undergoes a breakup into sections of low index planes, separated by steps of fractional or multiples of the unit cell, as shown in Figure 2.9. These low index planes can then further reconstruct as previously discussed.

The most common case of high index planes exposed for surface reconstruction is offcut or vicinal surfaces. The surfaces of single crystal wafers, when cut from a boule have a misalignment from the intended low-index plane due to processing error. These wafers, when reconstructed form terraces of the low index plane separated by fractional unit cell steps. Steps are formed either as “single” (height $\frac{a}{4}$) or “double” (height $\frac{a}{2}$), with terrace lengths determined by the offcut angle, as in Figure 2.10 and Equation (2.6).

$$l = \frac{a/2}{\tan\alpha} \text{ or } l = \frac{a/4}{\tan\alpha} \tag{2.6}$$

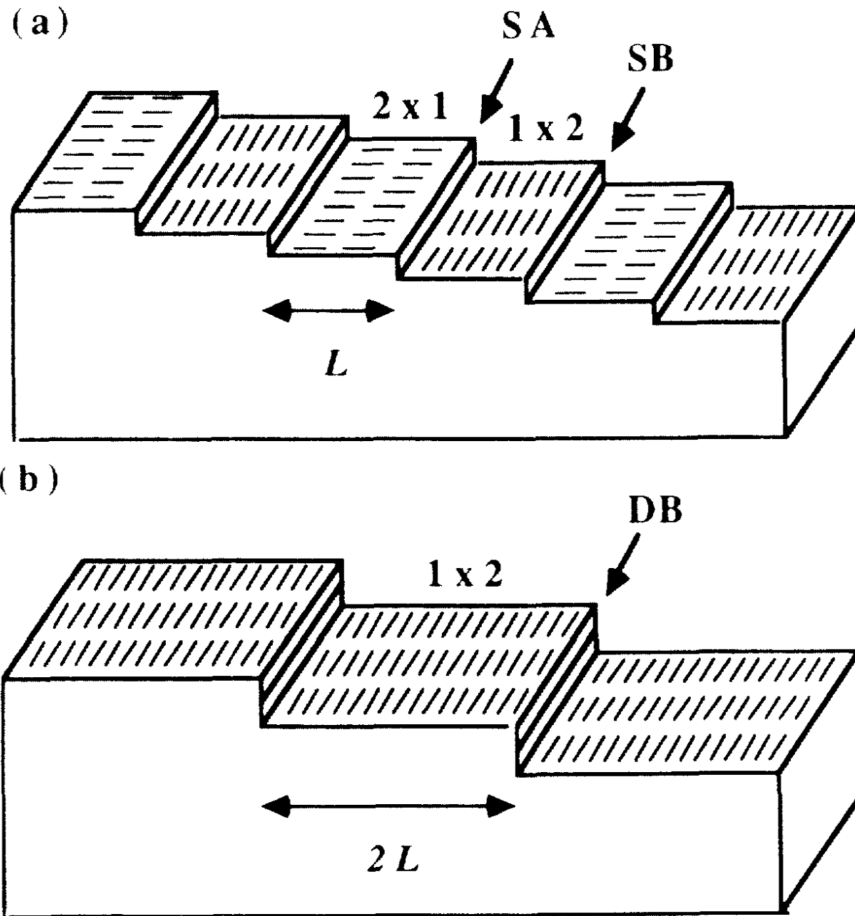

Figure 2.9: Vicinal silicon (100) surface reconstructions, a) single steps (SA, SB) with alternating sublattices and dimers and b) double steps (DB) with the same sublattice exposed[18](used with permission, Copyright (1990) by The American Physical Society).

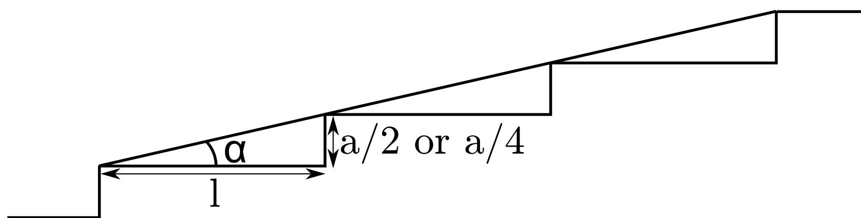

Figure 2.10: Terrace length of reconstructed stepped surface due to offcut of α.

2.3.2 Thermodynamics, Kinetics and Stability of Surface Reconstructions

While an unreconstructed crystal surface is in a high energy state, all the routes to lower energy states require an input of energy. Thus, while a crystal surface may be in a high energy state after cutting, cleaving, polishing or other processing which exposes that surface, it can do very little to resolve its situation without help. Energy must be inputted into the system to allow the atoms to move, bond or leave the surface. The energy landscape of surface reconstructions has many local minima, so there are many possible surface reconstructions for a given surface, depending upon how much activation energy is provided to the system. Beyond how much energy is delivered to the crystal, it takes time for the atoms to reach a of local minima for the surface. Some surface reconstructions can take a significant time to progress to completion. Adding more energy in an attempt to speed up such reconstructions can result in transitions into another reconstruction, as such, time spent reconstructing is a key factor in the conditions of the final surface.

Thus far, energy and time have only been discussed in general terms. The most successful and commonly used method of delivering energy and eliciting a reconstruction is to increase the temperature of the crystal. Crystals can be annealed at a carefully controlled temperature or over an arbitrary temperature profile. Careful experimentation with annealing of crystals has resulted in phase diagrams of surface reconstructions given a surface and temperature combination, as seen for the Silcon (100) surface in Figure 2.11.

The formation and stability of a given surface reconstruction also depends upon the environment surrounding the crystal. Assuming the surrounding environment does not chemically react with a given crystal, the presence or absence (vacuum) of an inert gas will affect the activation energies for the surface atom processes. A vacuum above a crystal when annealing promotes the exit of atoms from the surface as there is no equilibrium vapour pressure resisting the exit of addition atoms. For complex crystals which incorporate elemental gases into their lattice, different surface reconstructions are achievable if an overpressure of those gases are present, rather than a vacuum. These surface reconstructions are commonly seen in the complex oxides, where oxygen is a primary constituent of the crystal and will be lost from the surface during annealing if an overpressure is not provided.

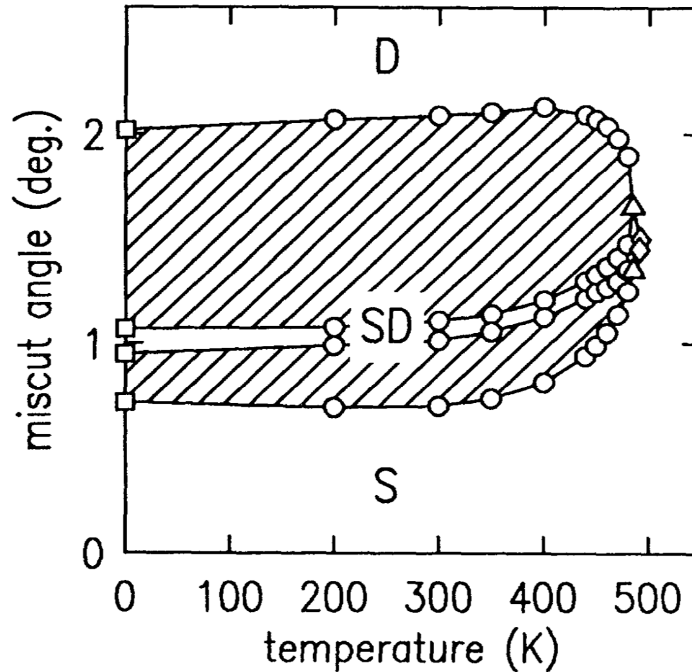

Figure 2.11: Phase diagram of the Silicon (100) surface reconstruction showing regions of single and double steps, with shaded region of mixed reconstruction[19](Copyright (1991) by The American Physical Society).

Stability of surface reconstructions to subsequent interactions with atoms added to the surface varies widely depending upon the properties of the crystal. Semiconductor crystals have less stable surface reconstructions, where interactions with additional atoms easily destroy an established reconstruction. The most common example are the common silicon reconstructions, which are disrupted and destroyed during epitaxy of additional layers. Refractory crystals (defined as those materials wit high melting points and with stability above 538℃[20], such as MgO T_m = 2852℃, Al_2O_3 T_m = 2072℃ and $MgAl_2O_4$ T_m = 2130℃) such as complex oxides are considerably more stable once reconstructed, a point which has been taken advantage of later in this work.

2.3.3 Nomenclature for Surface Reconstructions

Since surface reconstructions are pseudo-2D constructs, the allowed symmetries of a surface reconstruction are a subset of those of the allowable 3D lattices. There are five unique 2D surface nets that can be used to describe the symmetry of a surface

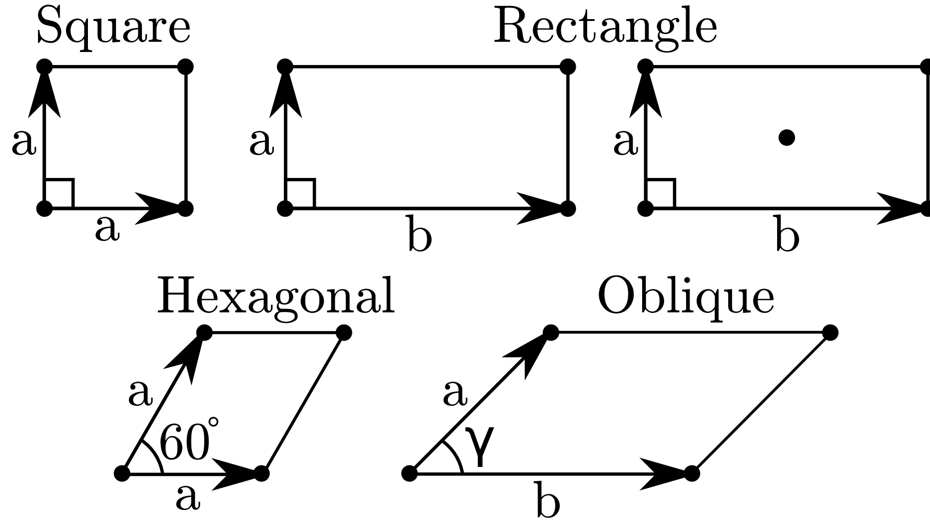

Figure 2.12: The five unique 2D surface nets, all are primitive (single atom basis) except for the two atom centred rectangular net (after [8]).

reconstruction as shown in Figure 2.12

The nomenclature of naming surface reconstructions is determined by the relationship of the 2D surface lattice to the underlying unit cell. The notation preferred in the literature was originally introduced by Wood[21] The smallest repeating surface cell is determined and denoted by whether it is primitive (P), having only one atom per surface cell, or centred (C) having two atoms per unit cell. The surface cell's repeat unit is then related to the underlying unit cell by the ratio of the surface cell lattice constant to the unit cell lattice constant. Thus, the simplest surface reconstruction for a crystal would be the $P(1 \times 1)$ reconstruction, containing one atom, and having the same spacing as the underlying crystal. These nomenclatures do not include details such as the type, number or configuration of atoms which constitute the reconstruction. These reconstructions can also be rotated relative to the underlying unit cell (R). A number of example surface reconstructions namings are shown in Figure 2.13. The nomenclature for surface reconstructions is not unique, as a reconstruction such as $C(2 \times 2)$ is equivalent to $(\sqrt{2} \times \sqrt{2})R45°$ reconstruction.

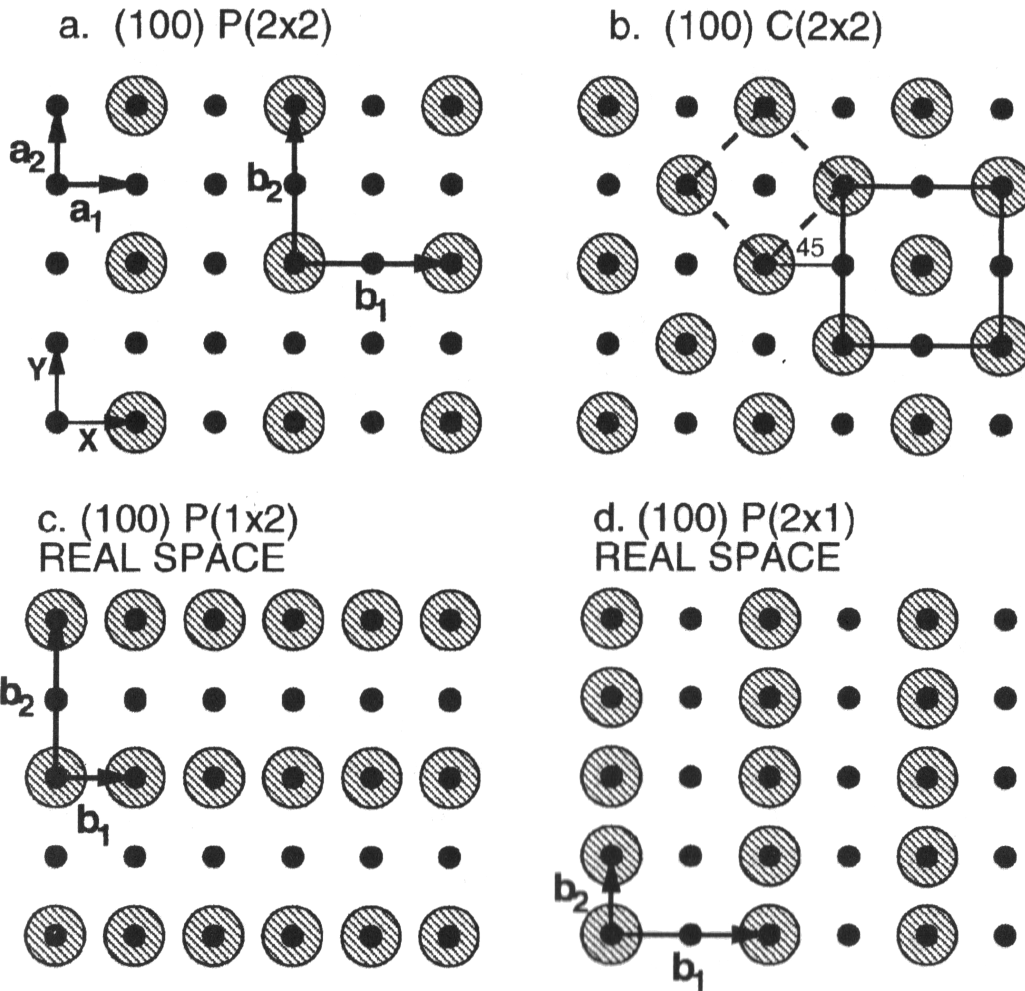

Figure 2.13: Examples of simple cubic surface reconstructions showing atomic positions of reconstructed atoms (shaded) relative to bulk atoms (dots) on a (100) simple cubic substrate. a) P(2×2) b) C(2×2) or ($\sqrt{2} \times \sqrt{2}$)R45° c) P(1×2) d) P(2×1) (used with permission after [8]).

2.4 Atomic Bonding — Attraction Between Atoms

The strength of attraction between atoms is a key factor in the growth process of epitaxial crystals. Attraction between atoms in a crystal is dominated by three different types of forces, electrostatic attraction, covalent electronic attraction and dipole attraction. Hydrogen attraction is a fourth type of atomic interaction potential which acts on the permanent dipoles formed in compounds with hydrogen. While it is a substantial component of the properties of water it is rare in crystalline materials and needs no further consideration here.

Electrostatic attraction is the major contributing force in ionic materials. In such systems, atoms exchange electrons due to their large differences in electronegativity and the resulting anions and cations are bonded together via electrostatic attraction. With multiple atoms, the anions and cations are alternately surrounded by cations and anions, allowing the formation of crystals. A common example of purely electrostatic or ionic material is sodium chloride, where each sodium atom (Na) loses its electron to a chlorine atom (Cl) to form a repeating structure of Na^+ and Cl^-.

Covalent electronic attraction is the typical type of attraction seen in most molecules and many crystalline materials. When atoms come together they change their electronic structure to hybridize and share their outermost electronic orbitals. These shared orbitals lower the overall energy of the system, resulting in a strong bonding force between the two atoms. These bonds, sometimes called chemisorption, typically have energies of 1–10 eV[15]. When multiple atoms are brought together, they can hybridize and share atomic orbitals between more than one atom, allowing for a multitude of configurations and the diversity of crystal symmetries seen in nature. An example of a purely covalent material is silicon, where each atom has hybridized its electronic orbitals and shares its orbitals equally with four surrounding silicon atoms.

Van der Waals attraction is the third of the atomic interaction potentials. Van der Waals attraction is due to the dipole-dipole interactions between the electronic structure of atoms. Such an attraction process is different than covalent sharing, the electronic structures are attracted due to their oscillating dipole of the electron could, but do not share or hybridize electronic structures. These atomic interactions occur at greater distances than covalent interactions, and are considerably weaker, generally

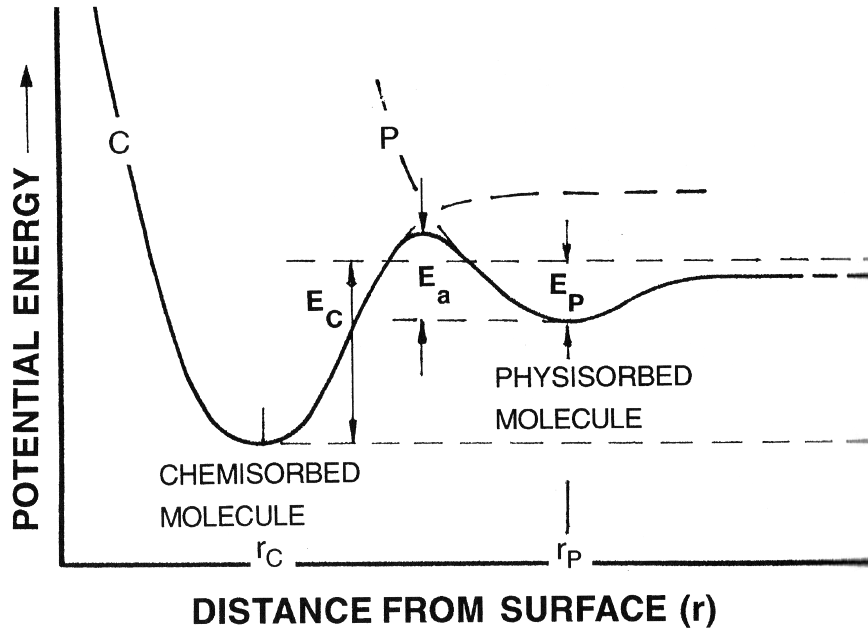

Figure 2.14: Potential energy versus distance for an atom with respect to a surface, showing the region of physisorption and chemisorption (used with permission from [8]).

having potentials of 10–100 meV. The van der Waals potential is the force that initially binds adatoms at the epitaxial interface, sometimes denoted physisorption, allowing them to move on the surface before chemically reacting and becoming covalently bound. The potential energy of an atom approaching a surface is shown qualitatively in Figure 2.14, showing the first energy minimum of physisorption and the second deeper potential energy minimum of chemisorption.

In real materials, the bonding is more complicated than the three distinct potentials described. Many materials have both a covalent and an ionic nature at the same time, a property described as ionicity. In such materials, the electronic orbitals for the atoms hybridize as with covalent systems, but the resulting shared orbitals are unequal. Due to differences in electronegativity, one atom will contain a larger amount of the electronic charge, causing an electrostatic attraction between the atoms in addition to the covalent attraction. Most materials fall into this category of having a partial ionic nature.

In addition to the partially ionic nature of some solid materials, other materials also contain a partial van der Waals nature. Generally, such materials consist of stacked layers of covalently bonded atoms which have their electronic orbitals fully satisfied.

These layers of atoms, by virtue of being atomically flat, come into close contact with adjacent layers, close enough that their electronic orbital electrical dipole moments cause attraction, allowing for stable stacking. A common example of such a material is graphite, an allotrope of carbon, in which the carbon atoms hybridize and covalently attract in a single atom thick layer, which are then attracted to each other via van der Waals forces. Such bonding is rare in epitaxial systems but may be of relevance to the epitaxial liftoff phenomenon examined later.

Chapter 3

Experimental

3.1 Introduction

The work presented in this thesis, being experimental in nature, hinges on numerous experimental techniques. The fundamental components of this work rely on extensive use of X-ray diffraction (XRD) and transmission electron microscopy (TEM) in both standard and novel ways. These techniques will be examined and explained in some detail, as their novel usage is integral to the work presented here. Several other experimental techniques are also utilized in this work, but they are used in their everyday implementations as seen in the literature. These experimental techniques will be discussed only briefly. The two primary growth techniques used in this work will also be described, however as this work concentrates on epitaxy as a general phenomenon, the intricacies and parameter spaces of these techniques will not be considered again for brevity.

3.2 X-Ray

X-rays are high energy photons, generated from the transitions of electrons between their core shell energy levels and bremsstrahlung radiation (the deceleration of electrons). X-rays have weak interactions with matter, being absorbed or perturbed only slightly upon passing through it. X-rays have wavelengths comparable with the typical spacings between atoms in crystals, placing them as an ideal non-destructive probe for crystal structure. In XRD, X-rays experience elastic scattering when interacting with the electrons surrounding atoms. The scattering of X-rays, combined with the 3D periodic structure of atoms, results in constructive and destructive interference and X-ray diffraction[22]. X-ray diffraction is fundamentally an interference phenomenon. For a set of planes within a crystal separated by some distance (d), they will diffract from those planes at an angle (θ) depending upon the wavelength (λ), this is known as Bragg's law as in Equation (3.1).

$$2d\sin(\theta) = n\lambda \tag{3.1}$$

Bragg's law is identical to the phenomenon of thin film interference of visible light, only differing by the scale. Bragg's law, while correct, is a one dimensional expression, in three dimensions it can be represented by the Laue equations as in Equations (3.2)

to (3.4). The vectors $\mathbf{k_i}$ and $\mathbf{k_0}$ are the incident and outgoing X-ray beam, (a, b, c) are the primitive vectors of the crystal lattice and (h, k, l) are the reciprocal lattice indices. Thus, for a given crystal with a fixed unit cell, there are only certain relationships between the incident and outgoing X-ray beams that satisfy the diffraction conditions, resulting in X-ray diffraction.

$$\mathbf{a} \cdot (\mathbf{k_0} - \mathbf{k_i}) = 2\pi h \tag{3.2}$$

$$\mathbf{b} \cdot (\mathbf{k_0} - \mathbf{k_i}) = 2\pi k \tag{3.3}$$

$$\mathbf{c} \cdot (\mathbf{k_0} - \mathbf{k_i}) = 2\pi l \tag{3.4}$$

A concept known as reciprocal, or momentum space, is a common construct used in solid state physics to discuss the properties of crystals and is intimately related to diffraction. Reciprocal space can be visualized as a lattice of points, each representing a spacing present in the crystal, and the lattice having the same symmetry as the real crystal. Reciprocal space is also the Fourier partner of the real space lattice of the crystal. Reciprocal space provides an opportunity for an alternate expression of the conditions for diffraction, known as the Ewald construction. The Ewald construction or Ewald sphere expresses the diffraction condition through the overlay of a sphere of radius $1/\lambda$ pinned on its radius at the origin in reciprocal space, an incident X-ray beam $(\mathbf{k_i})$ entering the sphere. The direction of the exiting diffraction beam is determined by the intersection of the surface of the sphere with the reciprocal lattice, as shown in Figure 3.1. As a crystal is rotated (or the incoming beam is moved), the Ewald sphere will rotate about the reciprocal space origin, sweeping through reciprocal space and exciting diffraction conditions as the sphere coincides with lattice points. The pinned rotation of the Ewald sphere about the origin means that only reciprocal lattice points with a radius from the origin of less than $2/\lambda$ can be excited into diffraction, indicating the effective limitation of a given X-ray source, as well as why light is an ineffective diffraction probe.

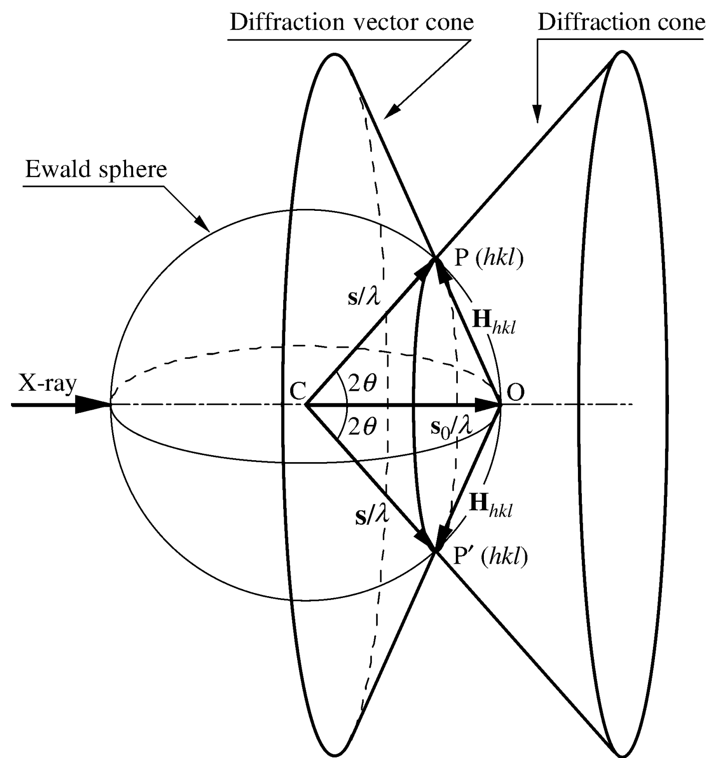

Figure 3.1: Ewald sphere construction of diffraction conditions (vector form of Laue equation) showing incoming X-ray beam to crystal (C) and the reflected and transmitted diffraction cones for a fixed (hkl) and 2θ (used with permission from [23]).

3.2.1 2DXRD — Reciprocal Space Mapping

As shown by Equations (3.2) to (3.4) and Figure 3.1, there are a large number of orientations of a crystal which generate diffraction. For the analysis of crystals, the lowest orders of crystal diffraction (small h,k,l) are the strongest, and provide the least ambiguous information, the they are also at the lowest 2θ values. This still leaves a significant number of diffraction beams of interest to measure and provide structural information. The naïve measurement technique for collecting this information involves taking a crystal and orienting an incoming X-ray beam, and a detector in configurations that satisfy Equations (3.2) to (3.4). Such measurements assume that the experimenter knows the orientation and unit cell of the crystal to a degree well enough to calculate those configurations. If either of those pieces of information is unknown, the experimenter must instead sample the 4π solid angle (usually only the upper 2π half) of the angular space surrounding a crystal with enough resolution to intersect with the diffraction conditions of interest. Such experiments, when performed using a typical X-ray point detector, take inordinate amounts of time, as the angular space is large and the point detector must count for a long time to achieve good counting statistics.

An alternate implementation of such a measurement process is with a 2D planar detector rather than a point detector. A 2D X-ray detector can subtend a large section of the angular space surrounding a given experiment, potentially collecting information about a large section of reciprocal space with each frame it collects. If the configuration is then swept through a range of diffraction conditions, the 2D detector will collect information about a wide swath of reciprocal space. 2DXRD techniques simultaneously collect information about the phase and symmetry of an unknown sample allowing that information to be then examined via a variety of techniques.

3.2.1.1 Practical 2DXRD Measurement

Practical 2DXRD measurements are achieved through the use of a multi-axis goiniometer, a device which maintains the sample at a central point while rotating its orientation relative to the X-ray source and detector. For epitaxial crystals grown on crystalline substrates, a sample under measurement is placed in the goinometer with its surface normal oriented along the goiniometer's sample axis and a reference edge.

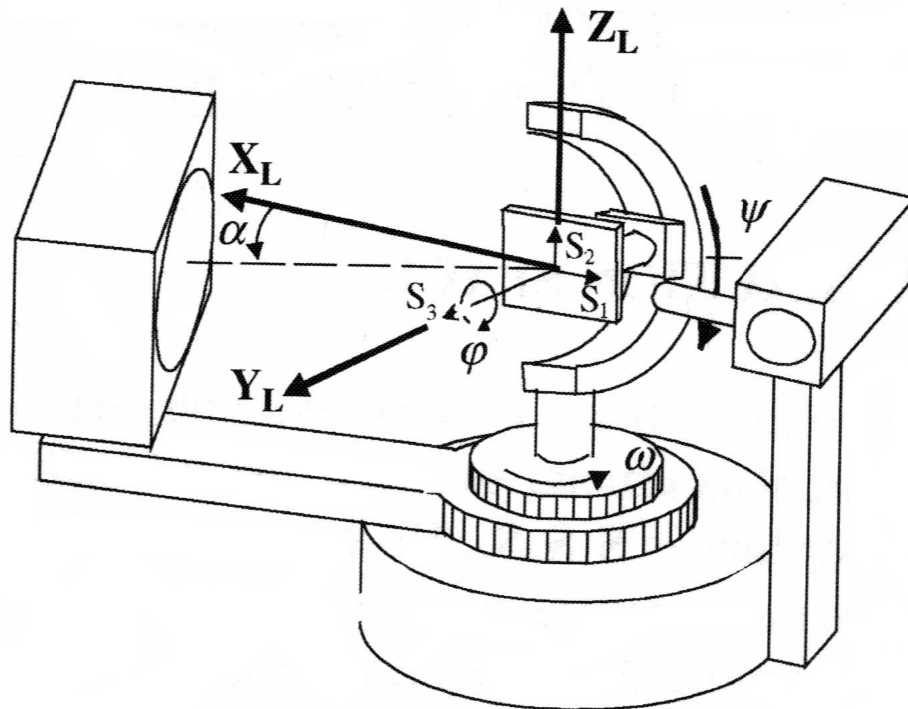

Figure 3.2: Standard configuration of a 2DXRD system with source, sample and detector, with the sample (S) and laboratory (L) coordinate systems labelled. Standard goiniometer angles are also labelled (used with permission from [23]).

An X-ray source is placed on one arm of the goiniometer and the 2D detector is placed on the other arm.

A standard 2DXRD measurement is performed by configuring the goiniometer (Figure 3.2) such that the X-ray source to 2D detector angle corresponds to a known or presumed low-order 2θ angle for the sample. The sample is then rotated such that incident angle to the surface is shallow, typically less than 5°. Such a beam configuration is ideal for collection of maximum diffraction information, however it can greatly increase the X-ray beam width (d_{eff}), as shown in Figure 3.3 and Equation (3.5).

$$d_{eff} = \frac{d}{\sin \alpha} \tag{3.5}$$

If the sample is of limited size, alternate measurement schemes must be computed. The sample is then rotated about its surface normal while the 2D detector takes sequential images, a process known as a φ-scan. By aligning the sample along 2θ in one dimension, and rotating the sample in a complimentary dimension, crystallographic reflections that contain the d-spacing corresponding to a range of 2θ around the selected value will be collected on the detector as they pass through their diffraction condition. The number of frames exposed during this rotation determines the resolution along the χdirection in reciprocal space, while the pixel resolution of the 2DXRD detector, combined with of the 2DXRD detector distance determines the resolution in the 2θ dimension. An additional scan of the sample while maintaining the 2θ configuration and scanning the X-ray beam incident angle is known as an ω-scan. While the combination of these two scans collects only the reflections surrounding the centred 2θ of interest, if the measurement scheme successfully collects most of the reflections, the symmetry of the underlying system will allow any other reflections to be inferred, greatly reducing overall measurement time.

As reciprocal space mapping is a process which operates in angular space, the distance to the detector is an important optimization parameter for 2DXRD measurements. The distance the 2DXRD detector is situated away from sample will change the solid angle subtended by the detector. Close detector distances allow the collection of more reciprocal space data in a given scan, at the expense of reducing the resolution due to finite pixel size, as well as increasing the risk of overlap for features close in 2θ. For epitaxial thin films grown on lattice mismatched substrates, close detector distances can result in substrate and epitaxial crystal peaks overlapping, making interpretation

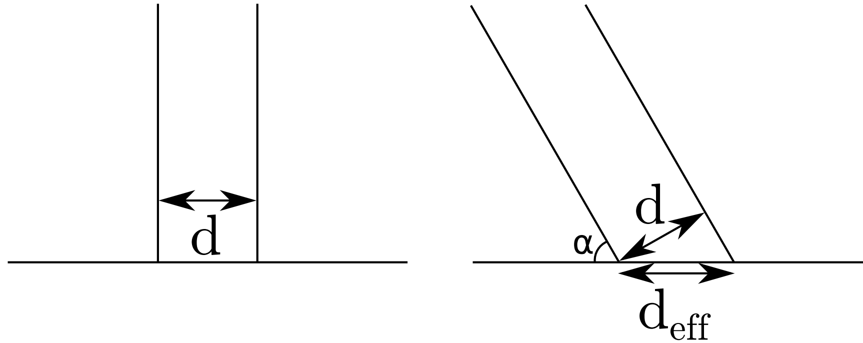

Figure 3.3: Comparison of beam width and effective beam width caused by inclination of sample.

difficult.

The last optimization parameter for 2DXRD scans is the time duration collecting each frame. For a given brightness of X-ray source and thickness of material, the frame exposure times are ideally set to capture counts just below the maximum the electronics can achieve. Maximizing the counts for the X-ray detector ensures optimum signal to noise for a given measurement.

3.2.1.2 Interpretation of 2DXRD Measurements

Once a 2DXRD measurement has been taken, the resulting data consists of a series of 2D detector frames. The exact number of frames is determined by the sampling resolution set during the 2DXRD scans. Each frame is a snapshot of the diffraction intensity collected from the sample for the exact angular configuration in space stored with the frame. A single 2DXRD frame (Figure 3.4) which contains an X-ray diffraction peak can be analyzed via a number of integration techniques. The two perpendicular pixel directions on the 2DXRD frames are transformed into two angular dimensions in the coordinate system of the sample, 2θ and χ [23]. The resulting frame is sliced into hyperbola with the x-direction of the frame corresponding to the radius (2θ) and a new dimension (χ) corresponding to the azimuthal direction along a given hyperbola.

The data on a frame can be integrated in one dimensional plots along either dimension of the hyperbola. Integration of the data along χ and plotting with respect to 2θ results in a pseudo-powder pattern similar to those taken in a common Bragg-Brantano XRD system, except it can be performed for diffraction peaks other than perpendicular to the substrate. Such plots show the presence of d-spacings within the

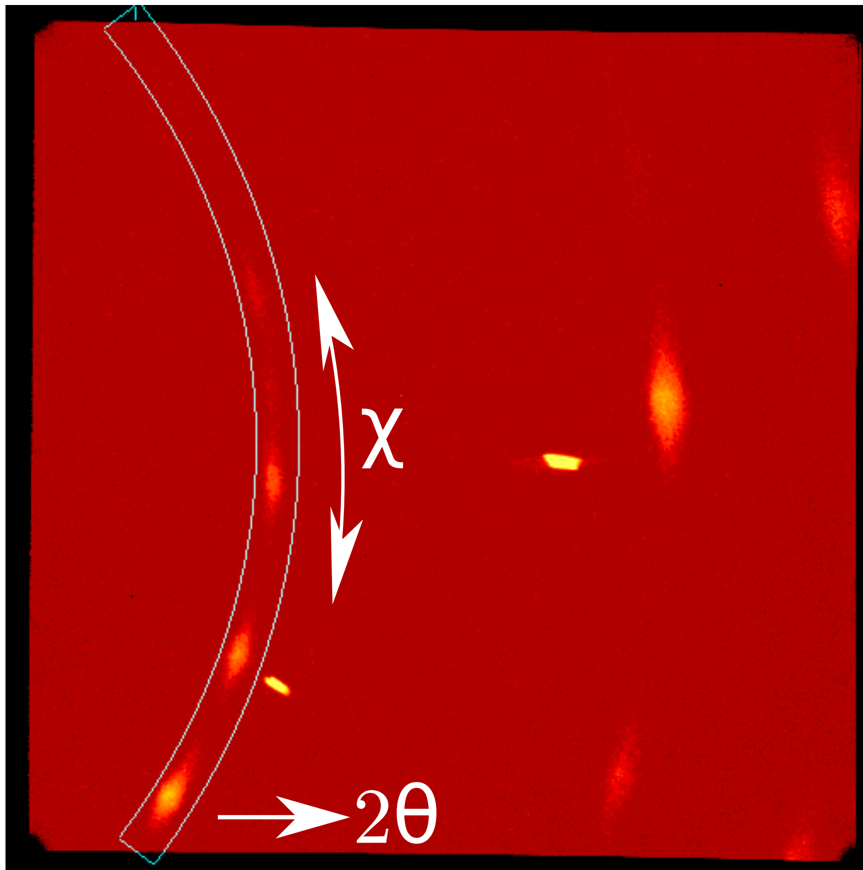

Figure 3.4: An example X-ray frame with a conic section of fixed 2θ highlighted, also showing diffraction space coordinate directions θ and χ.

frame of interest, and their width. Integration of data over a 2θ range and producing a one dimensional plot will show the spatial intensity distribution of a given diffraction peak. An example 2DXRD frame, with labels of the two diffraction dimensions is shown in Figure 3.4.

3.2.1.3 Pole Figure Generation

While integration of the diffraction data on a single frame provides useful quantitative measures of the distribution of a diffraction peak in space, when many frames are collected the generation and interpretation of many frames is tedious and difficult to interpret. Pole figure generation from a set of frames is a method of graphically representing the spatial extent of the diffraction intensity of a given d-spacing around a given sample. Pole figures readily allow the interpretation of diffraction data to assess crystalinity, presence of phases and orientation relationships between a substrate and epitaxial crystal.

To generate a pole figure from a collection of frames a 2θ and χ range are selected on the first frame of a series of frames. Generally, such a range will include the maximum width of a single d-spacing of interest (such as $\{111\}$) and the entire extent of χ on the frame. The range is integrated across 2θ, producing a one dimensional intensity scan. The intensity scan from each frame is then mapped onto the pole sphere (Figure 3.5) according to the frame orientation information, forming a geodesic line of intensity. The pole sphere is a construction centred on the sample which maps the direction in space that diffraction intensity is collected by the detector. As each frame is integrated, the surface of the pole sphere is painted with colour mapped intensity data. The resulting sphere of data is then stereographically (angle preserving) projected onto a circle, resulting in a pole figure[23]. The pole figure is a polar diffraction intensity colour map with the radial direction represented by α, the angle from the top of the sphere and the azimutual direction φ is the in-plane orientation relative to the sample's φ zero orientation set during sample mounting. An example pole figure mapping a single data point from the pole sphere is shown in Figure 3.5.

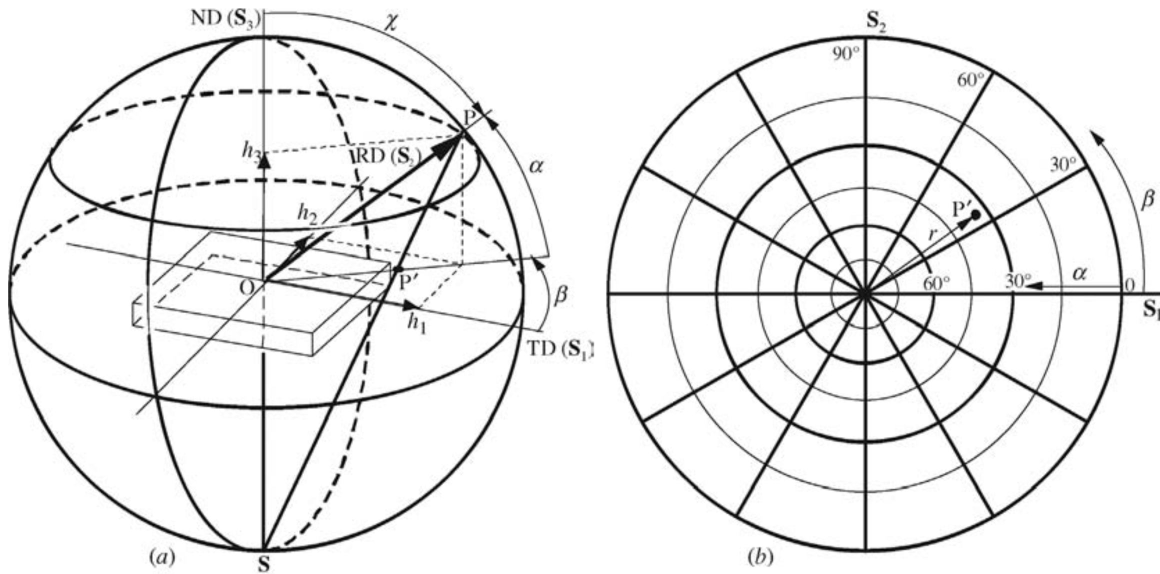

Figure 3.5: Example mapping of pole sphere data points to pole figure (used with permission from [23]).

3.2.1.4 Interpretation and Simulation of Pole Figures

Once a pole figure has been generated the resulting graphical representation of the diffraction data must be interpreted in the context of the sample composition. Generally, a pole figure will be generated for a low-index reflection (100,110,111) for both the epitaxial crystal and the substrate. By generating two figures, the orientation relationship between the diffraction intensity produced by the grown crystal and the single crystal substrate can be examined by comparing the two figures.

The first step for pole figure analysis is to examine the pole figure generated from the substrate low index reflection. Since the substrate should be a single crystal, it is trivial to interpret it for its orientation information. A single crystal pole figure of the substrate can be simulated by considering the space group (cubic, hexagonal, etc.), unit cell, and physical orientation (100-up, 111-up), calculating the surface normals of the d-spacing of interest, collecting them on a pole sphere and mapping them onto a pole figure. This is conceptually identical to the generation of a pole figure from raw data, except the data is computed from a perfect crystal unit cell. Such pole figures are simulated using a piece of software such as WinWulff[24] as seen in Figure 3.6, allowing interaction with the pole figure. The pole figure generated from the data is then compared to the simulated pole figure and the simulation is manipulated by

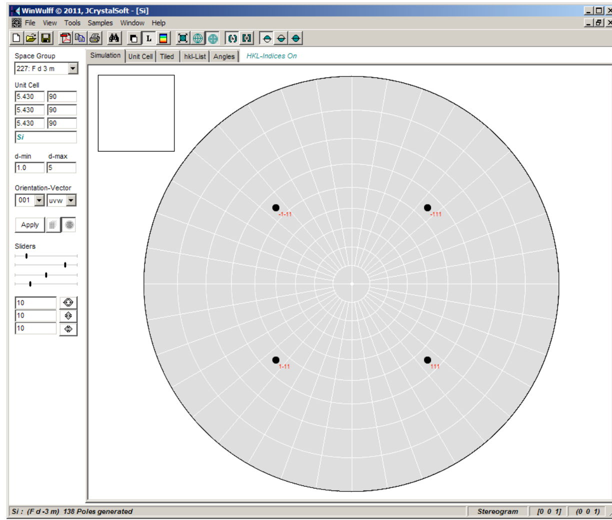

(a) WinWulff (111) pole figure of (100)-up silicon.

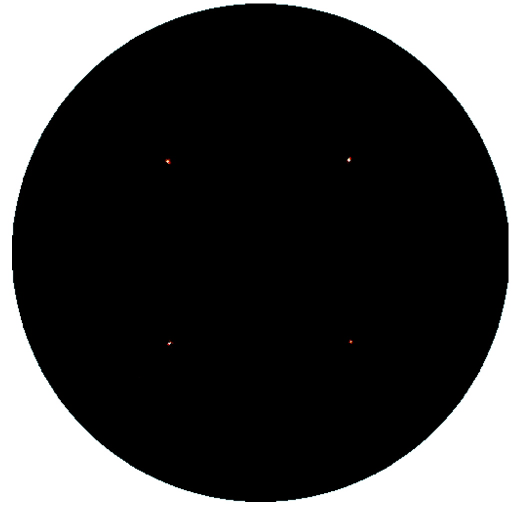

(b) Experimentally generated (111) pole figure of (100)-up silicon.

Figure 3.6: Comparison of WinWulff simulation and experimental single crystal silicon pole figure.

changing the orientation of the crystal until the two figures coincide. The orientation information provided by the simulation software is now the same as the orientation of the measured crystal. Such comparison provides the absolute orientation of the crystal in the diffractometer, and all other pole figures generated form the dataset can be referenced to that crystal.

Now that the substrate orientation is known, the pole figure generated from the data can be absolutely referenced to the substrate orientation. If the epitaxial crystal is also a single crystal, the same trivial comparison process can be performed. The resulting orientation of the eptitaxial crystal can be compared to the substrate, providing the epitaxial relationship.

For the case of systems which have non-ideal epitaxial growth, the pole figures likely contain diffraction intensity information from a number of crystalline sources. This pole figure is the convolution of the pole figures for each of the components of the epitaxial crystal. There are several features which arise in such pole figures which are characteristic of certain growth relationships. A pole figure that, when generated, is uniform in intensity, or has intensity present everywhere with a broad distribution is characteristic of a strongly polycrystalline growth random in orientation, with no epitaxial relationship to the substrate, a simulated pole figure of such a situation is

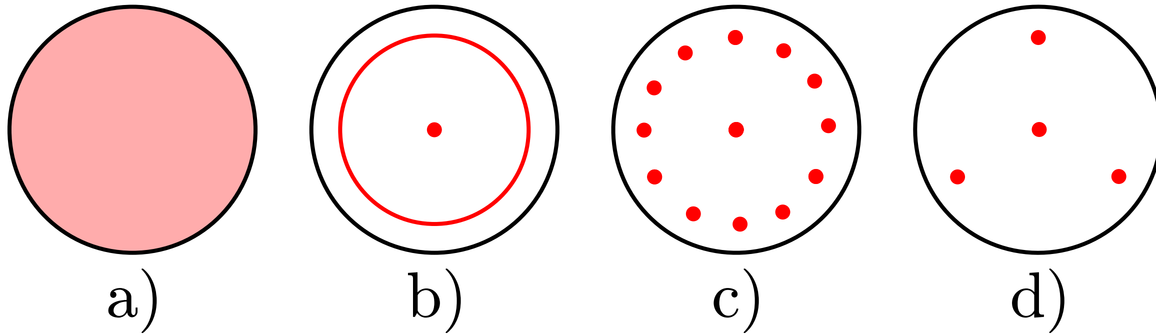

Figure 3.7: Example (111) pole figures of a) Polycrystalline randomly oriented b) (111)-up in-plane random orientation c) (111)-up textured epitaxial d) (111)-up single crystal FCC cubic crystal.

shown in Figure 3.7a. Pole figures which contain bands of diffraction intensity which are rotationally symmetric about their centre are characteristic of a crystal that has a preferred stacking order in the vertical direction, but has no in-plane orientation, such an example is shown in Figure 3.7b. Such preferred stacking orders, usually (111)-up, are a common occurrence when growing binary cubic materials.

The most difficult situation that occurs is when the generated pole figure contains multiple single crystal-like peaks. The presence of single crystal-like peaks indicates a number of different orientations of the epitaxial crystal. These epitaxial crystals are referred to as textured materials, an example of which is shown in Figure 3.7c. For textured epitaxial crystals, there are number of possibilities for the cause of texturing during growth. Faced centered cubic binary semiconductors have a propensity to have stacking faults or twins during growth. The twinned crystallite will create new diffraction peaks in the pole figure, they will have a twin relationship with the host crystal about the twin direction (usually {111}). Other textured epitaxial crystals may arise through multiple preferred growth relationships with the underlying substrate. Such systems typically have pole figures where the symmetry of the overall pole figure reflects the substrate surface symmetry. The example in Figure 3.7c is one of a (111)-up crystal (3-fold symmetry) on a (100) substrate (4-fold symmetry), showing $3 \times 4 = 12$ peaks.

Beyond the analysis of the symmetry of diffraction intensity, which identifies the crystallites present within a sample, the peak intensities within the pole figure provide a wealth of information about the epitaxial crystal. Similar to the integration techniques applicable to raw 2DXRD frames, the diffraction intensity in a pole figure can be sliced

and integrated in a number of ways. The pole figure can be inspected by integrating the intensity in a given area, allowing comparison of individual diffraction peaks. Pole figure intensity can also be integrated radially and plotted versus φ, providing information on the in-plane rotational misalignment of the selected epitaxial crystallites. Finally, pole figure intensity can be integrated versus φ and plotted radially.

Plots of peak broadening from pole figures are particularly informative. Broadening of diffraction peaks preferentially in the radial dimensions is a sign of strain present in a crystallite. The radial location of a peak in a pole figure is determined by angular relationships of the unit cells of the sample, fixed angles are expected for a given crystal group (e.g. cubic). Radial broadening in a pole figure is an indication that the unit cell has been distorted from its preferred shape. Similarly, broadening in azimuthal directions indicates the individual crystallites sampled by the 2DXRD measurement have in-plane misalignment, similar to a textured film, but of much smaller extent.

3.2.2 High Resolution XRD

While mapping reciprocal space provides much information about the phases and symmetries present in a given sample, the resolution available on such 2D detectors is limited in both the number of pixels, and the spacing between them. In addition, the X-ray beam geometry associated with 2DXRD measurements introduces instrumental broadening into the measurements preventing careful inspection of small scale diffraction details. To examine the small scale details of diffraction intensity, a different configuration must be implemented for the X-ray source and detector, this configuration is known as high resolution X-ray diffraction (HRXRD). If the general landscape of reciprocal space (diffraction intensity) is known through the application of 2DXRD techniques, HRXRD can carefully sample small sections of reciprocal space with very high resolution.

Recall that for a perfect crystal, there is only a single configuration for which the diffraction condition will be satisfied, resulting in a highly intense diffraction peak with minimal spacial extent. For a real sample, intensity distribution of individual diffraction peaks in reciprocal space provides information about the deviance from the ideal crystal.

Using HRXRD measurements, the precise d-spacing of a given material can be determined, showing whether a sample has its lowest energy structure or it is strained. If the orientation of the sample can be controlled carefully, the d-spacing can be

measured absolutely, otherwise, it can be measured relative to a known standard such as a single crystal substrate. The broadening (spatial extent) of a HRXRD peak provides different information depending upon the dimension along which it is examined. In the 2θ direction, the radial direction in reciprocal space, broadening indicates that the spacing of interest is a distribution of spacings within the region of the sample illuminated by X-rays. Such distributions can indicate strain or compositional variation in the region of interest. The broadness of the X-ray peak when a sample is rocked in the ω direction, while keeping 2θ fixed indicates that a given d-spacing has a distribution of orientations within the sample, usually indicating multiple crystallites.

3.2.2.1 Practical HRXRD Measurement

To ensure the validity of HRXRD measurements of precise d-spacings and X-ray diffraction peak widths, the HRXRD system and its operation must satisfy several conditions. These properties specifically deal with the properties of the X-ray source used in HRXRD, and the operation of the goiniometer in the rotation of the sample, source, and detector.

For practical HRXRD, the X-ray source must be monochromated far more than for general X-ray work. Typical X-ray sources will contain bright peaks from multiple core electron levels, along with bremsstrahlung radiation, and will be monochromated with a single monochromator. Such a source will still have an appreciable broadening in its peak and such broadness will convolve with the sample's true properties. HRXRD measurements must be taken with X-ray sources with at least two monochromators, and may have up to four. Monochromation will ensure that the instrumentation broadening will be below the level of the sample's diffraction properties, allowing a sensible measurement result. Such extra monochromation results in a weaker signal than general experiments, and a much longer experiment time. Beam size considerations are a balance between the sample's spatial distribution and the intensity of the diffraction signal.

The second practical requirement for HRXRD is for precise alignment of the sample, and the ability to be make precise movements of the sample. Absolute alignment of the sample is required to absolutely determine the orientation of crystal structures and the d-spacing of the planes of interest. Precise orientation and movement of sample is achieved by a goniometer with resolution of at least one arcsecond (1/3600 of a degree), with good reproducibility.

Practical HRXRD measurements, even after performing alignment, are best performed with reference to a known diffraction peak. 2DXRD pole figures generated from a sample are an essential first run to screen samples and to determine absolute orientations. If multiple crystal orientations are present, HDXRD does not provide useful results. If crystal orientation is determined relative to the sample orientation and careful sample mounting is undertaken, absolute crystal d-spacings can be determined from straight HRXRD scans. For most practical HRXRD measurements attempting to determine the precise d-spacing for a epitaxial crystal, it is best practice to align to a strong reference peak of the substrate, and include that peak in the measurement to allow both absolute measurement and relative calculation of the d-spacing. D-spacings in such a configuration are calculated by measuring the difference in 2θ between the reference peak (which has a known d-spacing) and the peak of interest, determining the absolute d-spacing.

3.3 Electron Microscopy

The second of two useful probes for examining the properties of epitaxial thin films is electrons, specifically, electron beams generated for electron microscopy. The electron, unlike the X-ray is a charged particle which interacts fairly strongly with materials. Free electrons can be generated and accelerated to high velocities, resulting in de Broglie wavelengths orders of magnitude smaller than X-rays and as a result can be confined or focused to sub-angstrom areas. The electron's use as a probe can be used as both a mechanism to excite other phenomena for study, or to measure the effect a given sample has on a beam of uniform electrons. For a generic beam of nearly-monochromatic electrons, typical of electron microscopy, a number of interactions are possible for a sample of finite thickness, as shown in Figure 3.8. The interactions of electrons with a sample can provide both chemical and structural information with fine spatial resolution thanks to the tight control of electron beams.

This work relied upon two measurement techniques which utilized electrons as their primary probe, scanning electron microscopy (SEM) and (scanning)transmission electron microscopy (STEM/TEM). SEM is an invaluable non-destructive technique for examining surfaces at high resolution to extract information about both the structural and chemical properties. STEM/TEM is a tool which uses similar interactions to examine the cross sectional structural and chemical properties of mechanically thinned

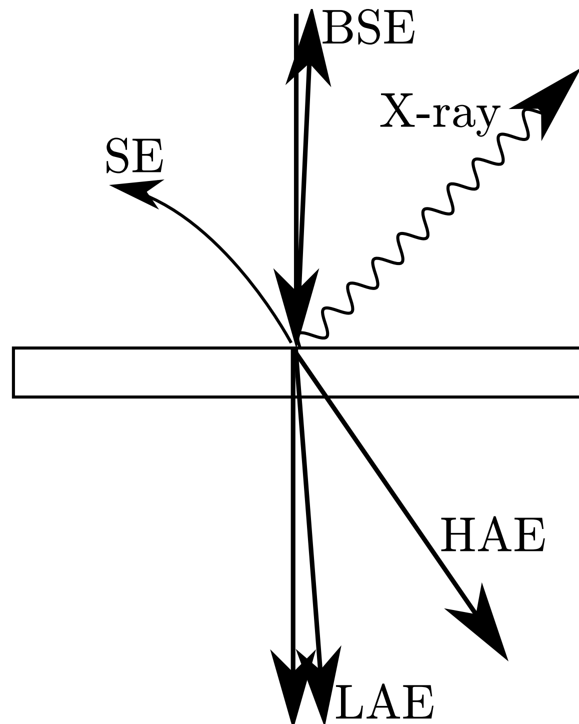

Figure 3.8: Schematic of an electron beam interacting with a sample showing backscattered electrons (BSE), secondary electrons (SE), generated X-rays, low angle scattered electrons (LAE), high angle scattered electrons (HAE), and the main electron beam passing through the sample.

slices of materials with sufficient resolution to examine individual columns of atoms in crystals.

3.3.1 SEM

Scanning electron microscopy is a high resolution non-destructive and non-contact technique used to examine the surface of a sample. SEM can reveal the topography and chemical composition of a surface down to 10's of nanometers, and the chemical composition on the micrometer scale. These measurements are achieved through the interaction of a beam of nearly-monochromatic electrons generated from a heated filament or cold cathode and accelerated to kilovolt energies in an high vacuum chamber and focused onto a sample. Magnification is achieved in SEM by careful scanning of the focused beam over a small area.

3.3.1.1 Secondary Electron Imaging

The most common electron-material interaction utilized in SEM is generation of images through the production and capture of secondary electrons. Secondary electrons are continuum (valence and conduction band) electrons excited from the sample through inelastic scattering excitations as an electron beam penetrates into a sample. These electrons typically have energies of less than 50 eV[25]. Secondary electrons, while generated along the path of incoming electrons, can only typically escape from depths of less than 7.5 nm, making secondary electrons surface sensitive[25]. Secondary electrons are collected by biasing an electron detector to electrostatically attract these low energy electrons while not appreciably affecting the incoming beam. Electron detectors are typically a phosphor screen combined with a photomultiplier tube to provide high gain. Images are formed by scanning the beam across the surface of the sample and counting the secondary electron yield for each dwell point within the scan. The resulting grid of counts is transformed into a bitmapped grayscale image.

As secondary electrons are low energy, their escape depth from a surface is very shallow, as such their yield is very sensitive to the local topography of the sample. Thus to the first approximation, the contrast in a grayscale image formed from secondary electrons is a representation of the topography present on the surface of the sample. Regions with vertical extent will increase the yield of secondary electrons, due to more of the sample being within nanometers of the surface. An extreme case of this is

vertical edges, which will have a high yield of secondary electrons, due to having the top and side surfaces both yielding secondary electrons.

3.3.1.2 Backscattered Electron Imaging

High energy incoming electrons can also interact with samples via elastic scattering. Electrons which are scattered at close to 90° are backscattered close to the incoming beam. By placing an unbiased detector near the incoming electron beam the detector can capture backscattered electrons. The electron elastic scattering process is proportional to atomic mass ($\sim\sqrt{Z}$) of the sample. The yield of backscattered electrons provides mass (usually called compositional) contrast of the sample under the electron beam. Penetration depth of the electron beam for backscattered electrons is deeper than secondary electrons, generally penetrating 1–2 µm into the sample, as well as laterally broadening. Such broadening reduces the resolution of backscattered imaging compared to secondary electron imaging.

3.3.1.3 Practical SEM

The practical application of SEM for imaging of samples requires the optimization of several parameters. While SEM is a non-destructive measurement technique, intentional sample preparation can vastly improve the imaging resolution and reduce noise. A key requirement for SEM samples is that the sample is sufficiently conductive to conduct away the electrons delivered by the scanning beam. For high conductivity samples, sample preparation can be as simple as bonding to a sample holder using conductive tape or paste (such as carbon tape or silver paste). Samples with poorer bulk conductivity may require conductive paste applied to contact the top surface to the sample holder. Highly insulating samples are normally coated with a thin layer of high density metal (Pt, Au) or amorphous carbon in order to provide a conduction path to the conductive paste connecting the top surface to the sample holder.

Optimization of imaging for a given sample is achieved through the tuning of several imaging parameters, working distance, accelerating voltage, beam current and dwell time[25]. For typical secondary electron imaging, the goal is to interact with the thin top surface layer with the smallest lateral beam possible. Minimization of accelerating voltage, beam current and working distance will maximize the resolution and reduce the surface interaction. Reduction of these working parameters has the

side effect of reducing the signal to noise ratio (SNR) of imaging. Increasing dwell time can improve SNR, but for poorly conductive samples charge buildup will cause deflection of the incoming beam. Stacked averaging of quick scans yields improved SNR on the tradeoff of time.

Interpretation of the secondary electron images in one key case is ambiguous; topographic features with vertical extent can appear to be both a depression and a bump simultaneously, due to the assumption of the human visual system that lighting always comes from above[25]. Care must be taken for features of this type to avoid misinterpretation. Modification of some imaging parameters can break the ambiguity and reveal the topography, including tilting the sample, rotating it about its surface normal using the SEM's focus and depth of field parameters to slice through the topography.

Imaging of samples using backscattered electrons to achieve chemical composition requires optimization of the elastic scattering process from the sample. The primary parameter that improves backscattered electron yield is increases of the electron accelerating voltage. Increasing the accelerating voltage has the downside of increasing the area of electron interaction, which reduces the effective spatial resolution[25]. The elastic scattering process is less efficient per incident electron than secondary electron generation, as such beam dwell times must be increased to improve SNR. To obtain a accurate measure of chemical composition, samples for backscatter analysis should be as flat as possible, as topography can modify the yield of backscattered electrons, processing such as polishing is essential for the highest accuracy chemical composition. If the measurement is intended to be non-destructive, careful correlation between backscattered and secondary electron images must be used to ignore topographic effects.

3.3.2 TEM

While scanning electron microscopy relies on the information generated from the surface and sub-surface of arbitrarily thick samples, transmission electron microscopy (TEM) relies on the information generated from electrons which transmit through a sample. Through control of the electron beam information about the thickness, crystalinity, and defects of a sample can be collected.

Imaging of samples via TEM is produced via one of several interaction mechanisms of a beam electrons with a thin sample, as noted in the transmitted electron beams in

Figure 3.8. Electron beams are generally on the order 10's to 100's of kilovolts and are controlled via magnetic lenses[26]. Images can be formed by collecting the scattered beam (dark-field) or the transmitted beam (bright-field) focused onto a scintillating screen or electronic CCD array. Magnification in TEM is achieved by controlling the width of the beam that passes through the sample and then expanding it again onto the detector. Magnification is generally limited by aberrations present in the magnetic lenses of the system.

Without any specific alignment of the sample, TEM image intensity provides contrast of the thickness-density product of the sample[26]. Electrons are absorbed or scattered away more strongly where there are more atoms present in the path of the electron beam, either through more electrons per unit thickness, or more thickness in total. Thus, some contrast formed in the image is an indication of the composition.

While thickness-density contrast can provide some information, it is generally useful for amorphous or biological samples. Crystalline materials offer several other contrast mechanisms. The de Broglie wavelength of electrons accelerated in a TEM is much smaller than the spacing between atoms in typical materials, so those electrons can undergo diffraction when they interact with a crystalline sample. Polycrystalline samples will provide distinct intensity contrast due to their large changes in orientation relative to the incoming electron beam, diffracting varying amounts of electrons[26].

When samples are more crystalline, polycrystalline diffraction contrast generally no longer plays a large role. In order to improve the contrast effects of electrons passing through crystalline samples, the sample must be aligned along a "zone-axis," that is, along some crystal direction in order to transport electrons mostly unperturbed down atomic columns. TEM samples are tilted to align the sample so the beam travels along a crystal direction. When crystalline samples are aligned in such a way, defects that break the periodicity of the crystal result in scattering of the electrons and create what is called phase contrast. Phase contrast will highlight regions where the atomic columns have defects which scatter electrons[26].

When a sample has crystal defects which present the same zone axis, such as twins, they do not show up in diffraction contrast or traditional phase contrast. In these cases, single zone axis imaging cannot provide a contrast mechanism which differentiates the two phases. Two-zone axis contrast tilts the sample in a second direction perpendicular to the first and brings the sample into a dual-diffraction condition. Since such crystal phases differ in the direction perpendicular to the zone axis, the dual-zone diffraction

uses this difference to provide contrast.

Beyond imaging, the electron beam can be adjusted such that after the electrons pass through the sample, the electrons that diffract with the crystal planes can be focused into spots resulting in a diffraction pattern. This diffraction pattern is akin to an X-ray pattern, it can be used to determine the crystal structure and orientation of the sample under the beam. The size of the electron beam can also be limited, a method known as selected area diffraction (SAD), allowing examination of sections of the sample.

3.3.2.1 Practical TEM

While TEM is a excellent technique for investigating the microstructure of epitaxial thin films, it imposes strict limitations on sample preparation. Samples must have lateral dimensions of several millimetres while being thinned to electron transparency. The precise thickness depends upon the density of the material and the TEM conditions. Samples must be generally thinner than 100 nm for enough electron transmission to provide enough electron scattering to provide contrast while also having those scattered electrons pass through to a detector.

Samples generally start out as wafers or sections of wafers with thicknesses of 500 µm and lateral dimensions of up to several inches. Before thinning of a TEM sample can be undertaken, a section of a (possibly) large bulk sample must be selected. The section selected must be of a size compatible with the thinning process. Preparation of such sections depends upon the properties of the substrate. For substrates with good cleaving properties, a thin bar can be cleaved, for substrates which are much harder, bars must be sectioned using sawing methods such as diamond or wire saws.

Once sections have been extracted from a larger sample, they must be progressively thinned. This is done through a number of steps, starting with mechanical polishing. In traditional sample preparation a sample is preferentially polished in a wedge shape, providing a gradient of thickness, where at some point the ideal thickness is present. In modern preparation techniques the sample is “dimpled,” creating a sample with circular gradient of thickness and then ion milled until break through. Samples prepared by most methods are gentle argon ion milled to remove polishing damage.

When preparation of a specific region of a sample is required, traditional preparation techniques do not provide enough spatial specificity to select features at the micro or nano level. For sample preparation of this type, preparation is performed using a

Focused Ion Beam (FIB) milling system. A hybrid gallium beam/SEM system is used to selectively mill the region of interest and perform localized sputtering of a sample, slicing out a section. After isolating the section, it is welded to a nanomanipulator probe and transferred onto a TEM grid. The sample is then thinned to electron transparency with the FIB beam, before finally being cleaned by argon gentle ion milling.

Preparation techniques must be extensively experimented with when preparing new or unknown samples. Some epitaxial layers will have greatly differing mechanical properties and react differently to mechanical polishing and ion sputtering. Care must be taken to not preferentially remove the material of interest. Haphazard preparation can result in the introduction of artifacts which may cause misinterpretation during imaging.

Beyond sample preparation, imaging in a TEM can be modified by tuning several parameters. The accelerating voltage of the TEM affects the wavelength of the electron beam, improving resolution with increasing accelerating voltage[27], however resolution is ultimately limited by lens aberrations. Lens aberrations can only be improved by the introduction of correctors such as electron monochrometers (which reduce electron current by throwing away those outside a set energy range) and aberration correctors which significantly increase cost. Beam current control is important to provide good signal to noise, but excess current can cause heating and damage in ultra-thin samples.

3.3.3 STEM

While TEM image formation passes a large beam of electrons through a region of a sample, scanning transmission electron microscopy (STEM) forms an image more akin to SEM. The electron beam is rastered across the thin sample and an image is formed by measuring electron beam current on one of several detectors. Because the electron beam is a focused point rather than a beam, with the detector immediately after the sample, the maximum resolution achievable in such a system is substantially higher than traditional TEM, reaching levels of < 1Å. While STEM's rastering system is beneficial for improving traditional bright-field and dark-field imaging, its major benefit is the addition of the High Angle Annular Dark Field (HAADF) detector for imaging. The HAADF detector is located after the sample at a larger angular deviation in comparison to the small angle scattering used in TEM, this high angle scattering arises due to atomic Z number scattering of the electrons. The resulting image formed by

collecting data with a HAADF detector is a Z-contrast image, with the brighter spots corresponding to higher Z-number atomic columns within a sample. The Z-contrast provided by STEM allows identification of atoms within a crystal structure based upon the relative intensities.

In addition to the Z-contrast imaging available within STEM, the electron beam which passes through the sample has energy losses which are characteristic of the atoms which the beam passed. If a spectrometer is placed below the sample, the energy loss can be measured and a Z-contrast image can be correlated with simultaneous spectroscopic energy loss information, providing chemical pseudo-contrast after post processing. Such a process is known Electron Energy Loss Spectroscopy (EELS).

3.3.3.1 Practical STEM

The preparation conditions for STEM is even more onerous than those for traditional TEM. The electron yield for HAADF imaging and EELS quickly diminishes with increasing thickness of the sample. Samples must be thinned by progressive low energy ion milling to ensure no remaining damage or amorphous layers are present. Such thin layers must also be stored in vacuum and analyzed quickly as such thin samples can quickly react with water and oxygen in air and chemically react or adsorb contaminants.

STEM imaging is most useful when paired with traditional TEM imaging, as phase and diffraction contrast can highlight regions of interest and Z-contrast imaging can examine the fine details at boundaries between such regions. Additionally, combining STEM with 2DXRD and careful sample preparation which maintains orientation relationships can provide absolute crystal orientation information, including polarity of polar crystals.

3.4 Growth Techniques

The work presented in this thesis are prepared primarily by two different growth methods, pulsed laser deposition (PLD) and molecular beam epitaxy (MBE). While these methods are distinct in their properties and the regimes under which they operate, the same material systems were not prepared by both systems, so direct comparisons cannot be made. Nevertheless, the differences between these growth processes will be examined in some detail to provide sufficient motivation for their choice for the given experiments.

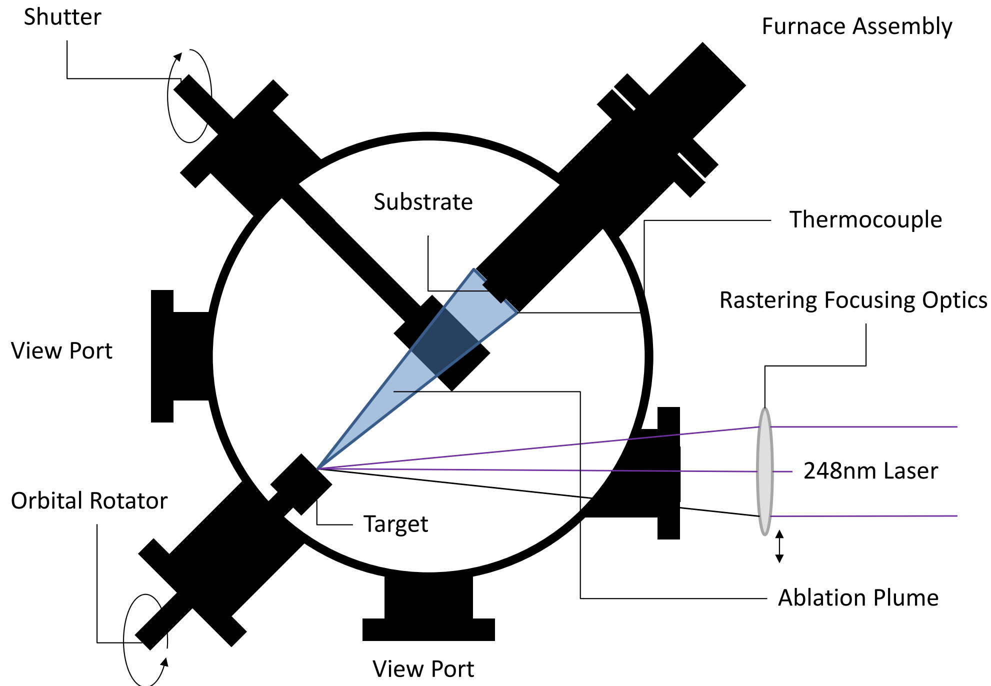

Figure 3.9: PLD Chamber Schematic (used with permission after [28]).

3.4.1 PLD

Pulsed laser deposition (PLD) is a versatile method of growing epitaxial thin films and nanostructures. PLD has the ability to operate in a non-equilibrium growth regime, that is, at a point where the atoms are excited to energies much above the temperature of the growth substrate. Such a regime is achieved by the use of a pulsed, high photon energy and high energy density laser to produce the atomic species used for growth. The properties of the PLD growth system allow a wide range of temperatures, pressures and material types to be used during attempts at epitaxial growths.

The PLD process uses a process known as laser ablation to produce the atomic species used for epitaxial growth. The laser ablation process relies on several key parameters of the laser and to a lesser extent a few material parameters. The lasers used in PLD have pulse widths of < 50 ns, with UV photon energies and total energies of 50—500 mJ/pulse. Typical PLD lasers are excimer lasers with 248 nm UV photons and pulse widths of ~25 ns. Growth rates for PLD are limited by the pulse rate of the laser, and secondarily by the ability of the target to withstand the sustained energy

deposition without melting.

The laser ablation process is achieved by application of laser pulses focused onto a target material, to achieve energy densities > 1 J/cm^2. The photon energy is absorbed within a thin surface layer $1/\alpha$, producing plasmons, excited electrons and excitons[29]. These high energy electrons thermalize and release their energy into the lattice within a few picoseconds. After this thermalization step, the ablation depth is modified by thermal diffusion, highly conductive metals can quickly spread heat up to a micron deep. The deposited energy then results in a pulse of evaporation from the target, called the plume. For highly thermally conductive samples, the surface layer can begin to ablate before the laser pulse is fully absorbed, in these cases further absorption in bulk is screened by the atomic plume[29].

Regardless of the target material, a plume is generated at the laser spot which, due to the laser pulse and heating timescales, is stochiometric with regards to the composition of the target. The atomic plume is also highly ionized, with energies of 1–100 eV and with typical energies of 5–50 eV. The atomic plume is now a vapour but highly compressed next to the target surface. It explodes perpendicular to the surface, expanding across the deposition chamber, to be collected by a waiting substrate. The plume expands from the target with a $\cos^{10}(\theta) - \cos^{20}(\theta)$ dependence, meaning it is highly peaked centrally about the laser spot. Once the atomic plume arrives at the substrate, its energy is delivered to the growing film. The high energy atoms, in addition to having high rates of diffusion, also promote the movement of atoms already present by providing activation energy for their diffusion processes[29]. This is a key reason the PLD process can be used at substrate temperatures lower than other methods, as the atomic plume delivers energy directly to the growing film.

Due to the generation of atomic species using light, the environment surrounding the target and growth substrate need not be ultra-high-vacuum or even high vacuum for the excited plume to successfully traverse the gap between target and substrate. Gas pressures on the order of mTorr can be used to modify the energetics of the atomic plume, reducing the total energy or modifying the distribution[29]. The addition of reactive gasses into the chamber, in addition to participating in plume modification, can also participate chemically in the growth process, allowing the growth of oxides and other gas-incorporating materials. Doping of materials grown with PLD is achievable by incorporating the dopant elements into the existing targets, or by periodically co-ablating pure targets using a target exchange system.

The main limitation of PLD are due to the highly peaked nature of the laser plume, that is, the spatial extent of the atomic plume is limited. The plume must be rastered across large substrate into order to grow a uniform layer. A secondary limitation is the production of macroscopic droplets which can impact the epitaxial growth process. The droplets are produced by several processes, some of which can be mitigated. Targets must be of very high density in order to ensure superheated gasses from voids do not eject pieces of the target. For highly thermally conductive samples (typically metals), the laser pulse can cause sub-surface boiling, resulting in ejection of liquid material from the target. For systems which experience this issue, energy per pulse must be reduced to the minimum which can achieve ablation. A similar process which produces macroscopic droplets is recoil ejection, again for fast conducting materials. As the vaporization shockwave in a target moves into already melted material, the forces can cause a compression and rebound of the liquid material into a macroscopic droplet.

3.4.2 MBE

Molecular beam epitaxy (MBE) is considered the gold standard for the growth of carefully controlled epitaxial thin films and nanostructures, being used for both research and commercial purposes. Its implementation as a growth process allows for a wide range of growth rates from angstroms per second to microns per minute, while controlling the precise ratio of incoming atomic species, and allowing for abrupt changes in composition.

MBE growth systems consist of a large ultra high vacuum (UHV, $<$ 1e-8 Torr) chamber, along with associated load lock system and exchange hardware, which can accept growth substrates of sizes up to several inches. This low pressure environment is essential to the MBE process to ensure a mean free path of larger than the chamber for the atomic beams used during growth. These atomic beams are generated in the chamber by one of two processes, effusion cells, or gas sources. In an effusion cell, a high temperature ceramic containing a solid ultra-pure source of material, is heated to cause evaporation, which then travels in the molecular beam regime across the chamber to a substrate. Effusion cell rates are controlled by the temperature of the cell. In gas sources, an organometallic gas containing the atomic species of interest is passed into the chamber via a “cracker,” a heated filament used to burn the organic components of the gas, leaving the atomic species which travel across the chamber and

are collected on a substrate. Gas source rates are controlled by mass flow controllers adjusting the rate of gas passing into the system. Growth rates of angstroms per minute to micrometers per hour are possible via high flow crackers and industrial growths.

MBE systems are used to grow materials in a wide variety of systems, typically concentrated in the III-V, and can also include a wide variety of electrical dopants during growth. Strict control of the atomic sources allows growth of repeating multilayer stacks, graded materials and quantum structures. In addition to the careful control of the atomic species, MBE's low pressure system allows in-situ monitoring and characterization of the growth surface using electron-based techniques such as reflection high energy electron diffraction (RHEED).

The main limitation of MBE is the ability to only produce a single sample at a time, making it unsuitable for high volume commercial production. Another limitation is the heating and temperature control of the substrate. Since samples must be added via load lock, contact heating and temperature measurement is impractical, leaving only indirect radiative heating and pyrometry temperature measurement.

Part II

III-V Materials on Silicon

Chapter 4

The Role of Vicinal Surfaces in Epitaxial Twin Formation

4.1 Introduction

Since the microelectronics revolution, silicon has been a dominant material for the production of devices for a variety of applications. Silicon has non-ideal properties for a variety of applications but remains dominant due to its well-understood processing parameters and large manufacture install base, providing economies of scale. The III-V semiconductors offer superior properties for a variety of applications when compared to silicon, and are actively used in applications were performance is valued above other considerations, such as military and space sectors. The goal of integrating III-V semiconductors into silicon based microelectronics has spawned extensive research into the processing involved to grow or otherwise electronically attach these materials with minimal defects.

Under auspices of the ARISE Photovoltaics project, the III-V semiconductors GaAs, GaSb, AlSb and InP were grown as thin films under a variety of conditions on single crystal silicon substrates, to examine the growth process and electro-optic properties. The role of the varied lattice mismatch, growth parameters, and substrate properties were examined and several previously undocumented phenomona were examined due to the use of 2DXRD, whose benefits were discussed in Section 3.2.1.

The formation of epitaxial (or growth) twins was found to be a key area where the literature had performed little examination. The role of twins in the formation of electronic defect networks, and the effects vicinal (offcut) substrates had on their formation were thoroughly examined and an explanatory model was developed to explain factors that affect their formation and provide proposed routes towards their minimization and elimination. This work was published as:

G. A. Devenyi, S. Y. Woo, S. Ghanad-Tavakoli, R. A. Hughes, R. N. Kleiman, G. A. Botton, and J. S. Preston. "The role of vicinal silicon surfaces in the formation of epitaxial twins during the growth of III-V thin films". In: *Journal of Applied Physics* 110.12 (2011), p. 124316. ISSN: 00218979. DOI: 10.1063/1.3671022 [30].

This work was completed in close collaboration with Ms. Steffi Woo, now a Ph.D. candidate in Material Science and Engineering at McMaster, with the TEM/STEM work performed exclusively by her, the 2DXRD work performed by me and all other work being collaborative.

4.2 Background

Anti-phase boundaries (APBs) have long been identified as highly detrimental to the electro-optic properties of epitaxial thin films[31]. Extensive research has been performed in the use of vicinal substrates and other means[2] to control the formation and propagation of APBs during the growth of epitaxial thin films. A far more common planar defect during growth are epitaxial twins[32]. Twins are regions of mirrored stacking sequence in the closest packed plane of {111} within a crystal with zincblende structure, where each consecutive layer is shifted after the first bounding stacking fault[33]. These twin defects, often observed through transmission electron microscopy (TEM), have been attributed to a variety of causes, including APBs, threading dislocations and simple stacking faults[34–42]. High resolution X-ray diffraction single peak analysis, which only examines X-ray peaks perpendicular to the substrate surface, will miss the additional peaks due to the presence of twins, leading to their misattribution. Similarly, the sole use of conventional TEM has the disadvantage of being a local measurement, and not representative of the bulk. Further work has definitively noted the key features of twins and provided guides to their identification[32].

The twin has been considered a low-impact defect, due to its coherent interface and lack of dangling bonds, causing only weak scattering due to the minor disruption in the crystal symmetry. This view of twins considers them as isolated in the material, ignoring the fact that in epitaxial films, twins are likely to intersect during growth, as the intersection of twins of different habit planes will lead to unsatisfied bonds. For example, first-order twins formed on opposing habit planes can terminate from mutual intersection along a {114} plane, which is highly incoherent, resulting in unsatisfied bonds and trapped charge[43]. Furthermore, twins which intersect from adjacent habit planes will also form incoherent interfaces on high-order planes. Finally, second- and higher-order twinning interfaces are expected to create dangling bonds, and will result in further unsatisfied bonds between the twinned regions and epitaxial film.

Using the combined techniques of two-dimensional X-ray Diffraction (2DXRD) and conventional TEM, this investigation has demonstrated a strong asymmetric suppression of twins due to the formation of atomic steps on vicinal substrates, previously observed for only GaAs[44–46]. This combination of techniques allows macro and nano/micro characterization which combines to provide a complete analysis of a material system. Twin suppression has been observed in GaAs, InP, GaSb and AlSb

semiconductors grown on vicinal silicon substrates under varying growth conditions. Through the integration of a quantitative reciprocal space mapping from 2DXRD and real-space imaging techniques from conventional TEM, we can understand the structural defects globally as well as their spatial distribution and propagation locally. From this, we propose a comprehensive mechanism for the suppression, which is the asymmetric step-flow overgrowth of twins on vicinal substrates, applicable to all of the III-V material systems examined. Given the detrimental nature of intersection of twins to electrical properties of thin films, this suppression phenomenon has the possibility of greatly improving the electro-optic properties of thin film III-V semiconductors grown on Si.

4.3 Experimental

Semiconductor epilayers (GaAs, InP, GaSb, and AlSb) were deposited on nominal (001)-oriented (±0.5°) and vicinal Si substrates (offcut 4.7° (±0.25°) towards [110]) using a SVT Associates molecular beam epitaxy (MBE) system. As-received epi-ready wafers were cleaned for 1 min in a 4% HF in deionized (DI) water dip followed by a 30 sec DI rinse immediately before to their insertion into the MBE load-lock. Before film deposition, both the nominal and vicinal Si(001) substrates underwent a 15 min degassing procedure at 350℃ followed by a thermal treatment at 800℃ for up to 5 min, to reconstruct the Si surface into single domain terraces[19, 47–49]. Few single steps are expected to remain on vicinal substrates, and a higher number on nominal substrates because of the larger terrace length. Growth conditions followed established protocols[42, 50, 51] and yielded comparable rocking curve full-width half-maximum for the [004] reflection using HRXRD. AlSb epilayers were grown to a thickness of 550 nm with a 20 nm GaSb capping layer to avoid oxidation. GaAs epilayers were grown to a thickness of 600 nm and GaSb to a thickness of 500 nm. InP samples were grown at 470℃ with a V/III flux ratio of 2.0 at a growth rate of 1 μm/hr, resulting in a thickness of 600 nm. HRXRD and TEM data also revealed that all films are fully relaxed by a network of interfacial misfit dislocations[52]. GaSb samples were grown in the presence of a 5 nm AlSb buffer layer, as prescribed by Akahane et al.[50]

Stereographic pole figures were generated for each sample using 2DXRD techniques. A Bruker SMART 6000 CCD detector on a Bruker 3-circle D8 goniometer (Bruker AXS Inc., Madison, WI) with a Rigaku RU-200 rotating anode X-ray generator (Rigaku

MSc, The Woodlands, TX) and parallel-focusing monochromator optics was used for the data collection. Scans were taken with the detector centred on the (111) 2θ of the material of interest and the sample rotated through 360° in 0.5° increments about the surface normal of the sample. A 1D integration of all frames was used to determine the combined width of the (111) peaks using MAX3D software (McMaster University)[53]. The peak width was then used to integrate (111) reflections from all frames, including a background and absorption correction for the corresponding material with GADDS (Bruker-AXS) software, resulting in a pole figure. Pole intensities were obtained from pole figures using a circular integration cursor with a 10 pixel radius which was centred on the pole such that the maximum total intensity was captured. All pole intensities were corrected for structure factor and frame exposure times.

For each sample two {110} TEM cross-sections were prepared, one parallel to the [110] miscut direction and the other perpendicular. The specimens were prepared by the standard procedure of mechanical polishing, dimpling, and ion-milling (4 keV Ar-ions at an incident angle of ±4° using a liquid nitrogen cold stage for InP) until perforation. Crystallographic information of the epitaxial layer was obtained using diffraction contrast imaging with a Philips CM12 conventional transmission electron microscope (TEM) operated at 120 kV and equipped with a LaB_6 filament. In addition, electron diffraction analysis was performed using selected area electron diffraction (SAD).

4.4 Results

Figure 4.1 shows the {111} pole figures generated from 2DXRD data. The pole figures presented here are a stereographic projection of the (111) X-ray reflections of all orientations of the material of interest, oriented with the top of the figure corresponding to the [110] direction of the substrate. The pole positions indicate that each of the III-V materials have the same symmetry and have variations of one orientation relationship with the Si substrate. For each of the III-V films, the pole figures indicate a dominant [100]-orientation, as well as four weaker orientations associated with twins having (111), $(1\bar{1}1)$ $(\bar{1}\bar{1}1)$ and $(\bar{1}11)$ habit planes, as indicated by a single shared pole (and hence a shared plane) between the bulk film and each twin variant. A simulated pole figure, indicating the origin of each pole is labelled and given in Figure 4.2. The experimental pole figures differ from the simulation due to instrumental broadening of

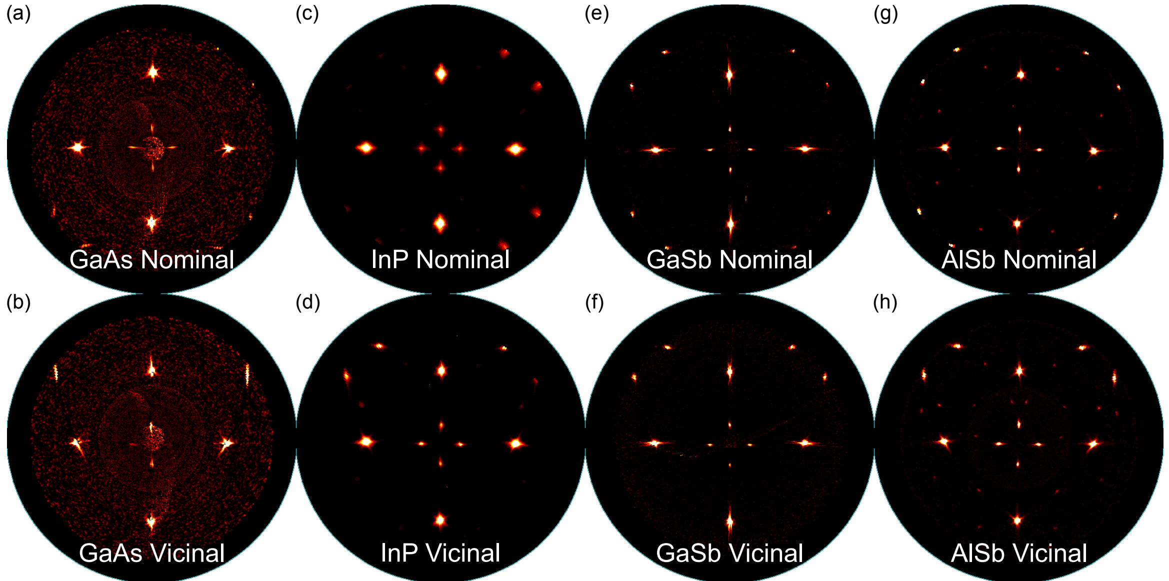

Figure 4.1: Stereographic {111} pole figures generated from 2DXRD show a bulk (100) phase plus four twinned variants as identified in Figure 4.2. Twin variant intensity is asymmetric for vicinal substrates.

poles, and in that the AlSb and InP pole figures show second-order twinning, which is not included in the figure in an effort to maintain clarity. The outermost poles are partially visible in the experimental pole figures due to limitations of the measurement range of samples in reflection, combined with substrate tilt tolerance. The background of Figure 4.1(a) and (b) is higher due to the weaker X-ray scattering from GaAs. For films grown on vicinal substrates (Figure 4.1(b),(d),(f),(h)) the centre of symmetry of the pole figure is shifted away from the tilt direction, i.e. towards the step edge. Figure 4.3 shows the corrected measured and normalized intensity of the unique twin poles, as labelled in Figure 4.2. Measured intensities are normalized to the maximum value of pole intensity for each pole figure. On nominal substrates, pole intensities are equal within experimental uncertainty and hence the twin volume fraction is equal for all four <111> twin plane directions. Films grown on vicinal substrates, show a 50–75% reduction in the volume fraction of the twin forming opposite to the step direction of the (111) habit plane (Pole 3). The overall intensity of poles does not increase on vicinal substrates, as seen in the corrected intensity plot of Figure 4.3(a), indicating no overall increase in twinning due to vicinal substrates. Conventional cross-sectional TEM measurements indicate that microtwins are visible for all four of the III-V material systems studied. Selected area electron diffraction (SAD) patterns

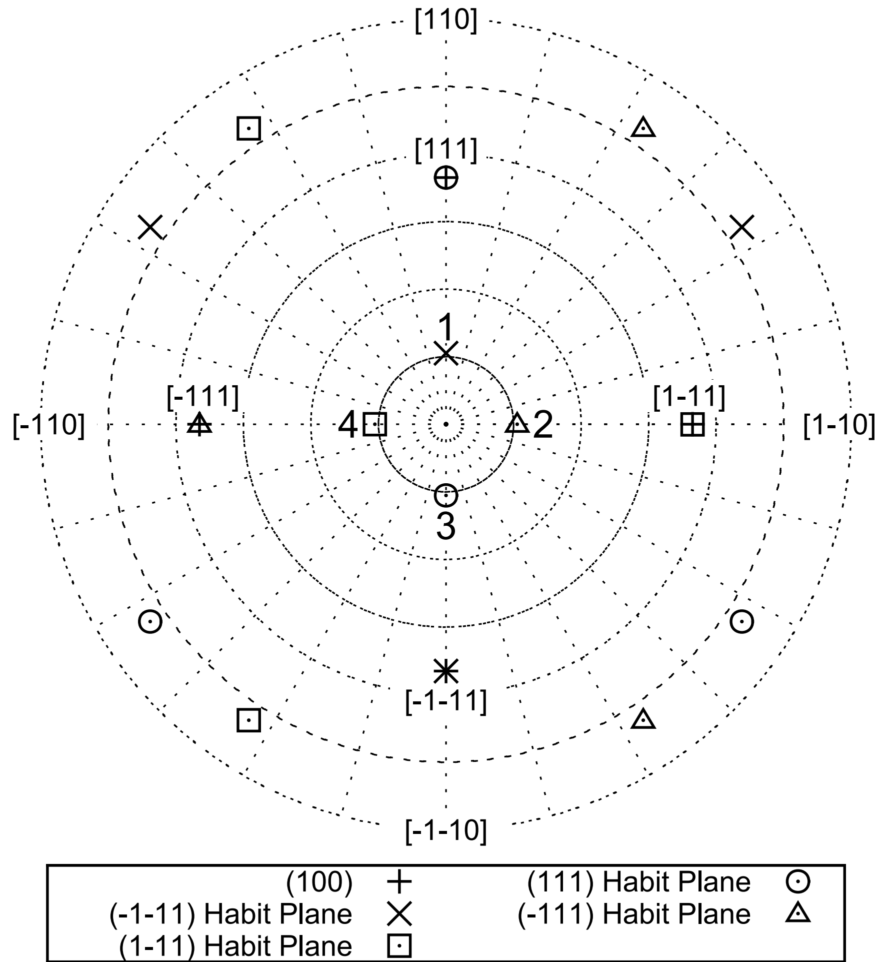

Figure 4.2: Simulated {111} pole figure for a cubic III-V semiconductor film deposited on nominal silicon substrate. The pole figure containing poles from the dominant [100] film orientation film and from the 4 primary twins along their associated habit plane. The poles associated with each orientation are labelled with unique markers for use in the intensity measurements (Figure 4.3), and labels on the edge of the pole figure indicate absolute crystal directions of the silicon substrate. All poles from Figure 4.1 are accounted for, although second-order twin poles are omitted for clarity.

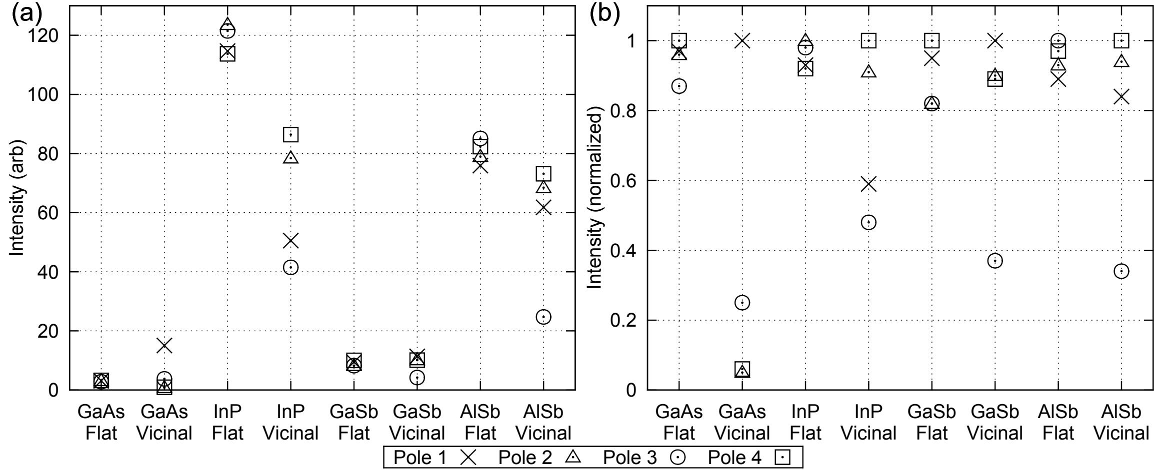

Figure 4.3: (a) Corrected (via structure factor and exposure time) and (b) normalized intensity of twin poles (as labelled in Figure 4.2 above). The normalized X-ray intensity shows a strong reduction in Pole 3 for all vicinal substrates.

of areas containing microtwins cause additional twin reflections in the form of streaks or spots in positions mirrored across the twin plane direction. Analysis of the SAD patterns indicates that the twin variants in the GaAs epilayers are highlighted in strong contrast with dark-field (DF) images formed by isolating only the twin reflection of the dominant variant in the diffraction pattern (Figure 4.4(a) and (d)). In comparison to their complementary DF images, where no particular twin variant is highlighted (Figure 4.4(b) and (e)), the preferential twinning direction is clearly present in GaAs grown on vicinal substrates. This is also true for GaSb grown on vicinal substrates, as shown in Figure 4.4(f). The asymmetry in twinning directions for vicinal substrates is evident when examining their spatial distribution, as well as propagation into the epilayer with conventional TEM. The preferential twinning direction along $(\overline{1}\overline{1}1)$ planes away from step edge (Pole 1) induces microtwins that propagate deep into much of the epilayer thickness, as indicated by microtwins with bright contrast in the DF image of GaSb and GaAs shown in Figure 4.4(f) and (d). The intrinsic asymmetry to a vicinal substrate becomes obvious when viewing perpendicular to the tilt direction of [110]. The two edge-on {111} twin habit planes, namely $(\overline{1}\overline{1}1)$ and (111) now lie 59.4° (54.7° + offcut angle) and 50° (54.7° − offcut angle) from the interface. The reduction in peak intensity of Pole 3 from 2DXRD can now be explained by the TEM image of the representative variant, shown in Figure 4.5, which propagates ∼25 nm from the interface and is small in width as visible in cross-section. In addition,

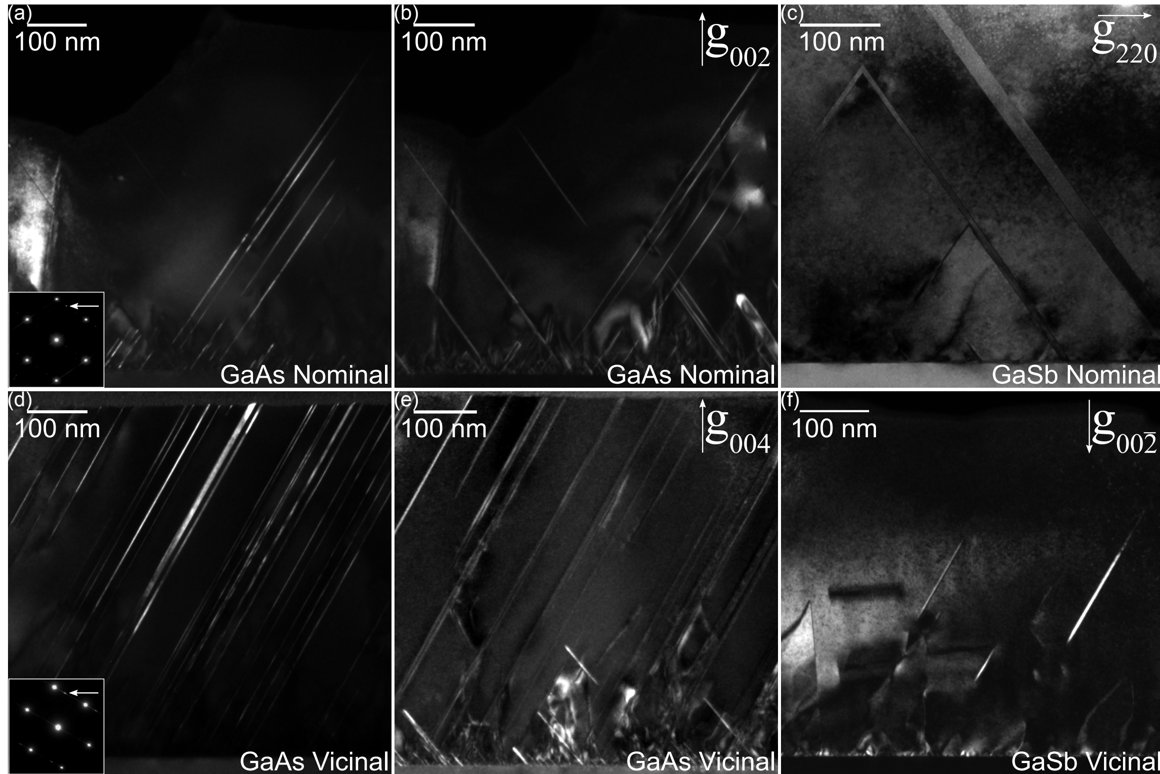

Figure 4.4: Conventional TEM images of the $[1\bar{1}0]$ cross-section, (a) GaAs Nominal DF image of variants with $(\bar{1}\bar{1}1)$ twin habit plane; (b) GaAs Nominal DF image of the same area as (a); (c) GaSb Nominal BF image; (d) GaAs Vicinal DF image of variants with $(\bar{1}\bar{1}1)$ twin habit plane; (e) GaAs Vicinal DF image of the same area as (d); (f) GaSb Vicinal with the preferential twinning direction of $(\bar{1}\bar{1}1)$ away from step edge (Pole 1), as indicated by microtwins with bright contrast in this DF image; step edge direction is towards the right for all vicinal images.

the in-situ RHEED pattern showed a transition from a spotty to a streaky pattern after nearly the same film thickness had been grown, indicating a change in surface morphology.

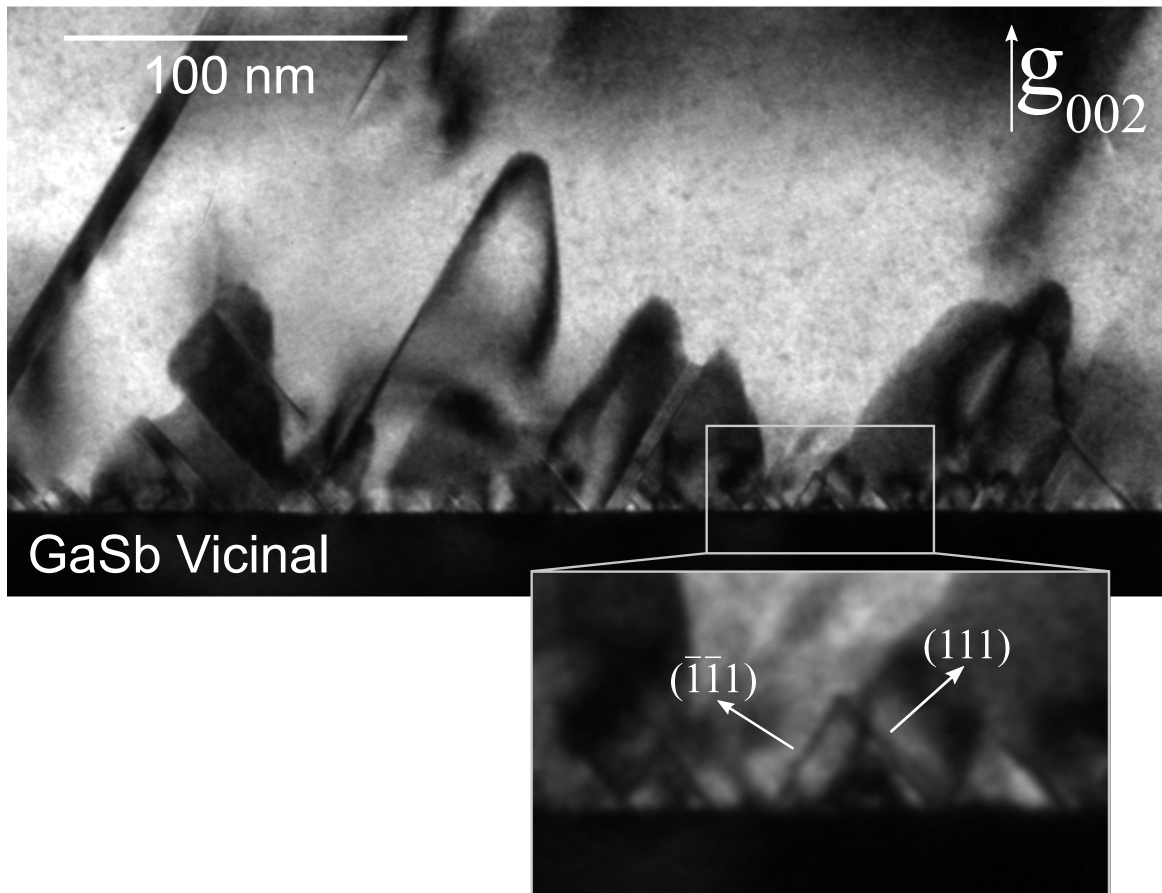

Figure 4.5: Conventional TEM DF image of the $[1\bar{1}0]$ cross-section of GaSb Vicinal, depicting the nanotwins close to the interface, of the twinning direction of (111) towards the step edges (Pole 3). The black “n”-shaped loops in this DF image formed with a super-lattice reflection are APBs, as described by Woo et al.[54] Step edge direction is towards the right of the image.

4.5 Discussion

Island nucleation followed by coalescence (i.e. the Volmer-Weber growth mode) is frequently observed for III-V thin films[32, 50, 55, 56]and is, in fact, anticipated for the growth parameters used in our film growths. Both substrate strain and interfacial energy play a strong role in determining the size of the initial islands during nucleation. After their initial formation, subsequent island growth occurs on the {111} planes, creating pyramidal structures which grow both laterally and in height. For III-V systems, stacking along the <111> directions consists of alternating layers of group III- and group V-terminated surfaces, where two of the exposed surfaces are (111)A with Ga triply bonded, and the other two are (111)B with As triply bonded. These two types of surfaces assemble at different rates. Such a growth mode can continue indefinitely, but often transforms into a layer-by-layer growth once some critical thickness is achieved[57]. Epitaxial twins occur when atoms stacked on a {111} plane shift from their designated positions during growth, resulting in a stacking fault, characterized by a 180° rotation in bond directionality about the plane normal. Atoms bonded to the next layer are likely to follow the stacking order defined by their nearest and next-nearest neighbour and continue the stacking sequence set out after the stacking fault, creating a rotation twin of the first region. A subsequent stacking fault will then rotate the next layer back to its original orientation, bounding the twinned region. The stacking fault energy (SFE) for a system is the measure of how costly it is for a single crystal plane to be misordered from its expected stacking sequence.

The total volume (V) of all twins in a film is given by Equation (4.1) and schematically shown in Figure 4.6:

$$V \cong \sum_{1}^{N} L w_1 w_2 \sin(54.74°) \tag{4.1}$$

The first factor impacting the volume of twins in an epilayer is the number of twins (N). This parameter is driven primarily by the SFE, but can also be influenced by the number of nucleation sites. Atomic registration errors on {111} growth planes are expected to occur fairly frequently, as their probability is inversely proportional to the SFE, and SFE is only a fraction of the average thermal energy of an atom during growth[32]. The formation energy of stacking faults is critical to the formation of microtwins, this is to say that when this energy is lower, the probability of a stacking

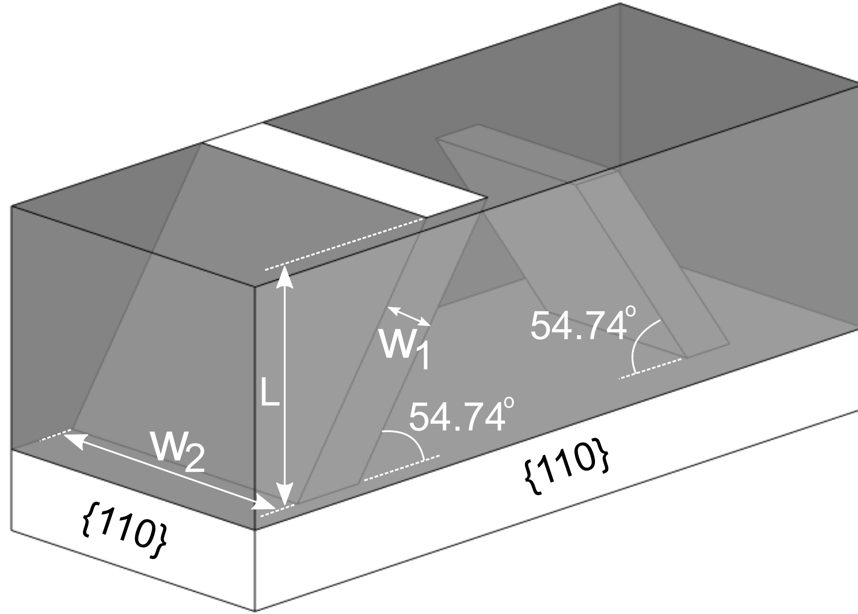

Figure 4.6: Two twins on a nominal surface, embedded within a film. Twin dimensions with widths (w_1,w_2) and length (L) are labelled.

fault, and hence twin formation, increases[58]. Higher assembly rates on the fault plane can also lock in stacking faults that could otherwise be corrected in order to minimize energetics. The second factor, L, is the vertical length that the twins propagate through the epilayer, a value that generally is the full thickness of the epilayer. The last two parameters impacting twin volume are the width in (w_1) and perpendicular to (w_2) the fast-growth direction. The width of the twin in the growth direction is determined by the interplay between the SFE and the assembly rate of that plane. The twin width perpendicular to the growth plane is determined by the size of the island in that dimension, which is influenced both by the chemistry and misfit of the epilayer-substrate interaction.

Given the role parameters play in twin volume fraction, it is now possible to account for the differences between the different III-V semiconductor films grown on nominal (001)-oriented Si substrates. The most obvious difference is the mean volume of twins, with InP standing out as having the largest value. This can mainly be attributed to the low value of 17 meV/atom for its reduced SFE (the energy per atom in a fault plane)[59], as compared to the larger values of 47 and 53 meV/atom exhibited by GaAs and GaSb[59]. It is noted that the SFE for AlSb has not been reported, but is expected to be similar to that of GaSb due its similar ionicity[60]. The higher mean

value exhibited by AlSb is due to its higher nucleation density[50], which leads to a greater number of islands where each has the possibility of forming twins.

In all III-V films grown on vicinal substrates, there is a 50–75% reduction in the volume of twins contributing to Pole 3. This corresponds to a substantial reduction in twin formation opposite to the tilt direction. GaAs, however, is unusual in that it exhibits a strong reduction in twins for directions perpendicular to the step direction (Pole 2 and 4), and an increase in twins towards the tilt direction (Pole 1 >> Pole 3). The TEM studies of Xie et al.[45] on GaAs epilayers grown on vicinal Si substrates observed with conventional TEM correlate well with our observations of As-initiated vicinal GaAs films. Irrespective of the rotation in tilt direction to the perpendicular <110> between Xie's work and the work presented here, the same very low density and equal distribution of microtwins with {111} habit planes perpendicular to the tilt direction (Pole 2 and 4) is evident. Xie's work proposed preferentially oriented island nucleation, and claimed that the asymmetric distribution of microtwinning is due to the two (111)B planes that are aligned with the offcut exhibiting a faster growth rate. The reductions in the Pole 2 and 4 twin variants are not observed for the other III-V systems (i.e., InP, GaSb, and AlSb), indicating that the fastest-growing plane cannot be solely responsible for such reductions. The single domain nucleation achieved by Xie due to Ga and As equal bonding preference to Si[61] cannot be guaranteed in other systems due to the lower bonding affinity of Sb[62] and P[63]. These other systems instead show a behaviour in the distribution of microtwins that is a combination of the As-initiated and Ga-initiated GaAs, as demonstrated by Xie, indicating mixed domain nucleation (both group III and V atoms as first atomic layer species). Despite the effort to use a group V-soaking before growth, the high affinity of group III atoms for Si can easily displace any weakly bonded group V atoms, especially at higher growth temperatures. In growths of group III-initiated nucleation, the fastest growing planes remain as group V planes, but are rotated to the two perpendicular {111} orientations not under the influence of the substrate offcut asymmetry, as claimed by Xie. Therefore, in the event of mixed domain nucleation, the asymmetric preferential growth of microtwins tilted towards the tilt direction in III-Vs grown on vicinal Si cannot be attributed exclusively to the faster growing group V planes.

Previous work by Wei and Aindow[44] on GaAs epilayers on vicinal Si concludes that under a balanced Ga- and As-initiated flux, it is expected to achieve layer-by-layer growth. They proposed that the high density of twins with habit planes towards the

tilt direction in combination with less twins on all other habit planes is due to the deformation resulting from the residual misfit associated with the heteroepitaxy. The critical resolved shear stress (i.e. the threshold value of stress necessary to cause atomic planes to slip) as calculated by Wei and Aindow[44] along the <112> slip direction in the {111} planes towards the tilt direction is over 4% higher than all other slip systems. This means the likelihood of slip in this direction is lower, so deformation twins would more likely form. This slip direction is not one of the two contributing partial dislocations (from the dissociation of a perfect dislocation along an interfacial <110> direction) responsible for the formation of a stacking fault common in such epilayers. Therefore the twins observed cannot be exclusively or even primarily be due to deformation, as their asymmetric distribution cannot be explained by the anisotropy in resolved shear stresses alone.

Comparing nominal and vicinal samples for all systems, the vicinal substrates increase the mean intensity of twins, which can be attributed partially to an increased number of preferential nucleation sites during initial growth, thus increasing the number of twins (N), which can form. Next, vicinal substrates enhance the fraction of twins with $(\bar{1}\bar{1}1)$ habit planes oriented towards the tilt direction in GaAs, which is not observed for GaSb, AlSb and InP. This phenomenon is evident in both the 2DXRD intensity of Pole 1 (see Figure 4.3(a)) and the DF TEM image (see Figure 4.4(d)). The work of Xie et al. also shows that the As-initiated GaAs growth induces an exclusively As-prelayer which leads to a domain in which (111)B surfaces are on (111) and $(\bar{1}\bar{1}1)$ aligned with the step direction. The high assembly rates of those planes increase the probability of errors in the form of stacking faults, which, in turn, increases the total number of twins nucleated (N). While in the case of mixed domain nucleation with GaSb, the enhancement in the $(\bar{1}\bar{1}1)$ fast-assembly surface is diluted by the even distribution to the adjacent $(1\bar{1}1)$ and $(\bar{1}11)$ planes of equal assembly rates. Because of this, fewer stacking errors occur in the $(\bar{1}\bar{1}1)$ and (111) planes, and the number of twins nucleated along those planes are decreased. The effects of this enhancement in the fraction of twins in III-Vs (including GaAs) is expected to be less pronounced with increasing growth temperature, where the group V-prelayer atoms are more likely to desorb, causing mixed nucleation and results which are more comparable to those of GaSb and AlSb. The presence of single steps on vicinal substrates can also affect this enhancement phenomenon, as they cause a rotation of domains, which result in APBs. The strong asymmetry in GaAs samples indicates that the Si substrate preparation

results in mostly double-stepped vicinal substrates.

The sum of the four reflection intensities for GaSb grown on vicinal substrates is close to two times higher than for GaAs grown on vicinal substrates. This is evident when comparing the width of twin domains with (111) and ($\bar{1}\bar{1}1$) habit planes in GaSb grown on nominal and vicinal Si substrates which are about two times as wide as those in GaAs, as shown in Figure 4.4(c) and (f), demonstrating an overall increase in the volume fraction of those twin variants. The width of twins in GaSb grown on nominal and vicinal Si substrates with two ($1\bar{1}1$) and ($\bar{1}11$) habit planes are also about three times as wide as those in GaAs.

The proposed mechanism for the reduction of twins is the transition to a step-flow growth mode induced by vicinal substrates. On nominal oriented substrates a transition to layer-by-layer growth allows for the continued propagation of nucleated epitaxial twins throughout the film as the growth front propagates normal to the substrate. In some systems on nominal substrates, layer-by-layer growth is never achieved, as is observed for InP and AlSb. On vicinal substrates, growth does not transition to a pure layer-by-layer growth mode but instead to a step-flow growth mode, due to the steps present on the underlying substrate. From the transition point onwards, the growth front is not normal to the substrate, but instead flows across the surface at an enhanced rate towards the tilt direction. This enhancement can also increase the fraction of twins forming in the step-flow direction as is the case for GaAs grown on vicinal substrates. Growth fronts originating from the steps flow across the surface and overgrow islands that formed during the initial island growth mode. Since step-flow growth occurs down steps, towards the tilt direction, twins which were initially nucleated on habit planes away from the tilt direction during island growth are halted since they need to propagate opposite to the growth front. The transition from island to step-flow growth is evident due to the presence of nanotwins which propagate $\sim$25 nm from the interface before termination, as shown in the GaSb TEM DF image (Figure 4.5). This propagation distance into the film thickness is consistent with the transition from an island to step-flow growth mode as is apparent from the observed transition from a spotty to streaky RHEED pattern during the GaSb growth. The transition to step-flow growth ultimately decreases the propagation length (L), of the twins with habit planes opposite to the tilt direction.

Greater vicinal angles are expected to initiate step-flow growth from nucleation, and hence eliminate twins opposite the tilt direction. An offcut towards the [100] direction

can induce surface steps in the two orthogonal <110> directions simultaneously[55], which is expected to decrease the twin density in two of four {111} habit planes, reducing the overall intersections of microtwins that do so along incoherent interfaces.

4.6 Implications for Symmetry and Energy at Epitaxial Surfaces

The growth of polar semiconductors, particularly the III-V on non-polar substrates such as silicon has presented significant challenges. Besides the obvious issues regarding the intrinsic lattice mismatch between these epilayers and the proposed substrate, the uniform energy surface presented by a non-polar surface provides a poor template for the nucleation of polar semiconductors, introducing numerous electrically active defects. Intentional symmetry breaking through the use of vicinal substrates provides a route to improve the quality of thin films, and to control the formation of defects.

By breaking the symmtery on the (100) silicon surface through the use of vicinal substrates, an important change occurs on the energy landscape for a growing crystal, improving the overall quality of the film. As has been documented numerous times in literature, vicinal substrates reconstruct at high temperatures in order to present the closest low energy (low index plane) surface, separated by atomic height steps. When the offcut angle is sufficiently large, and the temperature processing sufficiently aggressive, the vicinal substrate reconstructs to present the same sublattice layer, separated by double height steps. This uniform sublattice layer presents a chemical energy landscape for the incoming polar semiconductor atoms which results in the preferential nucleation of one of the two constituents, resulting a substantial or complete elimination of anti-phase boundaries.

The microtwinning observed in III-V compounds in literature had been ignored due to the assumption that twin interfaces are low-energy and non-defective. The interaction of multiple twins on different habit planes however, has been demonstrated to present an incommensurate boundary between the two crystallites resulting in electrically active defective bonds. By breaking the symmetry on the (100) silicon surface, growth twins, which frequently travel through the entire grown film, can be suppressed or limited to an interfacial region. The introduction of the reconstructed vicinal surface presents step edges where adatoms are more likely to nucleate, overgrowing twins

which spontaneously form during nucleation, confining the defects to a thin interface region.

While these results were not of immediate use to the ARISE project, due to the device of interest being a solar cell with vertical transport, horizontal transport devices grown epitaxially on silicon may benefit from the reduction in twin collisions forming in their active regions. The twin suppression results here also point towards two future areas which may yield further improvements, larger offcut angles and different offcut directions.

Larger offcut values for vicinal substrates are known to increase the density of step edges to the point where the surface reconstructs to another low index plane. Higher density steps are expected to increase the nucleation rate at edges, resulting in enhanced step flow, and further suppression of twinning. Offcut directions other than [110], specifically 45° between [110] and [211] will result in atomic reconstruction of the surface into two dimensional terraces with step edges along [110] and [211] directions. Such two dimensional terraces could allow step flow growth and hence suppress twinning in two perpendicular directions, resulting in further reductions in twin collisions and reduction in defect density.

Chapter 5

Tilted Epitaxy on (211) Oriented Substrates

5.1 Introduction

In parallel to the investigations of vicinal (100) substrates, the ARISE project investigated alternative substrate orientations including (111) and (211) silicon due to the previously outlined issues with (100) silicon. While the results of (111) substrates were disappointing, the growth of thin films on (211) substrates demonstrated several interesting properties. Most interesting amongst these was the spontaneous tilting of thin films grown on top of (211) oriented silicon substrates. Such tilting had been remarked upon previously in literature, but no comprehensive examination of its origins or relationship to material parameters had been examined.

In this work, also done in close collaboration with Ms. Steffi Woo, the spontaneous tilting of thin films grown on (211) oriented silicon substrates was examined. The effects of the naturally asymmetric substrate was found to cause a tilt of the growing thin film to minimize the strain across the interface. Using this idea of projected strain minimization across the interface, a model was developed which predicted the tilt as a function of intrinsic lattice mismatch between the substrate and thin film. Examination of the reports of thin film tilting in literature showed the model successfully calculated tilt for nine material systems and made predictions for those systems for which no measured values had been reported. This work was published as:
S. Y. Woo, G. A. Devenyi, S. Ghanad-Tavakoli, R. N. Kleiman, J. S. Preston, and G. A. Botton. "Tilted epitaxy on (211)-oriented substrates". In: *Applied Physics Letters* 102.13 (2013), p. 132103. ISSN: 00036951. DOI: 10.1063/1.4799278 [64].
This work was completed in close collaboration with Ms. Steffi Woo, with the TEM/STEM work performed by her, the 2DXRD work and preparation of the numerical model performed by me, and all other work being collaborative.

5.2 Background

The (211) orientation of non-polar semiconductor substrates, most notably silicon, has several beneficial properties. Of most relevance to the epitaxy of thin films on Si(211) substrates is the occurrence of two energetically non-equivalent lattice sites on the surface, without the need for surface reconstruction[65]. These two non-equivalent lattice sites offer preferential nucleation locations for the individual adatoms during growth of polar (group III-V and II-VI) semiconductors. Such preferred nucleation is

proposed to eliminate the occurrence of anti-phase domains (APDs) during the growth of polar semiconductors[65] while also maintaining the interface neutrality condition of h±k±l=0[65]. The intrinsic asymmetry of the (211) surface is also expected to influence the formation of epitaxial twins during growth[30]. Si(211) substrates have been used to produce the highest quality CdTe[66], ZnTe[67] and HgCdTe[68] despite large lattice mismatches of 19.4%, 12.3%, and 19.1%.

Thin films grown on (211) substrates have been previously observed in literature to have a tilted epilayer orientation relative to the substrate[66, 68–71]. The tilt phenomenon has been attributed to a number of causes by different authors including the glide and interactions of misfit dislocations [72–75] and localized distortion of the lattice at the interface[76]. The mechanisms proposed thus far have been unsuccessful at predicting the tilt of mismatched epilayers over large range of mismatch (0–20%) found in III-V and II-VI material systems. A phenomenon intimately intertwined with tilted epitaxy is "dual epitaxy," observed by numerous authors[70, 71, 77, 78] that mismatched CdTe on GaAs(211) epitaxy can result in films growing in a twinned orientation, combined with a tilt; such that the (133) planes make up the epilayer surface and are parallel to the substrate (211) planes. The tilt component of dual epitaxy is same tilt phenomenon examined here.

5.3 Experimental

GaSb epilayers were deposited on nominal (211)-oriented (±0.5°) using a SVT Associates molecular beam epitaxy (MBE) system. As-received epi-ready wafers were cleaned for 1 min in a 4% HF in deionized (DI) water dip followed by a 30 sec DI rinse immediately before their insertion into the MBE load-lock. Before film deposition, substrates underwent a 15 min degassing procedure at 350℃ followed by a thermal treatment at 800℃ for up to 5 min, to reconstruct the Si surface. Growth conditions followed established protocols[42, 50, 51] at 600, 640 and 500℃.

Stereographic pole figures were generated for each sample using 2DXRD techniques. A Bruker SMART 6000 CCD detector on a Bruker 3-circle D8 goniometer (Bruker AXS Inc., Madison, WI) with a Rigaku RU-200 rotating anode X-ray generator (Rigaku MSc, The Woodlands, TX) and parallel-focusing monochromator optics was used for the data collection. Scans were taken with the detector centred on the (111) 2θ of the material of interest and the sample rotated through 360° in 0.5° increments about the

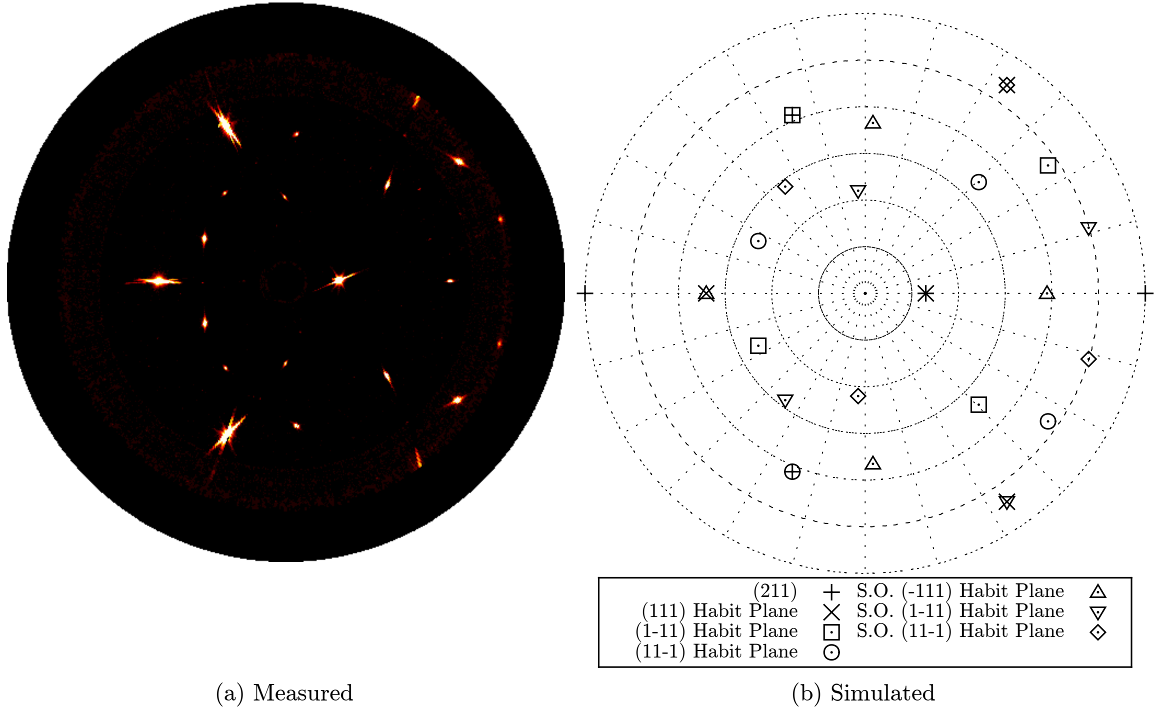

(a) Measured (b) Simulated

Figure 5.1: a) 2DXRD Stereographic pole figure and b) accompanying modelled pole figure, identifying the origin of each peak in the pole figure from the bulk or one of six twin variants. Overlapping peaks indicate twinning habit planes. Outermost poles are partially visible due to experimental limitations. Streaking in peaks is due to instrumental broadening. (S.O. = second-order twinning).

surface normal of the sample. A 1D integration of all frames was used to determine the combined width of the (111) peaks using MAX3D software (McMaster University)[53]. The peak width was then used to integrate (111) reflections from all frames, including a background and absorption correction for the corresponding material with GADDS (Bruker-AXS) software, resulting in a pole figure.

5.4 Results

2DXRD data was processed into a GaSb (111) pole figures as shown in Figure 5.1. Modelling of the poles present indicate that there are seven phases of GaSb, the bulk (211) orientation of GaSb and six twin variants, three first-order twins and three second-order twins from the twin variant with (111) habit plane, with 58%, 21% and 2% of the intensity (and hence volume fraction) present in the twinned orientation for the films presented here. Volume fractions were determined by integration of the sum of

intensity of unique (111) X-ray peaks from all twinned orientations, and divided by total intensity of all unique (111) reflections (sum of bulk and twin intensities), performed using *Bruker GADDS*. There are two distinct nomenclatures used in literature to describe phases present in epitaxial films[70, 75, 79, 80]. One method describes the crystallographic direction which is normal to the surface for each phase, while the other (which the authors choose to use here) describes the nature of the crystallographic orientation relationship between the secondary phases with respect to the orientation of the substrate. Where reference is made to literature using the first, descriptions will be translated into the second for ease of comparison.

Indexing of the crystal unit cells present in the film was performed using *Bruker APEXII* single crystal refinement software, to obtain orientation matrices for the Si substrate as well as the seven GaSb phases. The bulk thin film orientation matrix was then compared to the substrate matrix and a tilt calculated using *orilib* a crystal orientation calculation library, yielding a tilt of 2.65°, 2.55° and 2.40° ± 0.2° about the $[01\bar{1}]$ direction towards $[\bar{1}11]$, these values are indistinguishable within experimental error. The (111) habit plane twin formed in these films is also tilted with respect to the substrate, by the same angle as the bulk, this is expected by crystallography, since this twinned orientation shares extended interfaces with the bulk orientation.

Two transmission electron microscopy (TEM) cross-sections were prepared, in orthogonal directions of $[0\bar{1}1]$ and $[1\bar{1}\bar{1}]$. The specimens were prepared by conventional mechanical polishing and ion milling, and examined as described in Woo *et al.*[81] Conventional TEM imaging of the $(0\bar{1}1)$ cross-section of the epilayers, combined with the selected area electron diffraction (SAED) pattern of the $[0\bar{1}1]$ zone axis as shown in Figure 5.2 confirms the presence of microtwins with (111) habit planes. These microtwins are observed in the perpendicular $(1\bar{1}\bar{1})$ cross-section as large bands lying parallel to the interface over a long-range, alternating with the epitaxial variant (not shown). The observed misorientation between the GaSb and Si reflections in the $[0\bar{1}1]$ SAED pattern also indicate a tilted epilayer (both epitaxial and twin variants) with a tilt of 2.54° ± 0.2° towards the $[\bar{1}11]$ direction. The 133 reflection of the twinned GaSb nearly coincides with the Si substrate normal 422 reflection. The GaSb twin variant can be differentiated in real space by selective dark-field imaging formed using one of the twinned reflection spots. The jagged features at the GaSb/Si interface (seen in detail in the inset of Figure 5.2) only belong to the epitaxial variant. This is indicative of the presence of misfit dislocations at the portions of the interface where the epitaxial

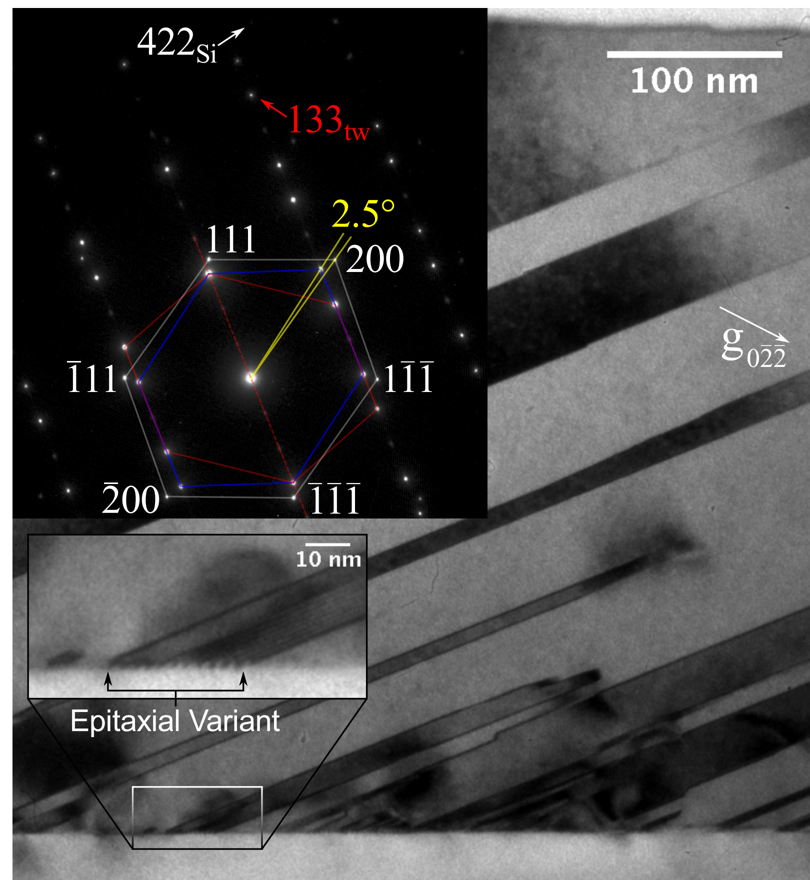

Figure 5.2: Conventional TEM image of the $(0\bar{1}1)$ cross section, with inset diffraction pattern of the epitaxial and (111) habit plane twin variant in blue and red, and inset higher-magnification of the epitaxial variant showing misfit dislocations.

region meets the substrate, as characterized by Vajargah *et al.*[82]

5.5 Discussion

Analysis using an atomic ball-and-stick model, along with trigonometric modelling of lattice plane spacing, can be used to show that the tilted epitaxy reduces the projected in-plane lattice strain along one dimension for the GaSb/Si system. Figure 5.3 shows the alignment of planes present in the epitaxial and twinned variants of the GaSb epilayer. The Si(111) plane spacing (in red) at an angle of 19.471° to the Si(211) surface is aligned to the GaSb(111) plane spacing (in blue), by a tilt of 2.50° in the epilayer. The relationship describing zero projected strain condition between these planes across the interface is described in Equation (5.1), where a_{Sub} is the substrate lattice constant and a_{film} is the film lattice constant, and where δ is the tilt angle. The specific case of $a_{Sub} = a_{Si}$ and $a_{Film} = a_{GaSb}$ describes the material system examined here. This relationship (dot-dash line) also applies over the full range of common heteroepitaxial lattice mismatches grown on (211) substrates, from GaP/Si to CdTe/Si, as shown in Figure 5.4.

$$\frac{a_{film}}{\sqrt{3}\sin(19.471^\circ + \delta)} = \frac{a_{Sub}}{\sqrt{3}\sin(19.471^\circ)} \quad (5.1)$$

$$\frac{a_{film}}{2\sin(74.207^\circ + \delta)} = \frac{a_{Sub}}{\sqrt{3}} \quad (5.2)$$

In the twinned orientation, the Si($\bar{1}$11) plane spacing is aligned to the projection of the GaSb(200)$_{tw}$ plane spacing (both in black) onto the GaSb/Si interface, by a tilt of 2.22°. The geometrical constraints of these planes can be described by the relations as expressed in Equation (5.2). The line of zero projected strain for the twinned region is also shown in Figure 5.4 (dotted line). The applicability of Equation (5.2) is considerably more limited across heteroepitaxial systems, as the constraints described by Equation (5.1) also needs to be simultaneously satisfied as extended interfaces are shared. However, an equivalent relationship describing another set of planes for other lattice mismatches may replace the relationship described by Equation (5.2). The proposed ball-and-stick atomic model (Figure 5.3) also shows that the Ga- and Sb-atoms in the twinned variant are perfectly registered with the terrace (T) and edge (E) atoms of the Si substrate. The epitaxial variant interface is distorted, and the same atomic registration of Ga- and Sb-atoms to the underlying Si substrate does not occur, however the projected sublattice is still aligned. This correlates well with the

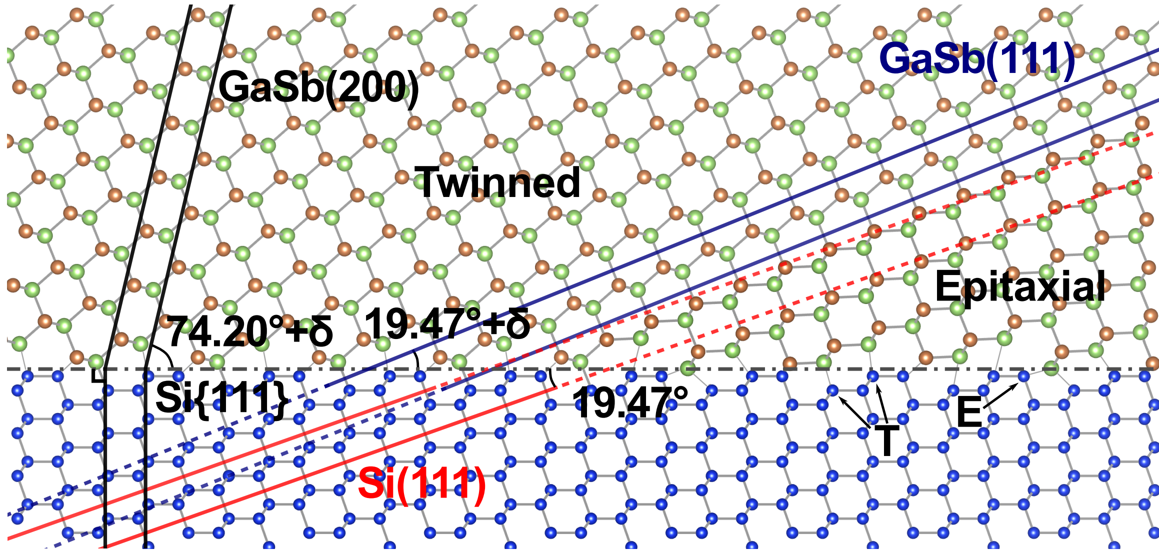

Figure 5.3: Ball-and-stick atomic model of a triple junction of the epitaxial orientation, twinned orientation (with (111) habit plane in blue), and the Si(211) surface. Geometrical alignment of the atomic planes as described by Equation (5.1) and Equation (5.2) are also shown in red/blue and black. Terrace (T) and edge (E) atom labels denote the two non-equivalent surface sites.

misfit dislocations observed at the GaSb/Si interface in the inset of Figure 5.2.

For general case of an epilayer with unknown twin volume-fraction, the tilt is bounded by competing factors of minimizing strain in both the epitaxial and twinned variants (as in GaSb on Si), with the projected strain effectively minimized at the volume-fraction weighted average of the two tilts. For GaSb with 58%, 21% and 2% twin fraction, the predicted tilts are 2.493°, 2.498° and 2.500°. This small variation in tilt angle is due to the steeper slope of Equation (5.1), thus its contribution dominates the weighted average. The intrinsic +12.2% lattice mismatch between GaSb and Si is minimized, however there are localized strain variations between the epitaxial and twinned regions. For a film with 58% twin, the projected (111) d-spacing in the epitaxial region is +0.03% (in compression), while the projected GaSb(200) and Si($\bar{1}$11) d-spacing in the twinned region is -0.12% (in tension). Thus, the proposed driving force for the tilted epilayer during growth is the minimization of lateral strain of close-packed (111) planes (red/blue planes in Figure 5.3), in one dimension within the two-dimensional projected interface net.

In addition to accounting for the tilt observed for GaSb on Si, this model predicts the tilts observed in other material systems. The growth of CdTe on Si(211) and

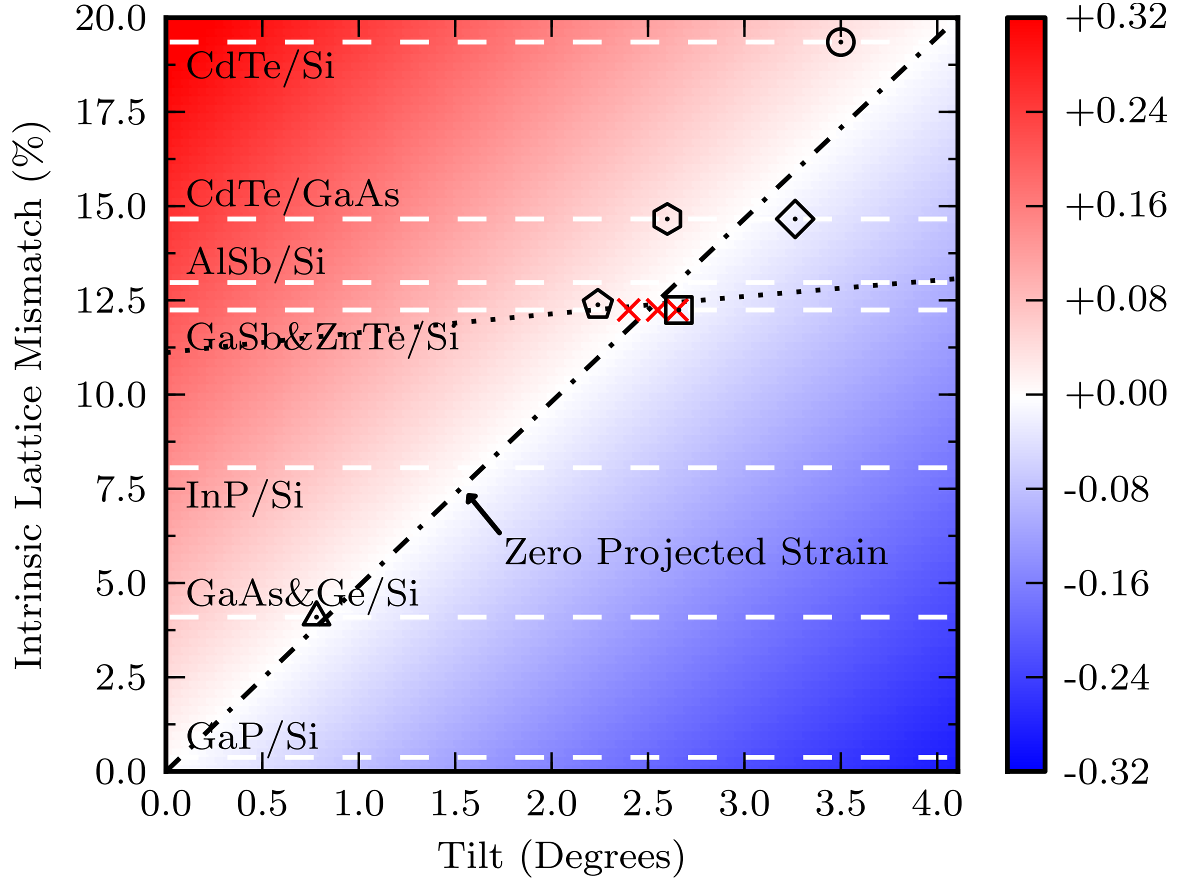

Figure 5.4: Colourmap showing the projected strain as a function of intrinsic lattice mismatch and positive tilt angle of an epitaxial film, computed from Equation (5.1) with the zero projected strain contour highlighted (dot-dash line). The dotted line also overlays Equation (5.2). Experimental data points from this work (×), Ref. Zhao, Jacobs, Jaime-Vasquez, Bubulac, and Smith [66] (⊙), Ref. Wang, Chang, Becker, Grein, Sivananthan, and Kodama [67] (⊡), Ref. Johnson, James, Ahlgren, Hamilton, Ray, and TOMPA [75] (◇, △) and Ref. Smith, Kim, McCartney, and Aoki [83], Kim, Smith, Jacobs, Almeida, Jamie-Vasquez, Nozaki, Markunas, and Benson [84] (⬠, ⬡) are shown, indicating good agreement with measured tilts of thin films. Common heteroepitaxial systems are also highlighted. Close lattice mismatches are merged for figure clarity.

GaAs(211) is a common use to buffer the growth of HgCdTe for detector applications. Several authors[70, 85, 86] published results which indicate CdTe epilayers which are tilted in the range of 3.5° on Si(211)[66] and 3.26° on GaAs(211)[75], about the $[01\bar{1}]$ direction towards $[\bar{1}11]$. The direction and magnitude reported by those authors agrees well with the tilt of 3.97° and 3.00°, as predicted by this model. Discrepancy between the predicted and reported value of tilt is expected to be partially due to the presence of twinning in the epilayer, along with uncertainty in the reported values.

ZnTe is often used as an intermediate buffer epilayer, prior to the growth of CdTe and HgCdTe on Si(211)[66, 68]. Wang *et al.*[67] published results which indicate epilayer tilts in the range of 2.66° while Smith *et al.*[83] reports tilts of 2.24°. This is in good agreement to the predicted value of 2.50° obtained from the proposed model. The good matching between our predicted and the reported values of tilt in ZnTe on Si(211) is expected to be due to the low degree of twinning observed.

The model also makes a prediction of the tilt expected from the growth of GaAs on Si(211), a value of 0.83° is predicted. A tilt of 0.781° is reported by Johnson *et al.*[75] when grown alone, and 0.835° when capped with CdTe, again demonstrating good agreement with the model.

For the systems AlSb/Si, InP/Si and GaP/Si, the model predicts tilt angles of 2.65°, 1.64° and 0.07°. Measurements of these material systems are expected to yield tilts that quantitatively follow this model.

5.6 Implications for Symmetry and Energy at Epitaxial Surfaces

The naturally asymmetric (211) surface of cubic non-polar semiconductors offers an alternative route to breaking the symmetry for epitaxial growth. The (211) surface offers two unique properties which can enhance nucleation and growth of lattice mismatched thin films, its asymmetric surface offers a energy landscape offering different bonding locations, and its surface has a intrinsically stepped nature.

The two non-equivalent surface sites present on an unreconstructed (211) surface offer an energy landscape which encourages the nucleation of the polar adatoms. Such a preferred nucleation of adatoms into the two non-equivalent sites results in the natural elimination of anti-phase-domains.

The surface of (211) oriented semiconductors, in addition to having non-equivalent sites, also has a naturally asymmetric surface, consisting of atomic pseudo-step features along the [110] direction. This natural asymmetric surface results in two non-equivalent directions on the surface. The broken symmetry of the surface results in an asymmetry in the grown film, allowing a preferential tilt towards to the pseudo-step direction, allowing strain reduction. Such pseudo-steps also affect defect mechanisms such as twins reducing the formation density along the step direction.

The (211) surface of semiconductors offers a range of properties which are superior for hetereoepitaxy when compared to the traditional surface orientations. Further investigation into ideal growth parameters for binary semiconductors. Vicinal variants of (211) oriented semiconductors offer an additional degree of symmetry breaking which may offer further improvement of thin film growths. Finally, higher order substrate orientations other than (211) may other types of symmetry breaking which also enhance heteroepitaxial growths.

Part III

Semiconductors on Oxide Substrates

Chapter 6

CdTe Growth on Sapphire Substrates and Liftoff Phenomenon

6.1 Introduction

The growth of CdTe on oxide substrates, specifically single crystal sapphire, has been a region of great interest for the Preston research group. Work has been published on optimization of growth parameters, the role of lattice constants, and the optical properties of the resulting thin films[87–92].

While the work investigating the growth parameters and properties of the resulting thin films has progressed to a high level, less investigation has been focused on explaining the surprising success that has been achieved with this material system. With a lattice mismatch of 3.65% between CdTe and sapphire, a difference in the crystallographic space group (cubic CdTe versus hexagonal sapphire), and chemical differences (high ionicity semiconductor CdTe versus complex oxide sapphire), the high quality single crystal nature of the grown thin films is far from expected.

In this work investigating the CdTe on sapphire heteroepitaxial material system, the unexpected high quality growth is examined through the lens of symmetry and energy at the epitaxial interface. These examinations support an explanatory model of the epitaxial alignment and defects present in CdTe thin films. These examinations also reveal the previously undocumented and highly surprising result that CdTe is not bonded nearly as strongly as expected to the sapphire substrates after epitaxial growth, resulting in the technologically relevant liftoff phenomenon. The liftoff phenomenon is examined and its resulting freestanding thin films are characterized. This liftoff phenomenon has been discovered to be robust enough to apply for a provisional patent[93] which has since been converted into a full simultaneous worldwide patent application. This work was completed in collaboration with Mr. Stephen M. Jovanovic (growths), Dr. Kristoffer Mienander (surfaces), Ms. Steffi Woo (TEM), and Dr. Martin Couillard (STEM) and relies on prior work by Dr. Robert Hughes and Dr. Svetlana Neretina (growth optimization of CdTe). Experimental design, 2DXRD, STEM analysis and engineering of liftoff was performed by myself with the assistance of Stephen M. Jovanovic.

6.2 Background

CdTe is a cubic semiconductor (a = 6.483Å) with a strong propensity to grow (111)-up, that is alternating layers of cadmium and tellurium, regardless of the structure of the

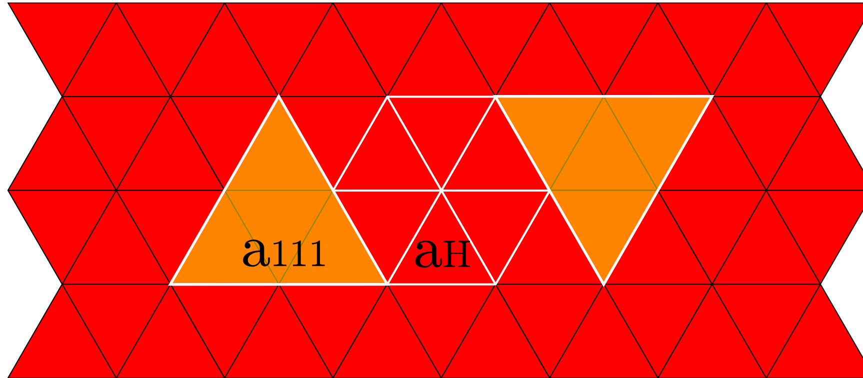

Figure 6.1: Geometric model of cubic CdTe crystal structure fit on hexagonal c-plane sapphire surface.

underlying substrate. Thus the key requirement for the growth of quality single crystal thin films is to control the nucleation and in-plane orientation. α-Al_2O_3 (sapphire) is a rhombohedral complex oxide (a = 4.758 Å, c = 12.991 Å), which presents a hexagonal surface net on its c-plane surface. As had been previously investigated by the Preston research group, the (110) diagonal of CdTe matches to double of the lattice constant of sapphire to within 3.65%, providing a geometric template for the epitaxial alignment of (111)-up on the c-plane surface. While the c-plane sapphire offers an epitaxial template for the CdTe, the mismatch of cubic on hexagonal symmetries offers two equivalent orientations for the CdTe crystal, as shown in Figure 6.1. Despite the geometric equivalence of two orientations of cubic on hexagonal symmetry, growths done by this research group have resulted in a single orientation of CdTe on the sapphire surface. Previous work by this research group attempted to explain the preferred orientation through experiments in the modification of sapphire[89], suggesting that the energy considerations at the surface play a key factor in epitaxy.

6.3 Experimental

CdTe thin films were deposited on single crystal c-plane α-Al_2O_3 $\pm 0.5°$ wafers, obtained from MTI Crystals Inc and diced into 12 mm × 12 mm squares. Prior to deposition, substrates were solvent cleaned in an ultrasonic bath. Samples were loaded into a custom pulsed laser deposition chamber at a base pressure of $1 \cdot 10^{-7}$ Torr and in-situ annealed at 450℃ for 30 minutes. CdTe thin films were deposited by pulsed laser deposition using a GSI Lumonics IPEX-848 KrF excimer laser with a wavelength of

248 nm. Pulses from the laser were focused and rastered radially onto a rotating CdTe 2.54 cm diameter target with a spot size of 4.25 mm^2 and average energy density of 1.8 J/cm^2. The CdTe 5N (99.999%) pressed powder target obtained from Princeton Scientific was stoichiometric and undoped. During growth samples were kept at a nominal temperature of 300℃ via a Pt-Rh thermocouple on the growth furnace surface. Films were grown to a thickness of 100 nm, as determined by optical and stylus profilometry.

Structural information was obtained using 2DXRD and TEM/STEM techniques. A Bruker SMART6000 CCD detector on a Bruker 3-circle D8 goniometer with Rigaku RU-200 rotating anode X-ray generator and parallel-focusing mirror optics were used for the data collection. 2DXRD data was processed into pole figures using Bruker GADDS. TEM/STEM preparation was completed by FIB preparation of cross sections followed by gentle Ar ion milling. TEM imaging was collected using a Philips CM-12 and STEM imaging was collected using a FEI Titan 80-300HB with aberration correction.

6.4 Results

CdTe thin films had been previously thoroughly structurally characterized via 2DXRD, AFM and TEM. As such, one of the next steps to fully characterize the CdTe thin films was to produce larger uniform films[28] and to electrically characterize these films via resistivity and the Hall effect. As part of this investigation, lithographic patterning of Pt contacts was performed to create van der Pauw geometry. Upon performing an acetone soak, as the photoresist dissolved, and the metal film floated off the sample, it remained in one piece, lifting off the areas of CdTe that were in contact with the metal from the epitaxial substrate. For a sample that had been previously characterized to be single crystal, this result was unexpected, as all that was required for this liftoff was an ultrasonic bath. This weak bonding phenomenon had been previously hinted at when CdTe nanowires (which are discussed in more detail in Section 8.1) were observed in SEM to have toppled in place, as shown in Figure 6.2, an event that could not have happened unless the bond strength with the interface was weak.

After the discovery of the liftoff phenomenon with lithographic patterning, simpler methods of liftoff were attempted. Strong adhesive tapes were found to successfully remove thin films with a simple mechanical peeling motion. While the tape peeling

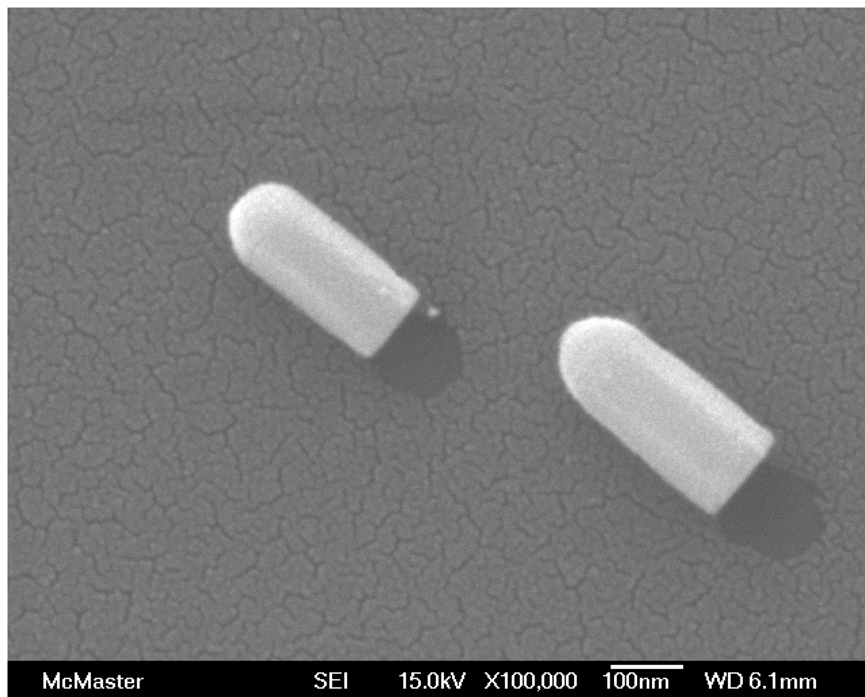

Figure 6.2: Toppled CdTe nanowire, the bare area where the substrate was not coated by gold for SEM examination is clearly visible, indicating the nanowires fell over after gold coating.

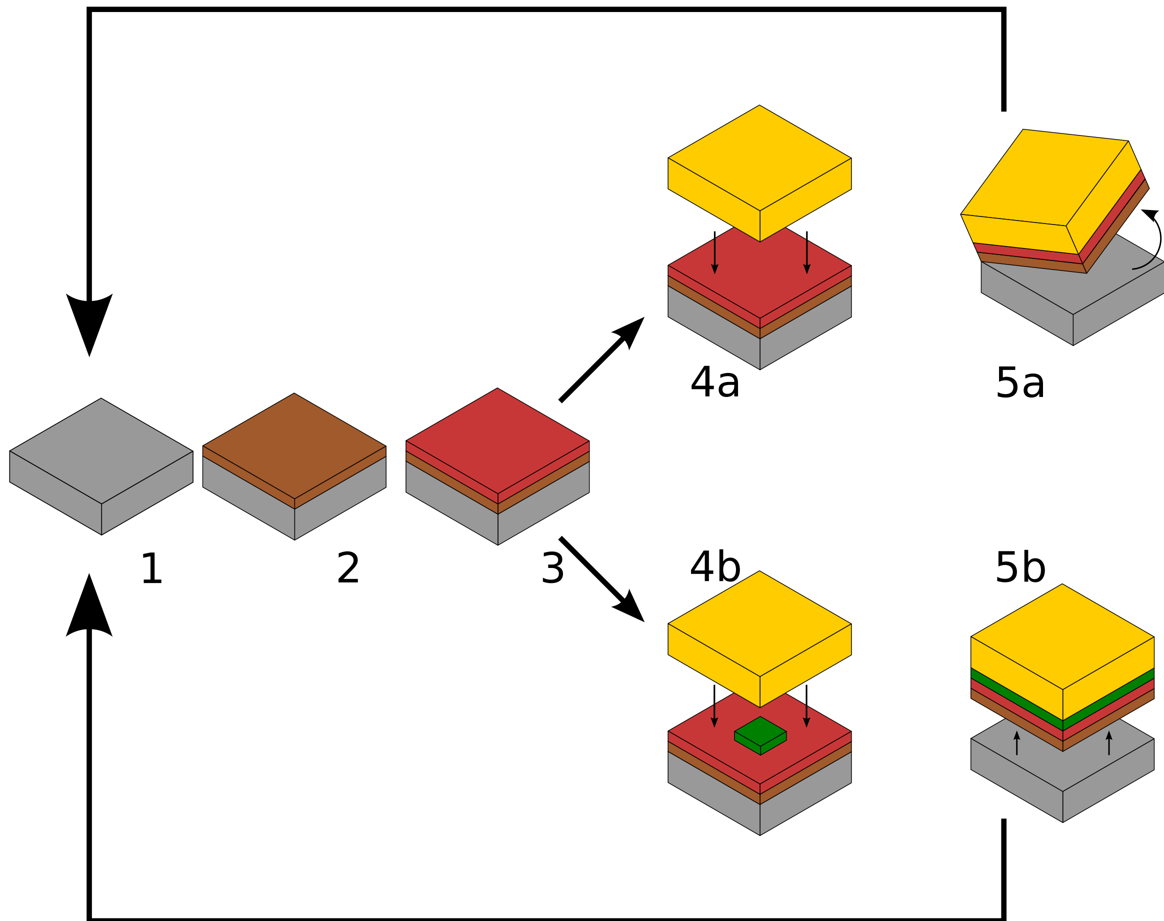

Figure 6.3: Generalized CdTe liftoff process. 1) Bare sapphire substrate 2) deposit CdTe thin film 3) deposit bonding facilitation layer (epoxy, adhesive, tape, metal layer), 4a) bond carrier substrate, 4b) wafer bond or reflow solder to metal layer and 5) liftoff CdTe thin film

was effective, the large curvatures caused cleaving and breakage in the lifted off film. Adhesive epoxies were attempted and found to provide a more rigid carrier, eliminating cleaving and breakage. Yields of liftoff are highly dependent on the quality of bonding to the CdTe surface, clean surfaces and effective adhesives are key. Numerous other bonding methods were tested including optical element adhesive, polymer films and the simplification of liftoff by the addition of liquid N_2 as thermal shock. The generalized adhesive based liftoff process is shown in Figure 6.3 The flexible non-conductive liftoff carriers offered a first step to producing freestanding thin films, but electrical contact to the films is a key property in order to yield devices. To this end, thin films were coated with metal, first platinum (a known CdTe contact material) and then copper,

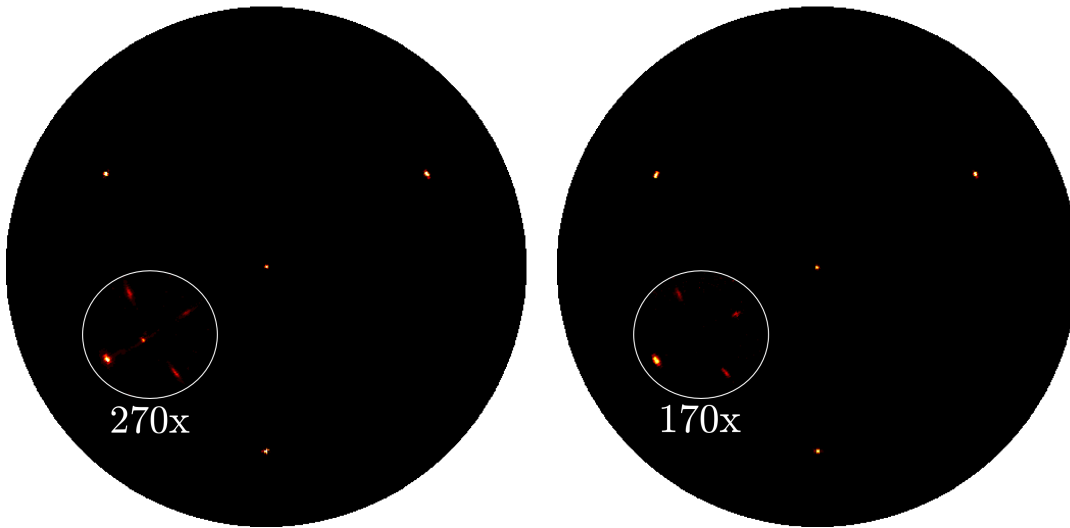

(a) (111) Pole figure of as-grown CdTe on sapphire.

(b) 2DXRD of single crystal CdTe thin film on epoxy carrier.

Figure 6.4: a) As-grown on sapphire and b) released on epoxy carrier CdTe pole figures, area of scaled intensity shows secondary phases present from twinning.

to create a reactive but temperature stable surface. Samples were then wetted with solder paste and placed metal side down onto a copper surface, and thermally cycled through a solder reflow curve, as shown in Figure 6.3 step 4b. Upon removal from the oven, the films were found to have bonded to the copper surface and spontaneously lifted off from the original sapphire substrate. These experiments have demonstrated that the production of freestanding thin films by the liftoff phenomenon is simple and straightforward.

Concurrent to investigations into the production of freestanding thin films via the liftoff process, the question arose as to the properties of these films when compared to those attached to the epitaxial substrate. 2DXRD measurements were undertaken on thin films before, Figure 6.4a and after Figure 6.4b, liftoff processing using two part epoxy. 2DXRD measurements of lifted off films, when compared to as-grown films, show a qualitatively identical pole figure. Peak broadness is unchanged, only the bleed through of the sapphire (024) peak disappears after the removal of the sapphire substrate. The change in the magnitude of the secondary twinning phase is due to the change in location of the two 2DXRD measurements on the sample.

6.4.1 Epitaxial Interface Characterization

The liftoff phenomenon observed hinges on the intimate relationship between CdTe and sapphire. In order to better understand the nature of the of this interface, experimental and computational investigations of the interface were undertaken. Samples were aligned using 2DXRD in order to prepare $(01\bar{1})$ cross-sections of CdTe using FIB for STEM imaging. Imaging was initially intended to provide atomic scale resolution of the interface, however it was found to be blurry for all samples prepared. It is unclear if this blurriness was an intrinsic property of the epitaxy process or as a result of sample preparation of the mechanically dissimilar interface.

Due to the atomic contrast available from STEM imaging, alignment of the Cd-Te dumbbells, along with absolute alignment of the physical STEM sample, allowed for determination of the polarity of the CdTe thin film. STEM imaging of the $(01\bar{1})$ cross-section of CdTe was aligned from the FIB attachment point as in Figure 6.5a. After alignment, high magnification STEM was taken at the interface as in Figure 6.5b, showing distinct $\{110\}$ family dumbbells. STEM image intensity was integrated along the dumbbells as plotted in Figure 6.6a, the modulation in the intensity data indicates a Te-Cd dumbbell oriented away from the interface. The STEM intensity modulation, combined 2DXRD crystal alignment and alignment of the STEM lamella, indicates the polarity of the thin film is CdTe(111)A, i.e. the film presents Cd-single bond up. The model of the CdTe(111)A crystal observed is shown in Figure 6.6b.

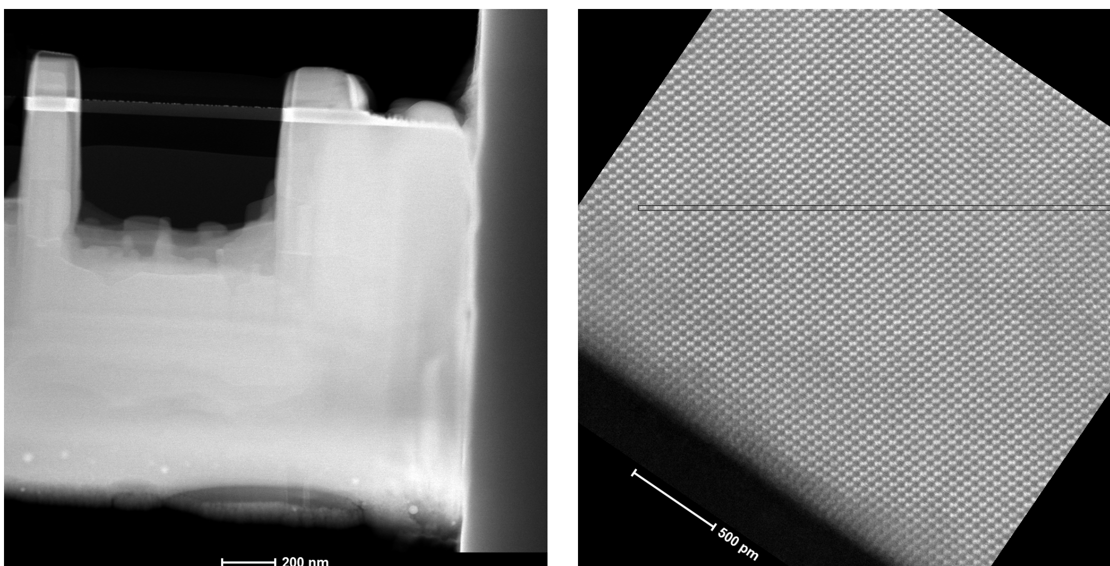

(a) Low magnification STEM of CdTe on sapphire, by FIB preparation, showing attachment point.

(b) High magnification STEM of CdTe on sapphire showing interface, CdTe dumbbells highlighted where intensity integration was performed.

Figure 6.5: CdTe on sapphire STEM images used for polarity determination.

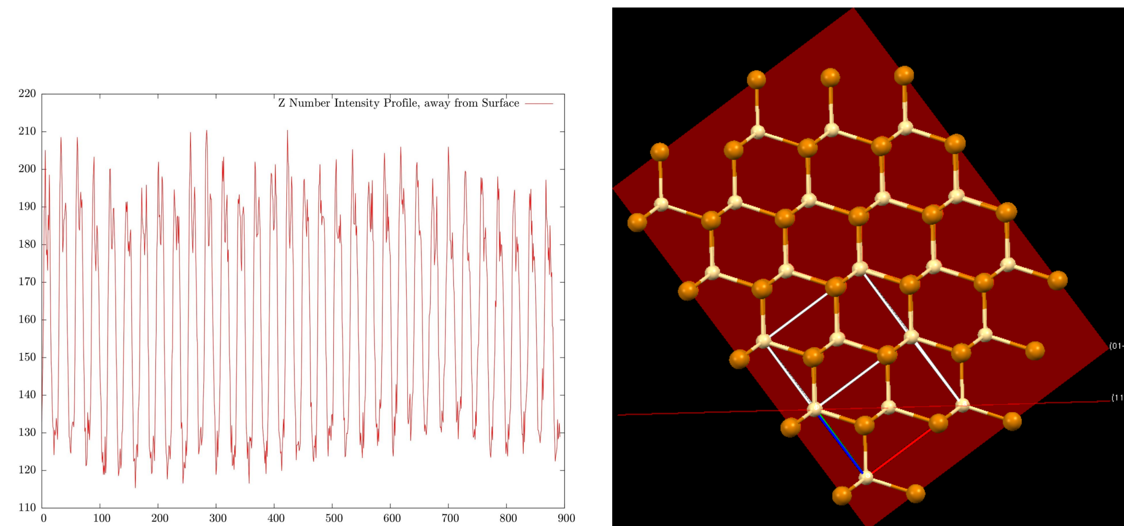

(a) Intensity plot of STEM image from Figure 6.5b, intensity is higher-lower away from surface, indicating Te-Cd dumbbells

(b) Atomic model corresponding to CdTe(111)A, Cd atoms in beige, Te atoms in orange

Figure 6.6: CdTe on sapphire STEM images used for polarity determination.

6.5 Discussion

The mechanism by which liftoff of CdTe on sapphire substrates occurs has not been definitively determined. A number of theoretical models have been examined by this group to explain the exceptional interface which yields epitaxial single crystal thin film growth and then releases the resulting film with little effort. The models proposed to explain such a process are 1) finite thickness polarization induced interface reorganization (i.e. the polarization catastrophe) 2) double layer Te nucleation, 3) van der Waals induced epitaxy and 4) weak covalent bonding.

Polar oxides (such as sapphire) are known to build up an unstable polarization due to unbalanced charge distribution (dipoles) in their unit cells, resulting in a small by finite voltage. This unstable polarization must be resolved as it builds to millions of volts over a crystal. This voltage can be resolved by reorganization of the surfaces to counteract the dipole, or via charge transfer from an overlayer. Either of these mechanisms could have a impact on the interface between the CdTe and the sapphire. Both atomic reorganization and charge transfer have the possibility of drastically altering the bonding environment leading to the liftoff phenomenon.

Investigations by this group into the liftoff phenomenon have included the use of density functional theory (DFT) modelling of the energy landscape of Cd and Te atoms on a sapphire surface, and their preferred position. Modelling of this system has indicated that there may be a preference for two layers of Te to bond to the sapphire substrate before the atoms form the typical CdTe structure. This two-layer structure immediately at the interface may be beneficial during nucleation however after some critical thickness the CdTe grown above may influence this layer such that the bonding is weakened.

Finally, it is possible for the bonding energies between the initial thin film nucleation layer and substrate to be small, with bonding being more akin to van der Waals forces (physisorption) than to the typical covalent or semi-ionic bonding seen in solids. The bonding is sufficiently strong enough to provide a good template for epitaxial growth, but when strong perturbative forces (thermal strains, mechanical peeling) are applied, the bonding can be overwhelmed. This weak bonding regime may be due to the strongly ionic nature of the CdTe semiconductor ($\sim$70% ionicity) combined with the highly stable oxide surface of sapphire.

6.6 Implications for Symmetry and Energy at Epitaxial Surfaces

The interface that lies between CdTe and sapphire has been a place of great interest for the Preston research group for many years. While sapphire can be described simply using its lattice constants and space group, such a description leaves out many complicating factors.

From a symmetry point of view, the body diagonal of CdTe fits onto sapphire with two geometric orientations. This coincident surface net, where the two crystals meet, offers the initial template for alignment of the CdTe, promoting a two-phase nucleation and growth. Such orientation relationships are key for epitaxy to occur, with fewer geometric possibilities being preferred, to reduce grain boundaries.

If growth occurred as in graphoepitaxy, where only geometry defines crystal orientation, this would still lead to defective material. From an energy point of view, the surface of sapphire can offer an energy landscape which selectively promotes one geometric orientation. For such preferences to exist, the surface must be stable and uniform, a difficult goal with the multi-layered structure of c-plane sapphire. When a uniform surface is successfully generated, the added chemical energy landscape is superimposed on the geometry, resulting in a single orientation being preferred for nucleation at the surface. The role of the surface energy landscape is a key factor in understanding epitaxy on more complicated surfaces such as complex oxides, as this work demonstrates that surface termination can have a strong effect on nucleation.

Chapter 7

CdTe Growth on Reconstructed $SrTiO_3$

7.1 Introduction

As part of the ongoing research into the growth of CdTe, other oxide single crystals were examined for possible use as substrates. One of those substrates, $SrTiO_3$, while it did not ultimately yield particularly high quality CdTe, did provide some interesting insights into the potential for surface reconstructions to play a role in epitaxy.

The role of both substrate offcut and high temperature surface reconstructions were examined through the growth of CdTe on as-received and reconstructed $SrTiO_3$ substrates. This work was published as:

S Neretina, RA Hughes, GA Devenyi, NV Sochinskii, JS Preston, and P Mascher. "Atypical grain growth for (2 1 1) CdTe films deposited on surface reconstructed (1 0 0) SrTiO3 substrates". In: *Applied Surface Science* 255.11 (2009), pp. 5674–5681. ISSN: 0169-4332. DOI: 10.1016/j.apsusc.2008.12.050 [87].

This work was done in close collaboration with Dr. Robert Hughes and Dr. Svetlana Neretina. Dr. Hughes grew the samples of interest, Dr. Neretina measured 2DXRD and AFM and I collected and produced the models of the CdTe (211) and reconstructed $SrTiO_3$ interfaces.

7.2 Experimental

CdTe films were deposited on both the as-received and reconstructed surface of (100) $SrTiO_3$ (MTI Corporation). Step-terrace formation relied upon the miscut originating from the inaccuracies in the crystallographic alignment carried out before cutting and polishing of the substrates (manufacturer's miscut tolerance 0.5°). As a result, the degree of miscut could only be varied through the selection of substrates from different manufacturer batches. Due to the high temperatures required, the surface reconstruction took place ex-situ in a quartz tube furnace. Prior to annealing, the substrates were etched in BHF for 90 s. Anneals were conducted in 60 SCCM of flowing oxygen at 1000℃ for 10 h. Figure 7.1 shows atomic force microscopy (AFM) images for the as-received and surface reconstructed substrates relevant to this work. As expected, only the annealed substrates exhibit the step-terrace structure with unit cell step heights. The difference in terrace width for the surfaces shown in Figure 7.1b and c can be attributed to a miscut difference estimated at 0.358°. Also present on each image are the crystallographic axes obtained through X-ray diffraction (XRD). A

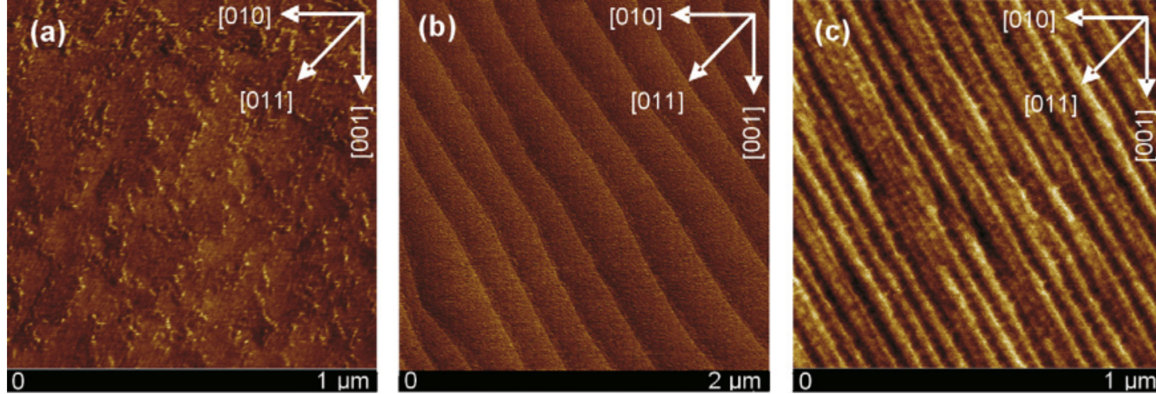

Figure 7.1: AFM images for the (a) as-received (100) $SrTiO_3$ substrate, (b) a reconstructed surface with an average terrace width of approximately 200 nm and (c) a reconstructed surface with a terrace width of approximately 50 nm. From the step heights and terrace widths it is estimated that the miscuts for the two reconstructed surfaces are (b) 0.118° and (c) 0.468°.

nearly identical in-plane step direction exists for both reconstructed surfaces. As this direction is close to, but not aligned with the [011] axis of $SrTiO_3$, it is expected that the steps exhibit a sawtooth morphology, but on length scales not readily observed using atomic force microscopy.

CdTe films were deposited on the three $SrTiO_3$ surfaces shown in Figure 7.1 using pulsed laser deposition. A deposition rate of 20 nm/min was achieved by operating the laser at a repetition rate of 10 Hz with a substrate to target distance of 3.5 cm. Films were grown to a thickness of 300 nm as determined using a spectroscopic variable angle ellipsometer (Horiba Jobin Yvon, France). Morphological and structural characterization was then conducted on the films using AFM and 2DXRD.

7.3 Results and Discussion

Figure 7.2 shows the (111) CdTe pole figures for the three substrates shown in Figure 7.1. The dramatic differences observed between films deposited on the as-received and annealed substrates indicate that the surface reconstruction gives rise to a complete re-alignment of the CdTe grains. The pole figure for the as-received surface is consistent with a [111] oriented film. Twelve peaks are present in the outer ring, instead of the three expected for a single crystal, indicates that there are four in-plane grain orientations. The pole figures for the films deposited on the surface

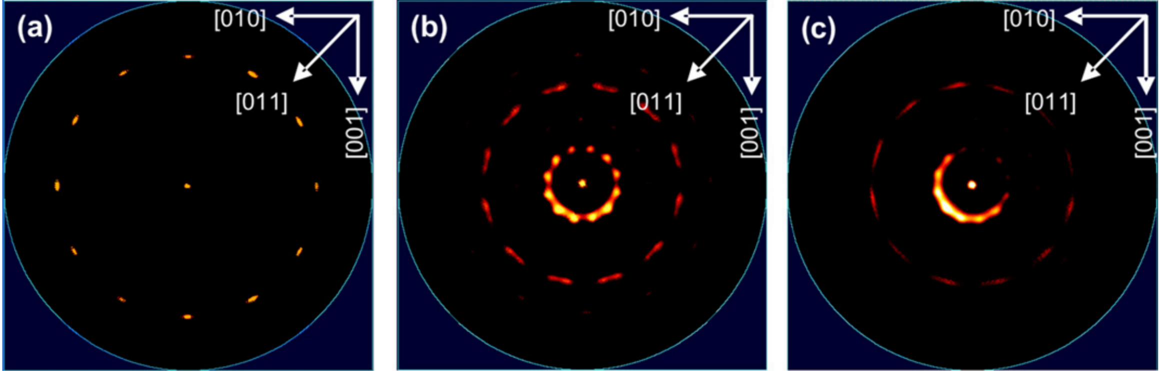

Figure 7.2: (111) CdTe pole figures for films deposited on (a) the as-received (100) $SrTiO_3$ substrate (b) the reconstructed surface with wide terraces and (c) the reconstructed surface with narrow terraces. Indicated on each image are the substrate's in-plane crystallographic axes obtained from XRD measurements.

reconstructed substrates show that both films are predominantly [211] oriented. The twelve peaks in the central ring and 24 peaks in the outer ring denote twelve in-plane grain orientations. Each peak in the central ring comes from a different grain, the intensity differences indicate that some grains form preferentially over others. Of the twelve peaks both the strongest and weakest is in-line with the miscut direction for both of the reconstructed surfaces and that the degree of this preferential orientation is stronger for the reconstructed surface having the narrow terrace width. An examination of the low intensity pole figure peaks (not visible in the figures), indicates that some [111] CdTe grains exist in these nominally [211] films, but at the 10% level. While these [111] grains contribute to the intensity at the centre of the pole, the response there is due to the (100) $SrTiO_3$ substrate. The simulated pole figures for single crystal [111] and [211] CdTe and [001] $SrTiO_3$ are shown in Figure 7.3.

Grain formation for a given film/substrate combination is determined by the interface energy. For the case of the as-received (100) $SrTiO_3$ substrate the interface energy is minimized through the formation of [111] CdTe grains. This interfacial relationship is not surprising as CdTe has demonstrated a high propensity for forming it regardless of the substrate surface offered[91]. The resulting interface, however, must overcome the seemingly incompatible situation brought about when the four-fold symmetric substrate surface mates with the six-fold symmetric (111) plane of CdTe. In this scenario it is reasonable to expect that the resulting in-plane grain structure reflects both a suitable fit to the substrate's atomic arrangement as well as its underlying

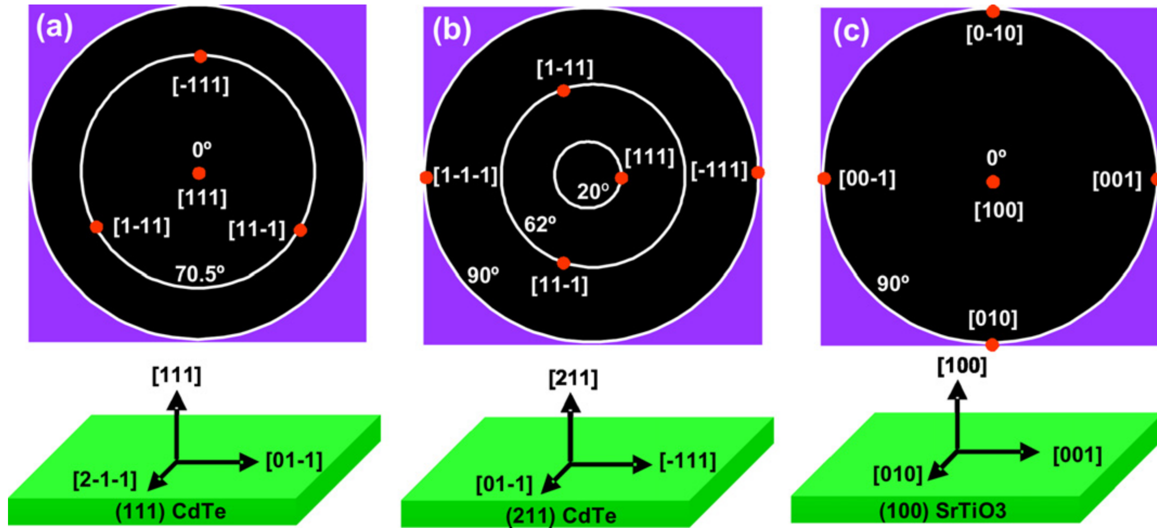

Figure 7.3: Schematics showing the (111) pole figure expected for a single crystal CdTe film with a) [111] and b) [211] orientation. c) Schematic showing the (100) pole figure expected for a [100] oriented $SrTiO_3$ substrate. The surface normal and in-plane Miller indicies are also shown for each case.

symmetry. The (111) pole figure results indicate that this is indeed the case as there is a four-fold symmetric grain structure which is commensurate with the substrate's cubic crystal structure. The XRD data indicates that these grains are oriented as shown schematically in Figure 7.4a. The triangles symbolize the orientation of the (111) planes on the surface of $SrTiO_3$ represented by the dotted pattern. The arrows on the triangles denote the three equivalent (111) CdTe planes that project out of its surface. Each of these four triangles match poorly to the substrate's lattice constant in all but one direction. In this direction, it is nearly equal to two of the substrate's unit cells (mismatch = 1.6%). This one-dimensional match is preferred to such extents that only grains that comply with it exist within the film. To appreciate the uniqueness of the four grains, for the arrows denoting the (111) equivalent planes, no two arrows point in the same direction. It is these directions that give rise to the twelve peaks in the outer ring of the (111) pole figure as is evident from Figure 7.4b.

The formation of a [211] CdTe film on a surface reconstructed (100) $SrTiO_3$ substrate was unexpected. CdTe films with this orientation have been deposited, but only when the interface energy is minimized through the use of [211] oriented substrates [94–97]. While [211] substrates provide an appropriate template for [211] growth, there exist no obvious symmetry arguments that would allow for twelve symmetrically

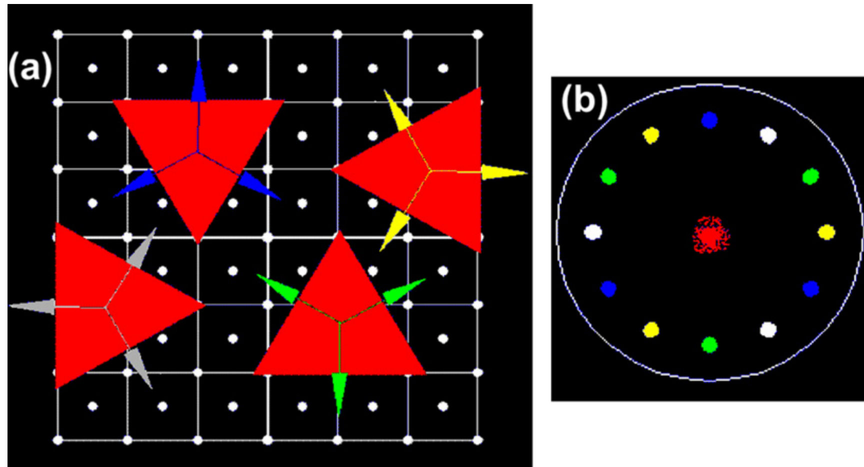

Figure 7.4: a) Schematic illustrating the four possible [111] CdTe grain orientations (triangles) for films deposited on the $SrTiO_3$ substrate (dotted background). The arrows on each triangle denote the direction of the three equivalent (111) planes that emerge from the surface. For each grain orientation there is a one-dimensional geometrical fit (mismatch = 1.6%) to the substrate in either the vertical or horizontal directions. b) Schematic showing the resulting (111) pole figure obtained from the four grains where the colour of the dot on the pole figure corresponds to the grain from which it was derived.

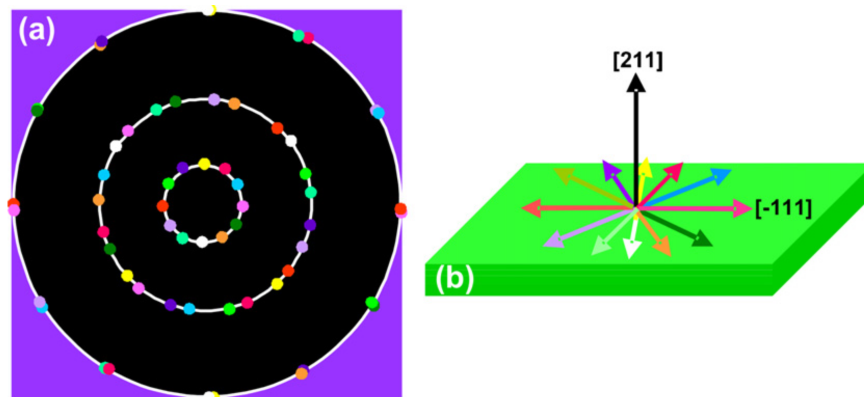

Figure 7.5: a) Schematic detailing the twelve-fold symmetric [211] CdTe grain structure observed for films deposited on the surface reconstructed substrates. The contribution from each grain is denoted by a different colour. The pattern corresponding to a single crystal [211] CdTe film (Figure 7.3b) is repeated twelve times. b) Schematic showing the in-plane $[\bar{1}11]$ direction for each of the [211] grains.

distributed grains to be accommodated on the bulk surface of (100) $SrTiO_3$. Instead, it is expected that the origin of the [211] CdTe grains lies with the epitaxial relationship formed between the (211) planes and the surface reconstruction. In this case, it is expected that the twelve-fold symmetric grain structure is commensurate with the underlying symmetry of the substrate's surface reconstruction. Thus, insight into the nature of the reconstruction is obtained from the observed grain structure. Figure 7.5 shows a schematic representation of the (111) CdTe pole figure where the contributions from each grain are shown. The pole figure's inner ring demonstrates a twelve-fold symmetry in the grain structure as it is composed of twelve nearly equally spaced peaks where each peak originates from a different grain orientation. The wide terrace widths shown in Figure 7.1b give rise to [211] CdTe grains even though the film grain size is often smaller than the width of the terrace. Thus, it appears that [211] grain formation does not rely on nucleation at the substrate steps. The insensitivity to step edges indicates that the atomic scale surface reconstruction is the dominant factor in the promotion of the [211] grains.

Of the three surface reconstructions known to form in an oxygen ambient, only the $c(4 \times 2)$ and $c(6 \times 2)$ reconstructions present a surface structure where there exist reasonable symmetry arguments able to account for the formation of a [211] CdTe film having a twelve-fold symmetric grain structure. Such a grain structure must arise from the symmetries of the underlying substrate as it provides the only means for the isolated grains to establish a symmetrical arrangement when first formed in an island growth mode. The (211) plane of CdTe, shown in Figure 7.6, is lack of symmetric and consists of a series of rows comprised of alternating cadmium and tellurium atoms separated by distances of 8.49 or 2.83 Å. Figure 7.7 shows a schematic of the $c(4 \times 2)$ TiO_2 surface reconstruction proposed by Castell[98]. It consists of a series of alternating rows of titanium and oxygen atoms. The top layer has a TiO_2 stoichiometry, but it is sparsely populated with only one quarter the number of atoms present in the TiO_2 layers found in the bulk[98]. With every second row of titanium atoms offset relative to each other they align in a pseudo-six-fold symmetric pattern. Possible geometric fits of the (211) CdTe plane to this surface reconstruction are shown in Figure 7.7b. Each of the three possible geometric fits shown would give rise to two unique grain types due to the one-fold symmetry of the (211) plane. Six other domain structures would also form by virtue of the fact that the $c(4 \times 2)$ surface reconstruction has two possible domains rotated 90° relative to each other[98]. The

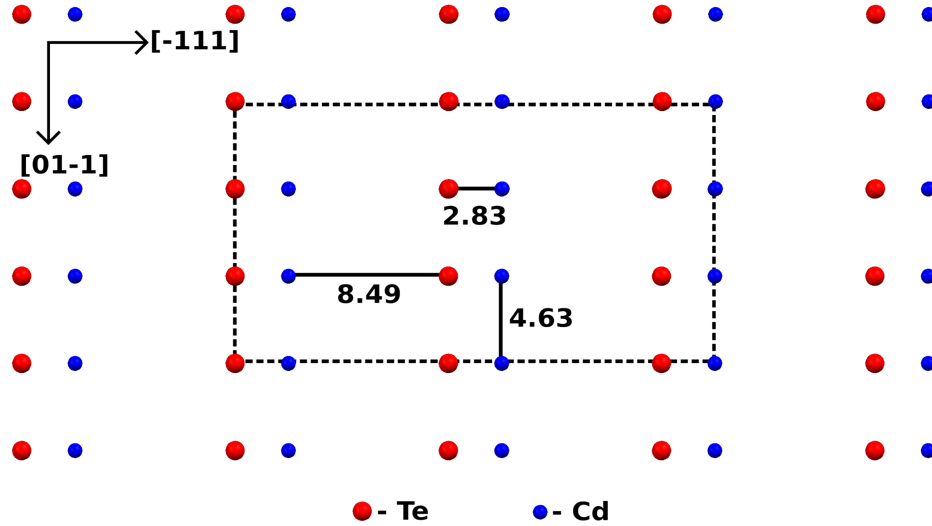

Figure 7.6: Schematic of the (211) plane of CdTe with the interplanar dimensions labelled in units of angstroms. The area outlined by the dashed lines is used in subsequent figures to demonstrate how this structure fits to (100) $SrTiO_3$ surface reconstructions. The Miller indices shown correspond to the crystallographic orientation of the (211) CdTe plane.

domain structure that develops on the reconstructed surface arises from the fact that the rows of titanium atoms have an equal probability of forming along the [010] or [001] directions. The net result would be a twelve-fold symmetric [211] CdTe grain structure. The c(6×2) surface reconstruction, proposed by Jiang and Zegenhagen[99], is shown schematically in Figure 7.6. It too is a sparsely populated surface that has the potential to accommodate the (211) CdTe planes in select directions (Figure 7.6b). Here, the four geometrical fits shown give rise to eight unique grain types. In a manner analogous to the c(4×2) reconstruction, the c(6×2) reconstruction also has a domain structure that gives rise to an additional set of eight grains rotated 90° to the ones shown in the figure. An examination of these additional grains, however, reveals that only four of them provide unique solutions as the other four rotate into solutions offered by the first domain. Thus, a twelve-fold $(8 + 8 \times 4 = 12)$ symmetric (211) CdTe grain structure is expected for this surface.

Assuming that the orientation relationships between CdTe and the surface reconstructions shown in Figures 7.7 and 7.8 are adhered to then it becomes possible to experimentally predict the surface reconstruction undergone by the substrates presented in this work. It should be noted from Figure 7.7b that the c(4×2) reconstruction is characterized by (211) CdTe grain alignment along the substrate's [010] and [001]

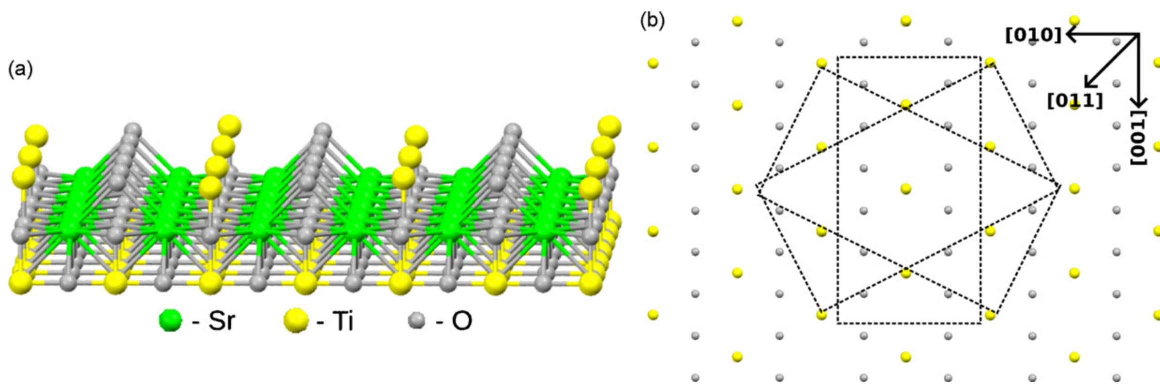

Figure 7.7: (a) Schematic showing the surface of the (100) $SrTiO_3$ with a c(4×2) surface reconstruction. (b) Schematic showing the uppermost layer of the reconstruction with the dashed lines being used to illustrate the closest geometrical fits of the (211) CdTe plane to this surface. The three orientations shown give rise to six grain orientations as a 180° rotation of the (211) plane yields a different grain structure. This is a consequence of the fact that the single crystal (111) CdTe pole figure for a [211] film is one-fold symmetric (see Figure 7.3b). Six other grain structures arise from a domain structure in the substrate surface reconstruction that would be schematically represented by a 90° rotation of Figure 7.7b. The Miller indices shown in the top right corner of the figure correspond to the crystallographic orientation of the underlying bulk (100) $SrTiO_3$ substrate.

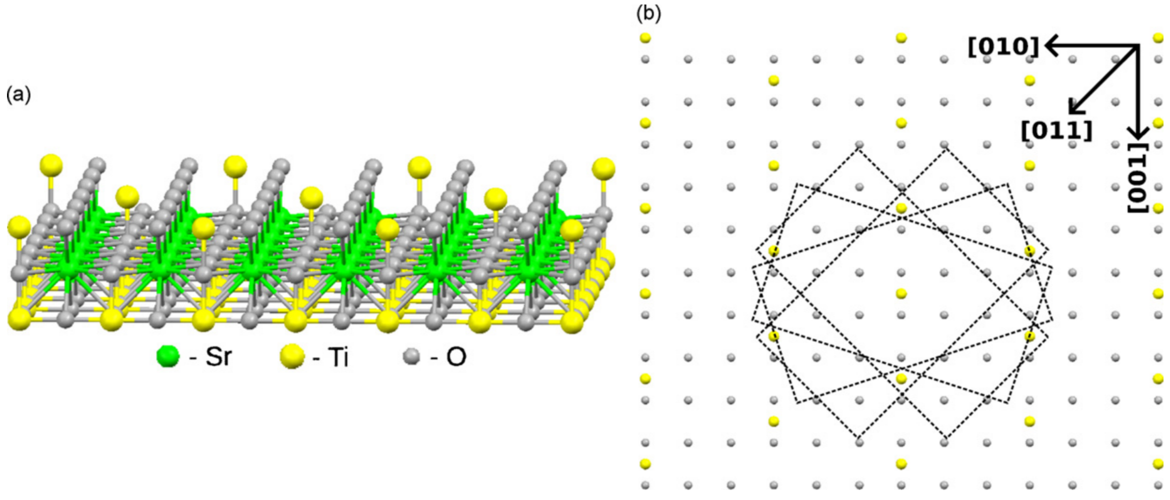

Figure 7.8: (a) Schematic showing the surface of the (100) $SrTiO_3$ with a c(6×2) surface reconstruction. (b) Schematic showing the uppermost layer of the reconstruction with the dashed lines being used to illustrate the closest geometrical fits of the (211) CdTe plane to this surface. The four orientations shown give rise to eight grain orientations as a 180° rotation of the (211) plane yields a different grain structure. Eight other grain structures arise from a domain structure in the substrate surface reconstruction that would be schematically represented by a 90° rotation of Figure 7.7b. Of these eight grains only four represent unique solutions as the grains forming along the [011] and [01$\bar{1}$] directions rotate into each other. The Miller indices shown in the top right corner of the figure correspond to the crystallographic orientation of the underlying bulk (100) $SrTiO_3$ substrate.

directions. Figure 7.2b shows that this is not the case, ruling out this reconstruction for the work presented here. It does not, however, rule out the possibility of [211] CdTe grain growth if a film were deposited on such a reconstruction. The c(6×2) reconstruction, on the other hand, requires grain growth along the substrate's [011] and [0$\bar{1}$1] directions, consistent with the X-ray data. While we have no direct evidence that the c(6×2) surface reconstruction formed, the anneal conditions used elsewhere[99] to obtain this reconstruction are similar to those used here. While it should be understood that predicting a film-substrate orientation relationship solely on the basis of a geometrical fit is somewhat naïve, it is well established that this scenario occurs in the substantial balance of cases.

Even though both the [211] oriented films show pole figure peaks in similar positions, the relative intensities of the peaks are different. This is most easily seen by examining the innermost ring of the pole figure where each of the twelve peaks corresponds to

a unique grain orientation. For both samples the peaks on one side of the ring show greater intensities than on the other. This effect, however, is much more pronounced for the pole figure shown in Figure 7.2c. Here, the ratio of the integrated intensities between the largest and smallest peak in the ring is 22 compared to 4 for the pole figure shown in Figure 7.2b. The fact that the terrace width is approximately four times smaller for the film that shows the most pole figure anisotropy suggests that the step edges promote this preferential grain alignment. Consistent with this explanation is the fact that the highest intensity peaks correspond to the CdTe grain orientation having its [111] in-plane direction normal to the step. The larger grain sizes exhibited by the surface with smaller terraces are also expected within this scenario. This is a simple consequence of the fact that, in the early stages of film growth, there are more similarly oriented grains that are able to merge into a single larger grain as is expected for an island growth mechanism. With a sizeable effect being observed between the two reconstructed surfaces having a miscut difference of only 0.358°, the potential exists to amplify this effect using a substrate with a larger miscut.

The results presented here show that the reconstructed surface of (100) $SrTiO_3$ profoundly alters the grain structure of CdTe films. While it is not unusual for the grain structure to be transformed by the presence of a step-terrace morphology, it is unprecedented for $SrTiO_3$'s atomic-scale reconstructions to promote a film with an alternative heteroepitaxial relationship. For the case of (100) $SrTiO_3$, there seems to be a disconnect between the research advocating a step-flow growth mode and the wide array of atomic-scale surface reconstructions allowed, with the latter not considered as a determining factor in the film quality achieved. This may be due to the high growth temperatures used in the fabrication of oxide thin films. In this case, the thermal energy available likely facilitates a local rearrangement of surface atoms in response to the addition of adatoms. This is the case for the homoepitaxial growth of silicon where the surface reconstruction gives way to bulk crystalline ordering for temperatures in excess of 300℃[100]. For the low growth temperatures used in the fabrication of these CdTe films the surface reconstruction is likely locked in place, forcing CdTe to accommodate itself on the reconstructed surface. The sparsely populated nature of such a surface should make it prone to alternative epitaxial relationships as the interface would not consist of an abrupt boundary, but instead, of an amalgamation of two interpenetrating layers. Consistent with this explanation is the fact that different (100) $SrTiO_3$ surface reconstructions give rise to palladium nanodots having variable

orientations and faceting[101].

7.4 Implications for Symmetry and Energy at Epitaxial Surfaces

While the results presented here do not explicitly improve the growth of the CdTe thin films, they do add to the understanding of the role of the interface in epitaxy. In all the cases presented here, the substrate used for epitaxial growth has a nominal orientation of (100), with small miscut of less than 1°. Despite a fixed orientation for the substrate, the thin surface net presented to the epitaxial thin film dominates the nucleation and growth orientation. These results show that it is possible to leverage high temperature surface reconstructions in order to completely transform a given substrate for later growth at lower temperatures. If a reconstruction can be created at high temperature and then locked-in at the growth temperature, substrates that do not immediately appear to be an epitaxial match can end up presenting an ideal template for growth. The additional symmetry breaking that is available for offcut substrates can widen the range of acceptable substrates, by triggering a step-flow growth mode suppressing unwanted orientations.

For this type of surface net epitaxy to yield the most benefit, surface science research must investigate the zoo of surface reconstructions possible on the commercially available complex oxides. The higher element complex oxides (YAG, YSZ, GGG etc.) have little to no literature examining their surface reconstructions or their behaviour when miscut. Phase diagrams of such surfaces would be highly beneficial in predicting good matches for epitaxy.

Chapter 8

CdTe Nanowire Growth on Sapphire

8.1 Introduction

A topic of substantial interest in semiconductor physics in recent years has been the potential of confined dimensional materials such as nanowires, particularly through the vapour-liquid-solid (VLS) growth process. As the research group had been successful at producing thin films of CdTe, experiments were attempted in the production of CdTe nanowires using a number of metal catalysts.

CdTe VLS nanowires were successfully grown using the PLD process and several insights were gained into the role of energetics at the epitaxial growth surface, and how they can affect nanowires during growth. This work was published as:
S. Neretina, R A Hughes, G A Devenyi, N V Sochinskii, J S Preston, and P Mascher. "The role of substrate surface alteration in the fabrication of vertically aligned CdTe nanowires". In: *Nanotechnology* 19.18 (2008-05), p. 185601. ISSN: 0957-4484. DOI: 10.1088/0957-4484/19/18/185601 [88].
This work was done in close collaboration with Dr. Robert Hughes and Dr. Svetlana Neretina. Dr. Hughes grew the samples of interest, Dr. Neretina performed the SEM imaging and 2DXRD measurements and I performed the statistical analysis of the nanowire SEM images and numerically modelled the growth process.

8.2 Experimental

The experimental results and procedures presented here will focus on those nanowires derived from Bi_2Te_3 catalytic seeds deposited on pristine (0001) sapphire substrates. The results obtained will then be compared to the CdTe nanowires, described elsewhere[102], obtained using bismuth catalytic seeds deposited on polyvinyl alcohol or terpineol treated (0001) sapphire substrates.

The Bi_2Te_3 seeds were prepared using the PLD process (GSI Lumonics IPEX-848 excimer laser at 248 nm, laser energy density 2 J cm^{-2}, laser spot size 1.2×1.2 mm^2). The target used was prepared in-house from commercially available Bi_2Te_3 pieces (99.999% purity). These pieces were melted in a cylindrical graphite mould that was machined to sizes able to yield a 1 inch target weighing approximately 10 g. This procedure was carried out in an argon background gas. Before the deposition, the sapphire substrate was heated to 400℃ and held there for 10 min in an oxygen background pressure of 300 mTorr.The substrate was then cooled to room temperature

where a 20 Å thick film of Bi_2Te_3 was deposited. This deposition lasted 35 s at a laser repetition rate of 3 Hz. Once deposited, the film was then heated to 370°C where, over the course of 10 min, it would dewet forming Bi_2Te_3 seeds. At this point, a 30 sccm helium flow was introduced into the chamber such that the pressure was maintained at 400 mTorr. Material from a rotating CdTe target, grown using the Bridgman method, was then deposited onto the substrate for time intervals typically in the range of 30–45 min at a laser repetition rate of 8 Hz. The nanowires were then allowed to cool to room temperature in the helium ambient.

8.3 Results and Discussion

Figure 8.1a shows an SEM image, of the Bi_2Te_3 catalytic seeds formed on the (0001) sapphire substrate. The seeds show a substantial size distribution with diameters as large as 150 nm. While these seeds show enhanced stability, they are still prone to evaporation and will disappear completely if the CdTe deposition is delayed by approximately 10 min. As was the case for the bismuth catalysts, the Bi_2Te_3 seeds gain stability from exposure to the cadmium/tellurium flux. It is also likely that the seeds shown in the image are somewhat different from those available when nanowire growth commences as the time required to cool these seeds to room temperature provided ample opportunity for further evaporation and Ostwald ripening.

Figure 8.1b shows an SEM image of the CdTe nanowires derived from Bi_2Te_3 seeds. In many respects, these nanowires are indistinguishable from those grown using bismuth seeds in conjunction with an alcohol-altered surface[102]. The two methods both yield vertically aligned nanowires that are highly faceted, share an epitaxial relationship with the substrate and grow without a two-dimensional planar layer. The nanowires are identical from a structural standpoint as well, exhibiting the wurtzite crystal structure instead of the bulk zincblende phase. Figure 8.2 shows a pole figure that includes contributions from both the (111) zincblende and (0002) wurtzite planes. Both phases give rise to a peak in the centre of the pole, but a zincblende phase must also give rise to a ring of three peaks at the outer extent of the pole. For the pole figure shown no such peaks are observed, but in general a small zincblende signature was visible. The three small peaks that do appear in the pole figure are associated with the sapphire substrate.

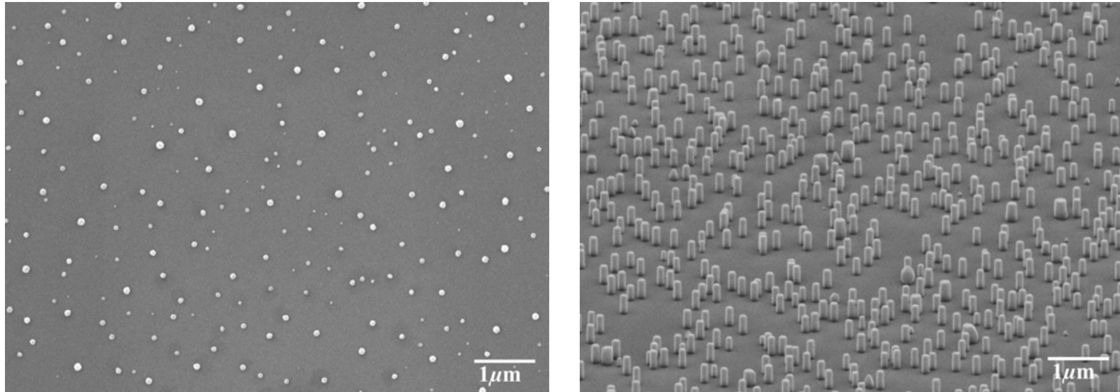

(a) SEM image of the Bi_2Te_3 seeds that were used as catalysts for CdTe nanowires.

(b) SEM image of CdTe nanowires derived from Bi_2Te_3 catalytic seeds presented from a 70° tilt side view.

Figure 8.1: SEMs of seeds and resulting wires.

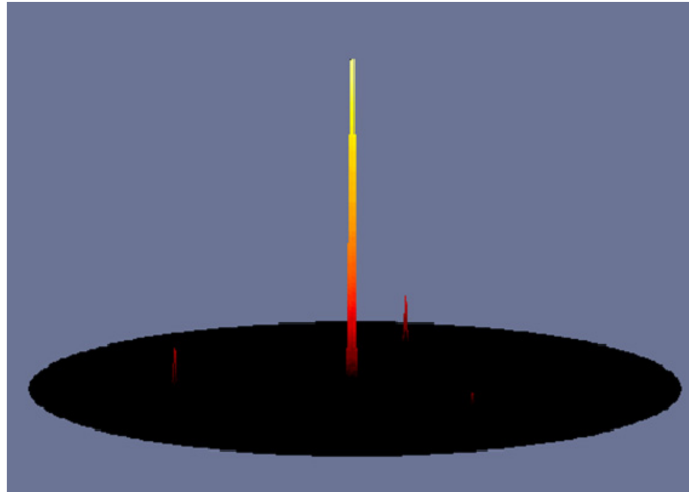

Figure 8.2: CdTe pole figure results for 2θvalues that include contributions from both the (111) zincblende and (0002) wurtzite phases. The pole figure shows no evidence of a zincblende phase. The three small peaks originate from the (0001) sapphire substrate.

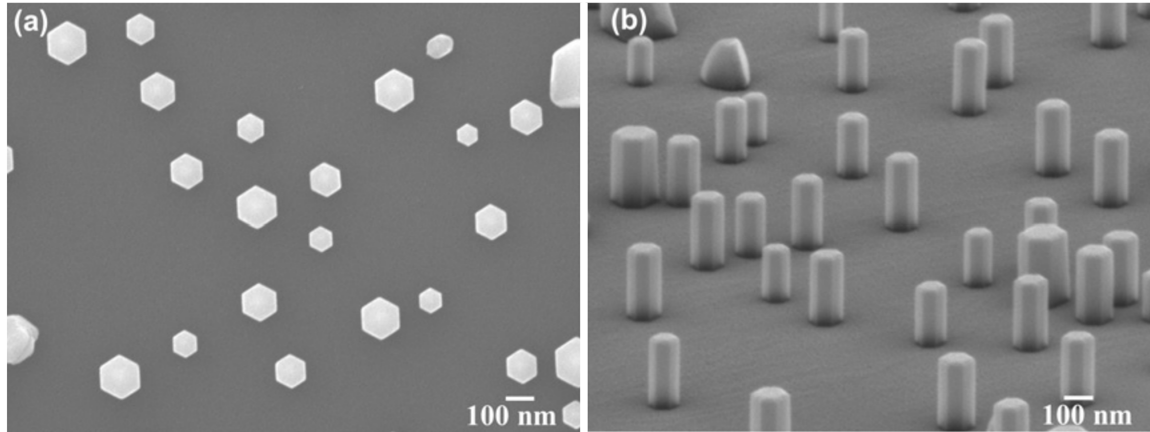

Figure 8.3: SEM images of CdTe nanowires from a (a) top and (b) side view (70° tilt). Highly faceted wires exhibit a substantial variation in both heights and diameters.

Even though these Bi_2Te_3 catalysed nanowires share many similarities with those derived from the bismuth seeds deposited on an alcohol-altered surface, there do exist substantial differences. One of the most striking differences is the nanowire size distribution observed in the SEM images of Figure 8.3. This size distribution is quantified by the colour map presented in Figure 8.4a. It shows a nanowire height versus diameter distribution for the Bi_2Te_3 seeded nanowires. It is quite clear from the map that larger diameter nanowires exhibit higher axial growth rates than those with smaller diameters. Figure 8.4b shows the same distribution for nanowires derived from bismuth seeds deposited on an alcohol-altered surface. A comparison of the two colour maps shows that the alcohol-altered surface gives rise to a narrower size distribution. It is also apparent from the distributions that the Bi_2Te_3 seeded nanowires are of larger diameter with values typically in the range of 80–200 nm. Also different is the fact that the Bi_2Te_3 nanowire height is not limited to 300 nm. Instead the nanowires grow longer while exhibiting substantial growth in the lateral direction (Figure 8.5). Moving away from the optimum growth conditions gives rise to other differences between the two nanowire growth procedures. First, nanowires formed at the substrate's edge have slanted tops where the direction of the slant at the left and right edges of the substrate point in opposite directions (Figure 8.6). Also of note is the fact that the nanowire's cross-section is no longer hexagonal, but instead elongates along the direction of the slant. Second, at high growth rates Bi_2Te_3 seeded nanowires show distinct tapering (Figure 8.7). This work combined with our previous results has demonstrated that CdTe nanowire structures can originate from catalytic seeds derived from two separate

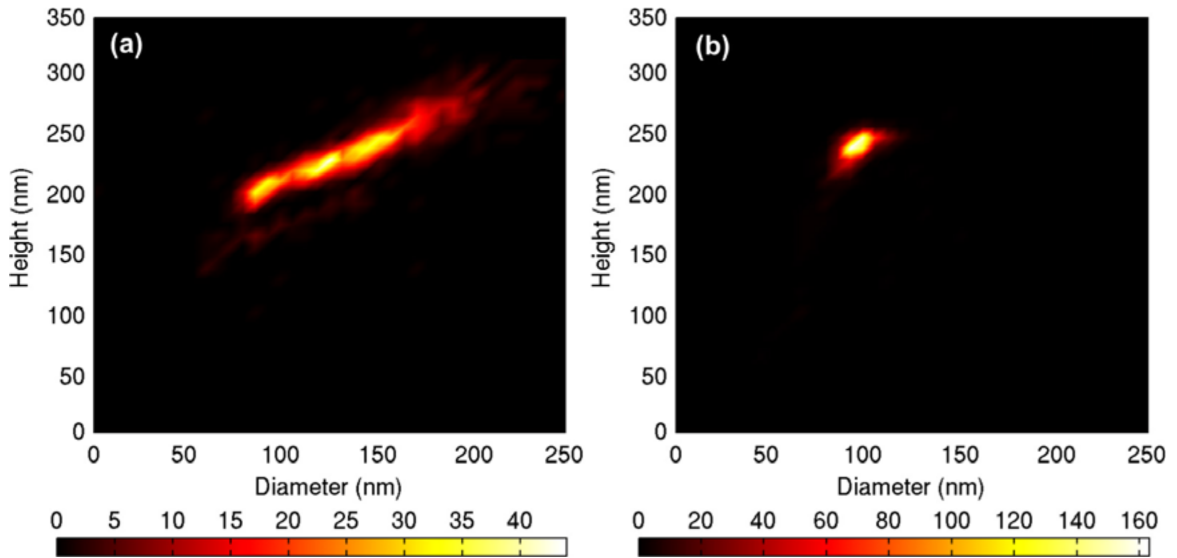

Figure 8.4: Colour map showing the nanowire height versus diameter size distribution for nanowires derived from (a) Bi_2Te_3 catalytic seeds and (b) bismuth seeds deposited on an alcohol-altered surface. The maps were generated from the measured dimensions of (a) 1344 and (b) 966 nanowires. The colour bar below each figure denotes the number of times a nanowire of a given dimension is observed. The Bi_2Te_3 seeded nanowires exhibit a broader size distribution and sizes that are, in general, larger than the bismuth seeded wires.

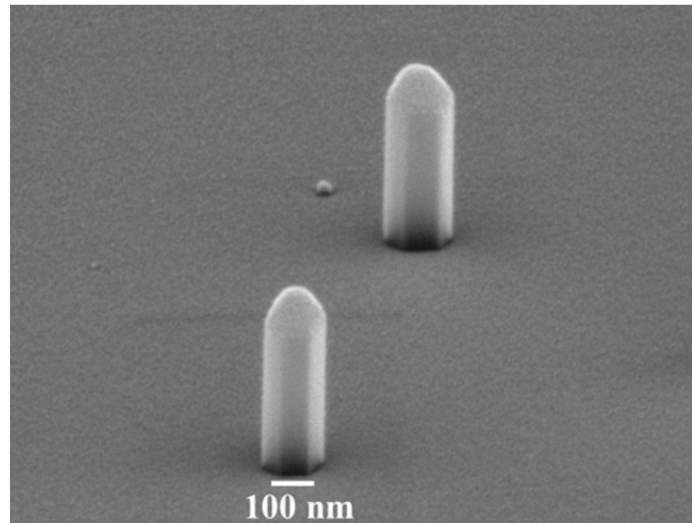

Figure 8.5: SEM images of CdTe nanowires deposited using extended growth times where increases to the height are met with substantial lateral growth.

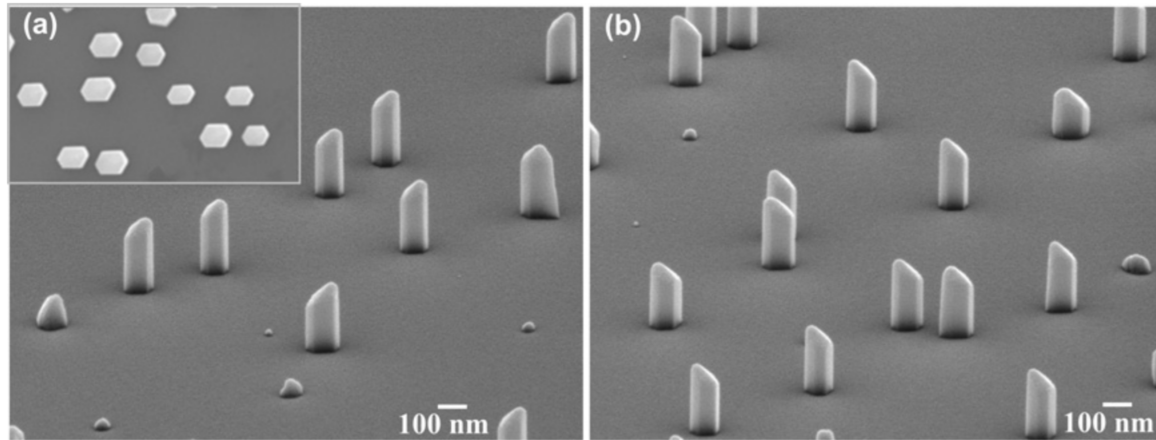

Figure 8.6: SEM images of CdTe nanowires with slanted tops that have formed at the (a) left and (b) right edge of the substrate. The tilt is in opposite directions. The top views of these nanostructures, shown in the inset to (a), indicate that the hexagonal cross-sections are elongated in the horizontal direction.

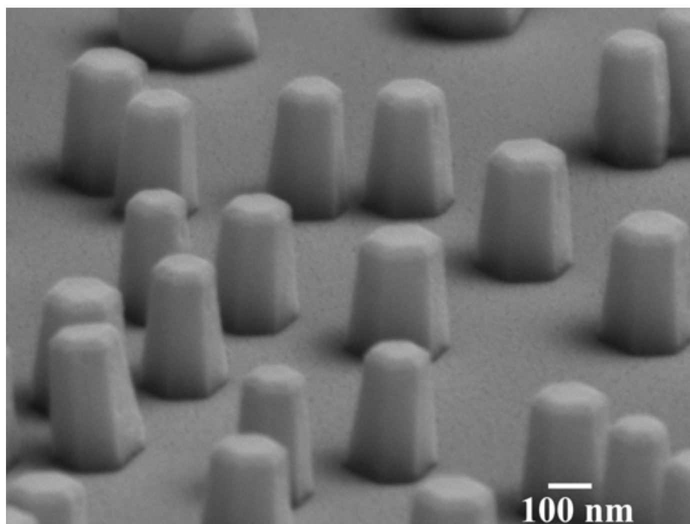

Figure 8.7: SEM image showing tapered CdTe nanowires.

processes, with each of these processes having advantages and disadvantages. Bismuth seeds, in combination with an alcohol-altered surface, give rise to superior nanowire uniformity, but there exist nanowire height limitations and fabrication can only proceed using volatile catalytic seeds maintained in a narrow window of processing parameters. The Bi_2Te_3 seeds are much more stable at the temperatures needed to initiate CdTe nanowire growth. This makes nanowire production possible without the cumbersome alcohol pre-treatment of the substrate's surface. The main disadvantage is that the nanowire size and shape distributions are severely compromised.

Over one hundred samples have been characterized for each of the two nanowire deposition methods. As a result, nanowire fabrication has been attempted over a broad range of growth conditions. Thus, the features presented here as unique to the Bi_2Te_3 initiated nanowires have been shown to decisively differentiate themselves from those observed using bismuth seeds deposited on an alcohol-altered surface. If, as expected, both the bismuth and Bi_2Te_3 catalytic seeds assume the same composition once exposed to a flux of cadmium and tellurium then the differences observed between the two methods must be attributed to the presence or absence of an alcohol-altered substrate surface. It is our conjecture that this can be done within the confines of the existing nanowire growth modes.

For both nanowire deposition methods the catalytic seeds are derived from a thin film that dewets at elevated temperatures. Once formed, these seeds are subject to Ostwald ripening, where there is an exchange of atoms along the substrate's surface with larger seeds growing at the expense of smaller ones[103, 104]. The effectiveness of this process is governed by the adatom's surface diffusion length given by the square root of the product of its diffusion coefficient and lifetime. If this length is larger than the separation between seeds then Ostwald ripening proceeds in the usual manner where, as time progresses, there is an increasing variation in seed size. On the other hand, if this length is reduced to where atoms liberated from one seed evaporate before encountering a second one, then a narrow size distribution will be maintained, but accompanied by a continuous reduction in the seed's diameter.

It is clear from our results that the pristine substrate used for the Bi_2Te_3 seeds leads to sufficient surface mobility for Ostwald ripening to broaden the distribution of seed diameters. Due to the higher volatility of tellurium we expect that this ripening process will result in bismuth-rich seeds. Indeed, the binary phase diagram indicates that the growth temperature is too low for the seeds to melt unless there is first a

substantial loss of tellurium[105]. The combination of Ostwald ripening in conjunction with evaporation leads to bismuth-rich catalytic seeds of different sizes which in turn cause nanowires of varying diameters. Corrupting the surface with alcohol alters this process by dramatically reducing the surface mobility; this increases the lifetime of the seed on the surface and frustrates the Ostwald ripening process, i.e., any bismuth atoms liberated from an individual seed are backscattered to the original seed or evaporate from the surface before reaching a second seed. With the ripening process halted, the distribution of seed diameters remains narrow, ultimately giving rise to a narrow distribution of nanowires.

With the catalytic seeds in place and exposed to a flux of cadmium and tellurium atoms it is expected that both the bismuth and Bi_2Te_3 seeds will evolve to the same ternary composition. While the ternary phase diagram for the cadmium/tellurium/bismuth system is unknown, it is well established that individually both tellurium and cadmium are soluble in bismuth[105]. The catalytic seed's ability to stabilize both elements on the timescales necessary for CdTe formation is crucial. This is made evident by the fact that the CdTe nanowires grow without a two-dimensional planar layer. This is attributable to the fact that both cadmium and tellurium have negligible sticking coefficients at the substrate temperature used. It is only through the formation of CdTe that these species have significant lifetimes on the substrate's surface. For the growth conditions used, however, the adatom lifetimes are too small to enable CdTe formation directly on the sapphire negating a planar growth mode. As a result, CdTe growth can only proceed through the catalytically driven process. Consistent with this analysis is a nanowire height distribution with the tallest nanowires having the largest diameters. This is in contrast to substrate-based nanowire growth modes where the tallest nanowires are those with the smallest diameters. For these systems, the nanowire height distribution is driven by adatoms arriving at the substrate's surface and making their way to the growth front via a random walk that takes them up the nanowire's sidewalls. For the CdTe case, the small adatom lifetime negates this process resulting in a nanowire growth mode that is dependent upon the direct impingement of atoms onto the catalytic seeds. Such a growth mode is not commonly observed in semiconductor nanowire systems.

A growth mode driven by direct impingement, where all the adatoms arrive normal to and are incorporated into the nanostructure, will result in a nanowire height distribution that is independent of diameter. There are, however, other factors

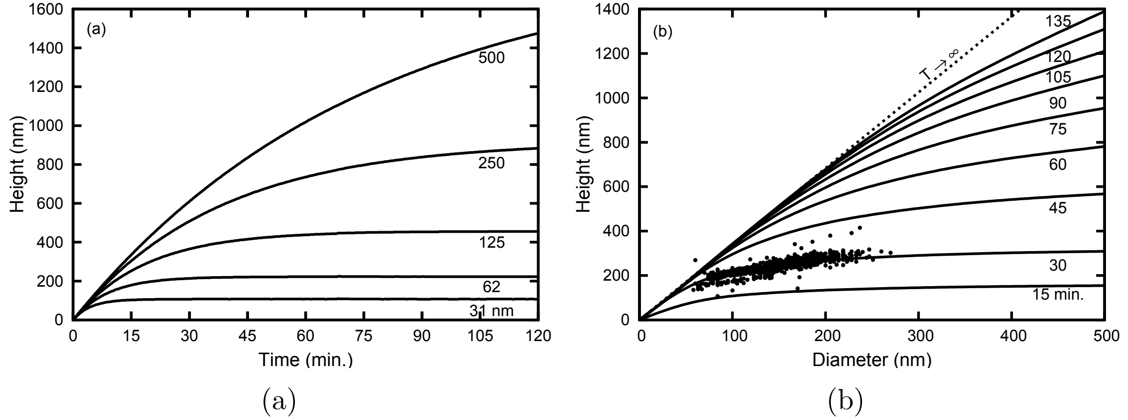

(a) (b)

Figure 8.8: Simulation results showing (a) the time evolution of the nanowire height for the five labelled diameters and (b) time snapshots of the height versus diameter dependence for the times labelled. The dashed line shows the linear dependence expected when all nanowires reach an equilibrium condition. Superimposed over the simulation is the experimental data (black dots) of Figure 8.4. The values used in this simulation have been scaled so to fit this experimental distribution.

that can come into play. It has been demonstrated both experimentally[106, 107] and theoretically[108, 109] that the Gibbs-Thomson effect can give rise to a height distribution directly proportional to the nanowire diameter. The effect stipulates that the higher curvature associated with smaller diameter seeds yields a higher effective vapour pressure, reducing the uptake of atoms from the impinging vapour. While this effect qualitatively gives rise to the observed CdTe nanowire height distribution, it is unable to account for the observed height limitation for the bismuth seeded nanowires as it provides no means of halting the growth.

The self-limiting growth mode displayed by the bismuth seeded nanowires deposited on an alcohol-altered surface likely originates from an equilibrium that develops between the addition of adatoms through direct impingement on the catalyst and the loss of atoms from the sidewalls through sublimation. The sublimation process is significant for the CdTe nanowires as they will disappear completely in approximately 30 min if left at the growth temperature without an incoming flux of cadmium and tellurium atoms. A similar situation must exist for the Bi_2Te_3 seeded nanowires, but in this case the results are complicated by the distribution of the nanowires' diameters and the lateral growth that becomes apparent for long growth times. A stochastic simulation was conducted to show the time evolution of the nanowires subject to a sublimation process. Arrays of nanowires with random diameters were exposed to a simulated

random flux of incoming atoms, atoms which caused them to grow larger while surface area caused them to sublimate. With the uptake of material being proportional to the area of the catalytic seed and the loss of material being proportional to the area of the sidewalls, the simulation yields nanowire heights showing the time evolution presented in Figure 8.8a. Snapshots in time of the nanowire height versus diameter distribution are shown in Figure 8.8b with the experimentally observed distribution of Figure 8.4a superimposed. The intent of this simulation was not to rigorously model the nanowire growth as it ignores such factors as the Gibbs-Thomson effect. It does, however, show that sidewall sublimation limits nanowire height and results in a size distribution qualitatively similar to that observed experimentally.

Essential to this work is the observation that Bi_2Te_3 seeded nanowires show a marked tendency towards lateral growth, while the bismuth seeded nanowires deposited on an alcohol-altered substrate do not. This tendency is displayed not only at long growth times, but also in the tapering shown at high growth rates and in the elongation of the slanted-top nanowires formed at the edge of the substrates. These three observations are consistent with the preferential nucleation of adatoms at the base of the nanowire where a weak nucleation site forms due to atomic bonding from both the sidewall facet and the substrate. Such a nucleation site would be analogous to the ones formed on a vicinal substrate[110]. The atoms forming at the base would then have to promote the propagation of a layer up the nanowire's sidewall. The existence of a lateral growth mode accounts for the formation of tall, large diameter nanowires for extended growth times (Figure 8.5). In the initial stages of growth the axial growth rate exceeds the lateral growth rate by a wide margin, but as the nanowire approaches its height limit the axial growth slows dramatically as shown in Figure 8.8a. The model presented, however, does not account for the situation where a slow lateral growth mode accompanies the axial growth. In this scenario, lateral growth results in larger diameter nanowires which, in turn, allow for increased axial growth. As a result, both dimensions will grow slowly in tandem provided that the catalytic material remains active as it spreads out over the expanding top surface of the nanowire.

Lateral growth is most evident for the slanted-top nanowires (Figure 8.5) as it proceeds in an anisotropic manner. In the PLD process cadmium and tellurium atoms exit the target from an area a few square millimetres in diameter. Thus, while the ablated material arrives normal to the centre of the substrate, it arrives at an angle to the edges. As a result, nanowires growing at the edges will have cadmium and

tellurium atoms preferentially landing on the sidewall facet nearest to the centre of the substrate. Thus, the adatoms have an increased likelihood of becoming a part of both the growth front nearest to that sidewall facet as well as any layer propagating up that sidewall. It is this asymmetry that leads to the anisotropic growth mode that is mirrored on opposite sides of the substrate.

The extent of the lateral growth at the base of the nanowire must be dependent upon the availability of adatoms on the surface of the substrate. At slow growth rates the nucleation of adatoms will be far more difficult as singly bonded atoms and small clusters of atoms will easily dissociate, making them prone to evaporation from the surface. At higher growth rates the availability of adatoms increases allowing for larger clusters to stabilize. Under these conditions the nanowires will have a small, but significant, collection area. The effect of this collection area, however, will diminish as one moves away from the surface of the substrate, a situation that should give rise to a tapered structure as shown in Figure 8.7.

As previously mentioned, these lateral growth modes are absent for the bismuth seeded nanowires deposited on an alcohol-altered substrate. It is our conjecture that during the dewetting process, the bismuth seeds are able to penetrate through this surface-altered layer in a manner that effectively cleans the surface and exposes the (0001) face of sapphire; a face essential to the epitaxial alignment of the nanowires. This statement is supported by the fact that a bismuth absorption/desorption treatment has been used to remove carbon-containing impurities from the surface of $SrTiO_3$ and $LaAlO_3$[111]. Around the periphery of each seed it is expected that the substrate's alcohol surface alteration persists. As a result, the nucleation site at the base of the nanowire is of poor quality as the substrate's epitaxial relationship no longer exists due to the corrupted surface. It is this deterioration in the nucleation site that inhibits the nanowire's ability to grow laterally. In general, poor adhesion of adatoms to the substrate should be detrimental to a lateral growth mode as adatoms must already have a low probability of attaching to the sidewall facet; if this were not the case a one-dimensional nanowire growth mode would be unattainable. The described process results in lateral overgrowth suppression in a manner analogous to that used for nanowire production through the use of selective area epitaxy. It is well established that CdTe is prone to such a process as there is a substantive body of work detailing procedures for obtaining selective epitaxy in the CdTe system[112–114]. Also supportive of this explanation are reports detailing the fabrication of vertically

aligned nanowires, where non-vertically aligned growth is eliminated through the use of organic layers[115–117].

8.4 Implications for Symmetry and Energy at Epitaxial Surfaces

The bond energy landscape of CdTe on oxide substrates like Al_2O_3 is already not particularly strong, as demonstrated by the CdTe thin film liftoff phenomenon. The additional chemical fouling of the sapphire substrate with alcohol has had the effect of both reducing the rate of nucleation on the substrate, and the diffusion rate of adatoms on the substrate surface. The carbon film on the surface is more chemically reactive with the Cd and Te adatoms than they are with the substrate. Only where the metal seeds are present can the adatoms reach the substrate and begin to assemble into the nanowire. Such chemical fouling resembles the process of surfactant layers deposited before epitaxial growth to enhance the diffusion of adatoms[118]. Here, the layer instead prevents the diffusion of adatoms.

This surface energy modification is a possible route to reducing or eliminating the parasitic thin film present during the growth of semiconductor nanowires. If the balance of growth temperature and chemical fouling can be optimized, higher quality nanowire devices may be possible.

Part IV

Noble Metals on Oxides

Chapter 9

Nanostructured Gold on Spinel

9.1 Introduction

As part of the investigations into VLS growth of CdTe nanowires, the control of the size and spatial distribution of metal seeds on oxides was investigated. CdTe nanowire growth had been previously successful using Bi and BiTe seeds, however they are unstable. Gold or another noble metal would expand the processing window both in terms of time and temperature. As such, experiments into the control of gold on oxide substrates was undertaken.

While ultimately nanowire growth was suspended in favour of other investigations, the research into the interactions of gold overlayers on $MgAl_2O_4$ (spinel) substrates yielded some surprising results. The standard method of producing metal seed particles is thermal dewetting, relying upon the relative surface energies of metal versus substrate to cause the film to ball up. The dewetting of gold on spinel substrates was found to result in epitaxial alignment and nanocrystal formation. A full characterization into the formation process of the gold nanocrystals was undertaken and a phenomenological model of their formation was presented. This work was published as:
Gabriel A Devenyi, Jianfeng Li, Robert A Hughes, An-Chang Shi, Peter Mascher, and John S Preston. "Epitaxially driven formation of intricate supported gold nanostructures on a lattice-matched oxide substrate". In: *Nano letters* 9.12 (2009-12), pp. 4258–63. ISSN: 1530-6992. DOI: 10.1021/nl902491g [119]. This work was done in collaboration with Jianfeng Li, a Ph.D. candidate in Physics at McMaster University, who performed the modelling of the formation of nanostructures, all other measurements and sample preparation were performed by me.

9.2 Experimental

The gold nanostructures were formed through the deposition of gold films on $MgAl_2O_4$ substrates (MTI Corp.) followed by an annealing procedure which facilitated film dewetting and nanostructure formation. The films were sputter-coated at room temperature to a thickness of 5–15 Å with a GATAN PECS Model 682 ion beam coating/etching system. The samples were then placed in a tube furnace with a 100 SCCM flow of argon, heated to 1100℃ in 45 min, and then held at that temperature for 1 h. Following this treatment, the sample was cooled to 1000℃ in 30 min, held at that temperature for an additional hour, and then allowed to cool to room temperature

over an interval of approximately 8 h. Holding the temperature at both 1100 and 1000℃ was crucial to the formation of the nanostructures described here. Removal of either step results in the formation of faceted gold spheres sitting directly on the substrate.

Scanning electron microscopy (SEM) images of the gold nanostructures formed on the (100), (111), and (110) $MgAl_2O_4$ substrates, obtained using a JEOL-7000F SEM in secondary electron mode, are shown in Figure 9.1. For each substrate orientation, one observes two types of features, (i) spheres supported by a necking region attached to a geometrically shaped base (Figure 9.1a-c) and (ii) standalone base structures (Figure 9.1d-f). Convergent beam electron diffraction (CBED) performed using a Phillips CM12 confirmed that the supported spheres are crystalline. For each case, the shape of the base structure reflects the underlying symmetry of the substrate which is four-fold, three-fold, and two-fold symmetric for the (100), (111), and (110) surfaces. X-ray diffraction measurements, using a Bruker 6000 CCD detector on a Bruker three circle D8 goniometer with a Rigaku RU-200 rotating anode Cu KR X-ray generator and parallel-focusing mirror optics, were used to determine the substrate orientation relative to the edges of the base structures and are denoted on the three top-down SEM images (Figure 9.1d-f).

9.3 Results and Discussion

The crystallographic alignment of the nanostructures is a clear indication of epitaxy and is strongly suggestive of 111 gold faceting of the base structures associated with the [100]- and [111]-oriented substrates. For the (110) surface, the standalone base structures are ill-defined and show no obvious faceting, while those formed in combination with a sphere show shapes consistent with mixed faceting, possibly having {111} and {100} facets for the short and long dimension. The standalone base dimensions are uniform with side lengths of 40, 65, and 65 nm × 110 nm for the (100), (111), and (110) substrates.

While there are two basic types of nanostructures formed on each substrate orientation, these structures are found in various stages of development. For the most part, the bases are well-developed and show little size variation. The spherical structures, however, vary dramatically both in their size and position relative to the base structures. Figure 9.2 shows a series of top-down SEM images for the case of the (111)

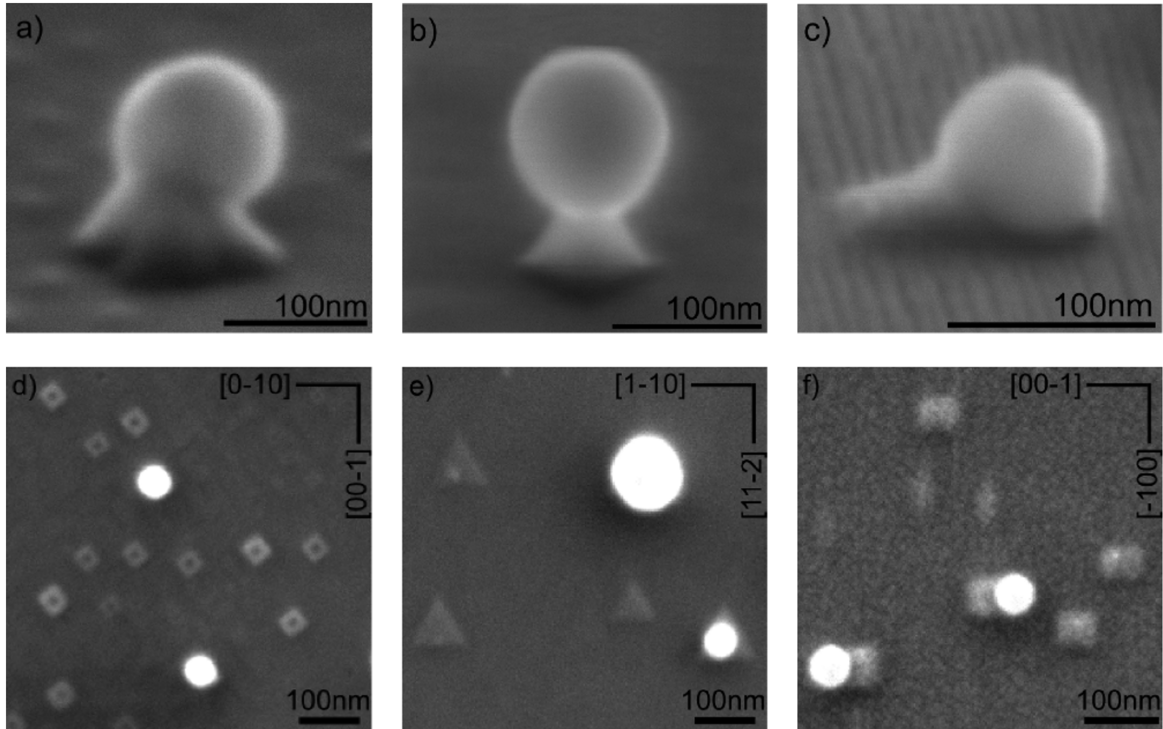

Figure 9.1: SEM images showing the gold nanostructures formed on $MgAl_2O_4$ substrates. The three upper images show spheres supported by a necking region attached to a geometrically shaped base for the (a) [100]-, (b) [111]-, and (c) [110]-oriented substrates. Each of these images was taken at a 70°tilt. The aura seen around nanostructures is an artifact of imaging. The three lower images show the top-down view of both standalone base structures and supported spheres for the (d) [100]-, (e) [111]-, and (f) [110]- oriented substrates. The in-plane Miller indices of the substrate are denoted on each of these images. For all cases, the samples were coated with a thin layer of platinum to improve imaging. Imaging without platinum shows the same structures but is of poor quality due to substrate charging effects.

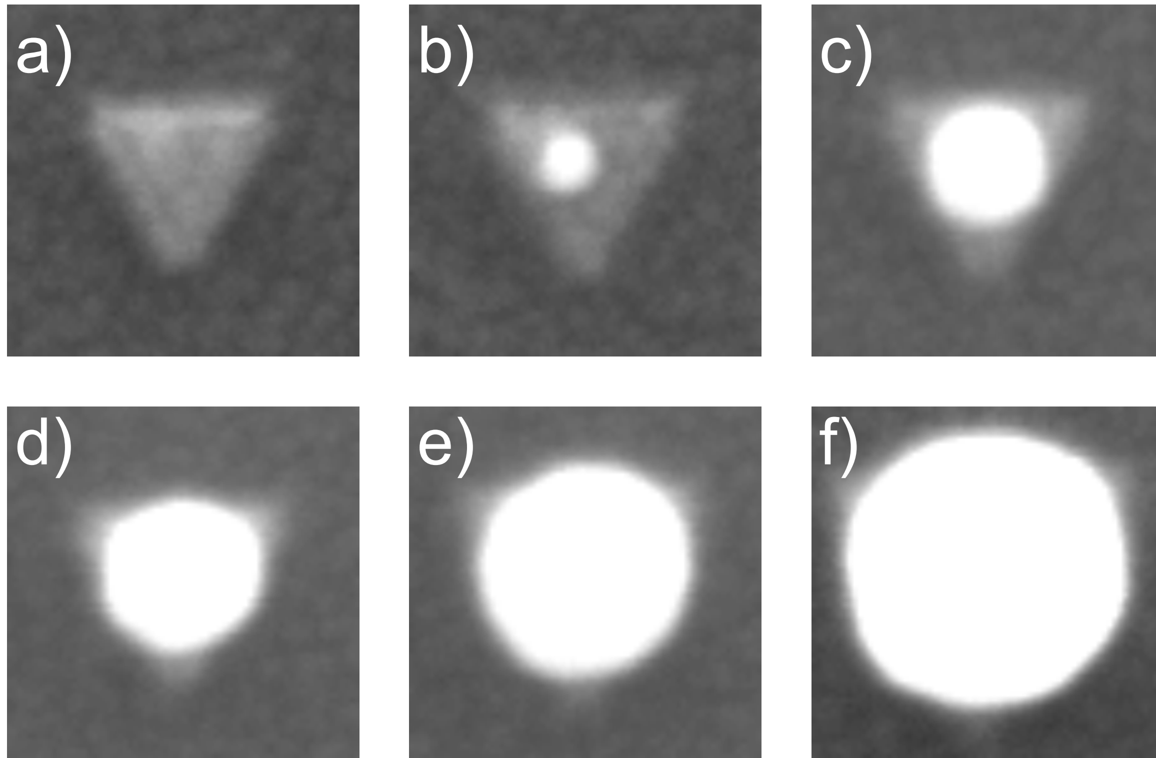

Figure 9.2: SEM images showing the top-down view of gold nanostructures formed on the (111) surface of $MgAl_2O_4$ substrates. The sequence of images is chosen to show progressively larger spheres atop the base structures. Only the smallest sphere, shown in b), is offset from the centre of the triangular base and that the base size is slightly larger when supporting larger spheres, as happens for e) and f). The size of each image is $130{\times}30$ nm^2.

$MgAl_2O_4$ substrate showing an evolution of the nanostructures from a standalone triangular base to bases supporting spheres of increasing size. Notable is the fact that the nanostructure, shown in Figure 9.2b, manifests itself as a small sphere which is offset from the centre of the base while for the larger spheres, this asymmetry disappears. Such asymmetries are observed for all three substrate orientations, but only those nanostructures formed on the (111) substrate consistently show a centrally placed sphere for the large sphere sizes. There is also a systematic effect whereby the size of the triangular base structure increases for sphere diameters greater than 80 nm (see Figure 9.2e and f).

The base structures formed on each substrate orientation are a clear consequence of the epitaxial relationship formed between gold and the latticed-matched $MgAl_2O_4$ substrate. This is apparent from the fact that the geometries of the base structures

mimic the underlying symmetry of the substrates. It is also likely that the base sizes are a consequence of the substrate-imposed strains. Arguments based on epitaxy, however, cannot explain the self-assembly of the gold spheres atop the base structures and the associated necking behaviour which facilitates their connection to the base. It is our hypothesis that the necking behaviour results from an attempt to minimize the surface energy of the structure. Thus, the overall shape of these nanostructures is governed by an interplay between the constraints imposed by epitaxy and a requirement that the surface free energy be minimized. This situation has much in common with formation of soap bubbles affixed to a wire frame[120]. This statement is based on the facts that the frame imposes a constraint analogous to that imposed by lattice mismatch and that the shape of the soap bubble is, to a large degree, determined by the surface free energy. This analogy provided the impetus for applying the well-developed models associated with soap bubble formation to the nanostructures described here. Such modelling has also been successfully used to predict the equilibrium shape of biological lipid bilayers (blood cells) when exposed to abnormal pressure, temperature, magnetic, and chemical environments[121–126].

The gold nanostructures were modelled as a continuum elastic surface constrained by a footprint. Three different footprint geometries (square, equilateral triangle, and rectangle) were used in order to mimic the four-fold, three-fold, and two-fold symmetries associated with the (100), (111), and (110) surfaces of $MgAl_2O_4$. The size and shape of the footprint were kept constant during the simulated growths in order to match the experimental observation indicating a high degree of base uniformity. For each orientation, the contact angle (i.e., the angle between the footprint plane and the tangent plane of any surface connected to the footprint's edge) was set to a constant where the value was chosen to be consistent with the observed faceting, as is schematically shown in Figure 9.3.

With these constraints, the shape of an open elastic surface can be fully described by the mean curvature, H, and the Gaussian curvature (K), while its corresponding elastic properties can be characterized by a bending modulus $\varkappa$and a Gaussian modulus $\varkappa_G$. The surface energy (F) can then be formulated as

$$F = \int \frac{\kappa}{2} H^2 dA + \int \kappa_G K dA + \lambda S + PV \quad (9.1)$$

where λ, V, S, and dA are the particle's surface tension, volume, total surface area, and

surface area element[127, 128]. The pressure (P), serves as a Lagrange multiplier which ensures that a constant volume is enclosed between the structure and the footprint plane. The second term gives the integrated Gaussian curvature, which is constant according to the Gauss-Bonnet theorem[129]. For a given surface tension and volume, the equilibrium shape will correspond to an energy minimum determined by the shape equation $\delta F = 0$. The structures are more readily solved by first rescaling the free energy of the model to become dimensionless, such that

$$\tilde{F} = \int \left(\frac{\tilde{\kappa}\tilde{H}^2}{2} + 1 \right) d\tilde{A} + \tilde{P}\tilde{V} \tag{9.2}$$

where

$$\tilde{A} = A/S_0 \qquad \tilde{V} = V/S_0^{3/2} \qquad \tilde{H} = HS_0^{1/2}$$
$$\tilde{\kappa} = \kappa/\lambda S_0 \qquad \tilde{P} = PS_0^{1/2}/\lambda \qquad \tilde{F} = F/(\lambda S_0)$$

and S_0 is the area of the base. Thus, according to this dimensionless free-energy expression, there are two independent controlling parameters, $\tilde{\kappa}$ P.

Helfrich and Ou-Yang[127] have analytically solved the shape equation for some symmetrical geometries. For the work presented here, the surface is sectioned into discrete elements using a triangulation mesh, and a simple dissipative model is used to minimize the energy, as in Equation (9.2)[130]

$$\frac{\delta \mathbf{r}}{\delta t} = -M \frac{\delta \tilde{F}}{\delta \mathbf{r}} \tag{9.3}$$

where $\mathbf{r(t)}$ is the position vector of a point on the particle surface at time (t) and M is a kinetic coefficient. These methods, developed by Taniguchi et al.[130], are, however, unable to simulate large deformations. To circumvent this limitation, we employed two techniques, equiangulation and vertex averaging, available through the Surface Evolver software developed by Brakke et al.[131]. Following the procedure of Lim et al.,[121, 124, 125] the curvature was discretized based on the methods of Julicher[132], which exactly describe the curvature in the continuum limit.

The variational derivative used in the triangulation scheme was evaluated analytically. For the Surface Evolver technique, variables were solved numerically when analytical variations for discrete curvatures proved difficult.

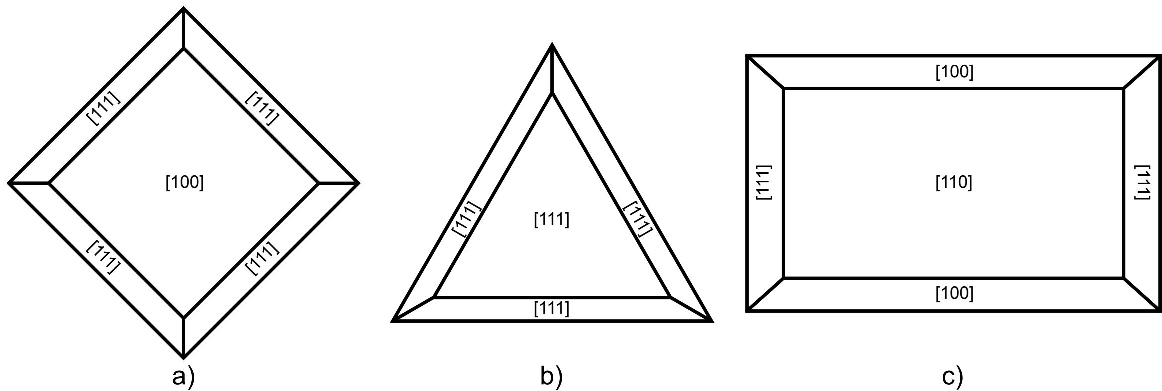

Figure 9.3: Proposed faceting of the base structures grown on (a) [100]-, (b) [111]-, and (c) [110]-oriented substrates.

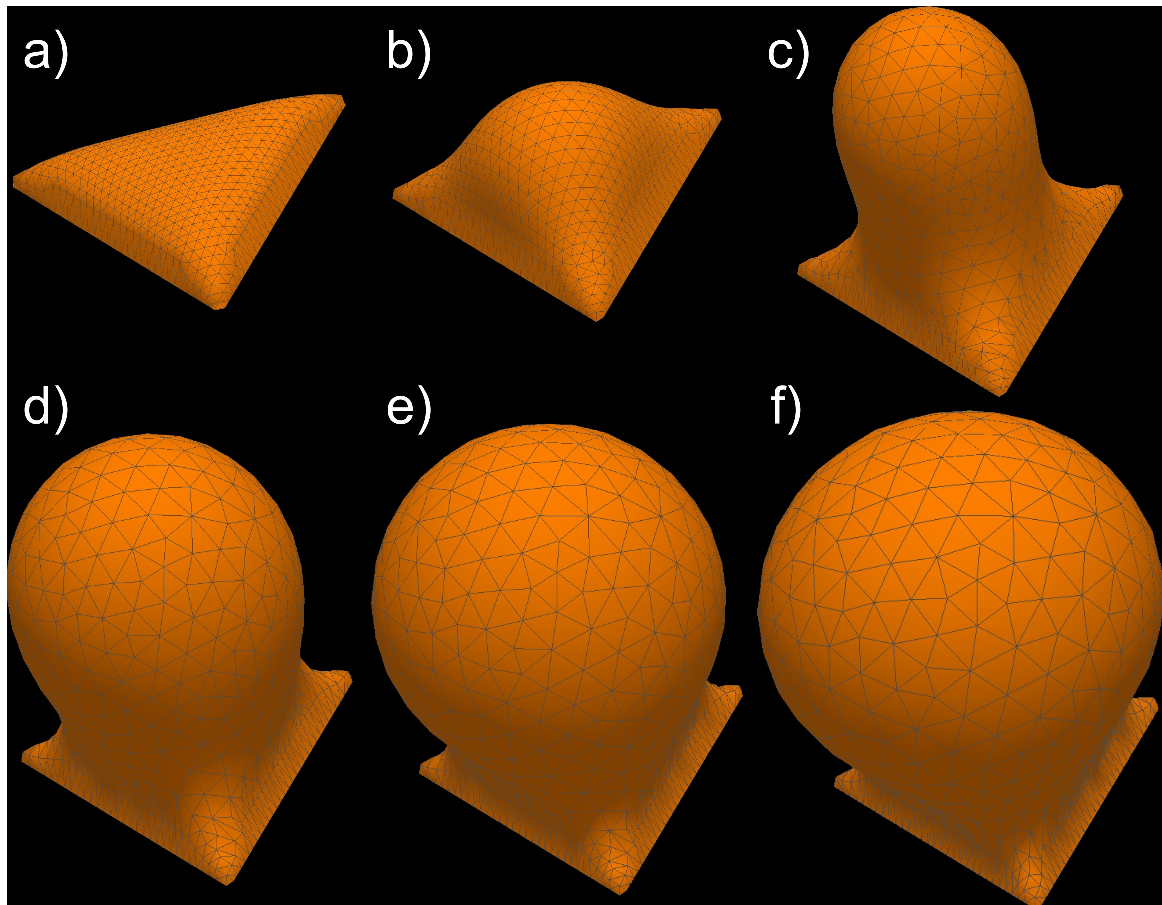

Figure 9.4: Simulations based on the continuum elastic model showing the shape evolution of structures with a triangular footprint as the total volume is progressively increased. The shape of these modelled structures resembles that of the self-assembled gold nanostructures formed on (111) $MgAl_2O_4$ substrates (Figure 9.1b and e and Figure 9.2). The scale is in arbitrary units.

Using the numerical methodology, a progression of structures with increasing volume were calculated using square, triangular, and rectangular footprints having contact angles of 54.7°, 70.5°, and 35° (long-axis) by 45° (short-axis). The chosen contact angles are consistent with the inferred faceting, as shown in Figure 9.3. For each case, the footprint area and surface tension are set to unity, while the bending modulus is allowed to vary. Figure 9.4 shows the calculated progression for the triangular footprint. As the volume is increased, there is an evolution from a nearly flat base, to a base with a bulge, and then finally to a spherical structure supported by a necked region to a triangular base. These simulated structures are similar to the gold nanostructures formed on the (111) $MgAl_2O_4$ substrate (see Figure 9.1b and c and Figure 9.2). Similar trends are observed for the square and rectangular footprints. Figure 9.5 shows the simulated high volume structures for the square and rectangular footprints, which, once again, are consistent with experimental observations. The simulations do not, however, account for any of the observed asymmetries.

The shape of the base structures of the self-assembled gold nanostructures is strongly influenced by epitaxy and the underlying symmetry of the substrate surface. That being said, it is difficult to account for the hollowed-out center observed for the base structure formed on the (100) $MgAl_2O_4$ using epitaxy-based arguments. This feature is, however, predicted by the continuum elastic model. Figure 9.6a shows the topographical color map obtained from the modelling for the low-volume structure. It shows a circular depression in the middle of the structure as well as a lobe near each corner. Motivated by the simulation results, we examined the topography of the self-assembled gold nanostructure using atomic force microscopy (AFM). Figure 9.6b shows a tapping mode AFM image of the base structure obtained using a Digital Instruments scanning probe microscope (SPM) and a NanoScope IIIa controller. Even though the features of the nanostructure are somewhat washed out since the resulting image is a convolution of the nanostructure and the AFM tip geometry, the nanostructure's four lobes and central depression are visible.

Taken together, the experimental observations and the continuum elastic modelling results strongly suggest that epitaxy and a minimization of the surface free energy are the two primary drivers in determining the shape and size of the self-assembled gold nanostructures. The fact that similar structures have not been previously observed is likely a consequence of the synthesis route used. The route employed here not only involves temperatures well in excess of those typically used when forming

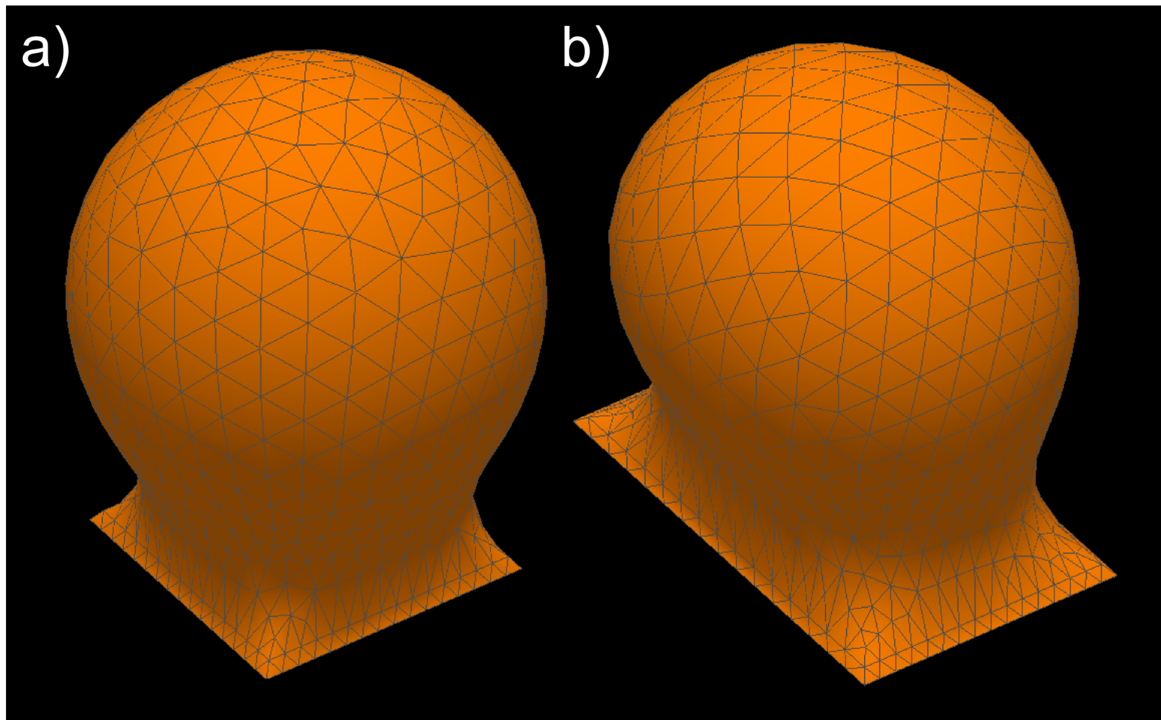

Figure 9.5: Simulations based on the continuum elastic model showing the expected high volume shape for the (a) square and (b) rectangular (length:width) 1.42:1 footprints. These structures show a resemblance to the self-assembled gold nanostructures formed on the (100) and (110) $MgAl_2O_4$ substrates (Figure 9.1) but show none of the observed asymmetries. The scale is in arbitrary units.

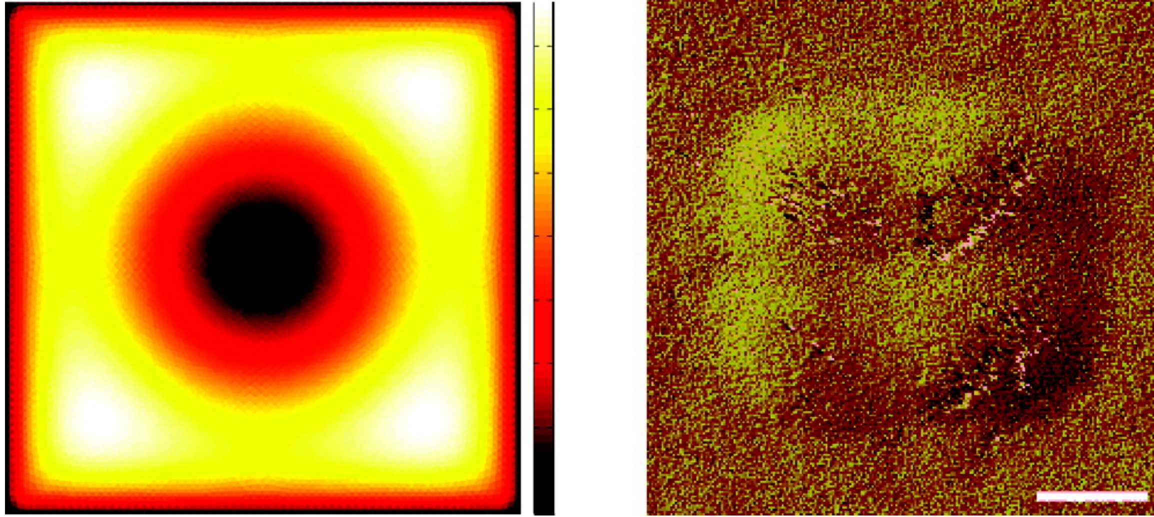

Figure 9.6: A comparison of the (a) topographical colour map derived from the continuum elastic model and (b) the AFM image of a self-assembled gold nanostructure deposited on the (100) $MgAl_2O_4$ substrate. The simulation predicts both the presence of four lobes at the corners and a central depression. The scale of the topographic image is arbitrary, and the scale of the AFM image is 10 nm.

substrate-supported nanostructures but also requires an annealing profile which accesses two temperatures. It is possible that the initial 1100℃ anneal is needed to induce surface reconstructions in the $MgAl_2O_4$ substrates which are essential to the growth of these nanostructures. Surface reconstructions have been shown to strongly influence the growth of both nanostructures[133–135] and thin films[87] when using (100) SrTiO3 substrates. We, however, consider it more likely that the formation of these nanostructures requires temperatures in excess of the melting point of bulk gold (1064℃). Significant deviations from the bulk value, due to finite size effects, are considered unlikely since such effects appear to occur only in nanostructures smaller than 5 nm[136]. Once molten, the nanostructures are cooled to 1000℃ and held at this temperature, which is just below the melting point. Such a temperature allows for solidification while maintaining high adatom mobility. The fact that this fabrication step is crucial to the formation of the observed intricate nanostructures provides compelling evidence that substantial adatom motion is essential. In this scenario, it is likely that an Ostwald-like ripening process will play a role where larger nanostructures grow at the expense of smaller ones. Substrate surface steps, due to the inherent miscut of the substrate[137], could also influence the process by providing energetically favourable nucleation sites. Nanostructure formation is also heavily reliant on the

epitaxial relationship between the nanostructure base and the underlying substrate. This relationship determines the crystallographic alignment of the base structures, while the consistency in size is likely a consequence of the strain imposed by lattice mismatch. Once the 1000℃ anneal ends, the adatom motion will be quickly quenched by the lower temperatures, allowing no further alterations to the shape or size of the nanostructures. The result is intricately shaped nanostructures whose size and shape are determined by a minimization of the surface free energy while simultaneously being subject to the constraints imposed by epitaxy.

9.4 Implications for Symmetry and Energy at Epitaxial Surfaces

Despite the materials of interest in this investigation consisting of a noble metal and a complex oxide, materials which one would expect very little interaction instead result in epitaxial alignment. This epitaxial alignment is simple in the sense that the nanocrystal orientations follow directly from the underlying substrate. The epitaxial alignment is complicated by the fact that gold fits onto sublattice of half of a $MgAl_2O_4$ lattice. Such epitaxy relies on the symmetry of the surface atoms forming a lattice with a smaller lattice constant than the bulk crystal. This epitaxy can thus be thought of as nanocrystal forming on a reconstructed surface, since the surface atoms present a surface net with a different lattice parameter than the bulk.

The more surprising result from this work is the epitaxial alignment possible between nonreactive materials. Noble metals are not known to readily react with other elements or compounds other than to form simple metallic bonds. Similarly, metals overall are not known to strongly wet oxide surfaces, preferring to bond to themselves instead. Complex oxides are also known to be stable to high temperatures, and stable when exposed to reactive compounds. To mix such two compounds and observe something other than segregation and no interaction is surprising. These experiments have shown that, despite there being a weak interaction between the two materials, due to low reactivity, epitaxial alignment is achieved through a careful thermal treatment. The subtle influence of the substrate's lattice can impart alignment of the gold, overriding the tendency to form an equilibrium crystal shape.

Part V

Closing Discussions

Chapter 10

Future Work

10.1 Surface Reconstructions

The role of surface reconstructions in epitaxial crystal growth offers a rich field of future research. Both reconstructions involving steps and the atomic reconstructions of surfaces offer routes to driving epitaxial growth into new regimes not previously observed.

10.1.1 Twinning Control

In this work, offcut substrates and the surface reconstructions induced by them were demonstrated to be effective at suppressing the twinning common in face centred cubic semiconductors. These offcut substrates were all offcut toward the (110) direction, resulting in reconstructions and steps along a perpendicular (110) direction, leaving long terraces. Such stepping was successful at suppression twinning along that direction, but had no impact in the perpendicular direction. If instead the substrate is offcut towards a (100) direction, when reconstructed the resulting terraces will have step edges towards to perpendicular {110} directions. Such a reconstructed surface may be able to suppress twinning in both directions, resulting in overall a higher quality epitaxial growth.

10.1.2 Lattice Matched Growth on Reconstructions

This work showed that the locked-in high temperature reconstruction of a crystalline oxide could successfully support alignment of an epitaxial crystal of orientation different than that of the bulk crystalline substrate. While in this case the epitaxial growth was not substantially improved, there are a huge variety of stable surface reconstructions reported in the literature. These surface reconstructions may offer lattice matches to epitaxial crystals, allowing high quality growth were no bulk crystalline substrate exists.

Undergoing such a research project would require a survey of existing literature of surface reconstructions. Many publications do not provide the exact lattice spacings of atoms of the surface reconstruction. Participation of researchers which can successfully measure surface reconstructions would be essential to construction an extensive database. Once such a database were developed the lattice spacings of such

reconstructions could be compared to existing epitaxial thin films and candidate pairs could be investigated by a variety of growth techniques.

The benefits of such systems would be the leveraging of existing substrates for the production of new epitaxial crystals.

10.2 Epitaxial Liftoff

The epitaxial liftoff process of CdTe/Al_2O_3 is a very surprising result considering the single crystal nature of film. There are a number of other materials which offer comparable lattice matches to either sapphire or another complex crystalline oxide. If these systems also exhibit the liftoff phenomenon the physics involved in such a process become even more interesting, and their engineering applications could allow previously expensive materials to be used in many systems. A patent application regarding the generalized liftoff process of crystalline materials on oxide substrates has been submitted and is being evaluated by the United States Patent Office.

10.2.1 Other II-VI Liftoff

Building on the prior successes of liftoff of CdTe on sapphire it is expected that systems in the same chemical family may also exhibit the liftoff phenomenon. Based on these expectations, some preliminary experiments have been performed on CdTe grown on MgO and ZnTe grown on sapphire. While CdTe/MgO does not result in a particularly high quality film due to the high chemical symmetry of the MgO surface, CdTe was found to a similar extent when grown on MgO. Similarly, as part of the continued investigation into II-VI systems, ZnTe/Al_2O_3 can be grown single phase with reasonable quality and also exhibits liftoff.

(a) (111) pole figure of ZnTe epitaxially grown on sapphire.

(b) (111) pole figure ZnTe after liftoff on polysulphone carrier.

Figure 10.1: Pre- and post-liftoff ZnTe pole figures.

10.2.2 III-V Liftoff

There are several lattice matched or nearly lattice matched III-V material systems to single crystal oxide substrates. Often these systems have never had any attempts to grow epitaxial crystals. There is an expansive field of research open to investigate the growth of III-V materials on oxides.

One material system which was readily available for cursory experiments was InSb/Al_2O_3 which has a very similar lattice match to sapphire as CdTe. Initial investigations into InSb growth via MBE yielded films with twin volumes of ∼25% comparable to poor CdTe grows. InSb/Al_2O_3 was also found to express the liftoff phenomenon.

The success of multiple substrate structures as well as the successes of both II-VI and III-V films indicates a number of other systems may also exhibit liftoff. The oxide substrates YAG, $PbWO_4$, GGG and YSZ offer suitable lattice matches to attempt single crystal growth which may then facilitiate liftoff. A full list of potential Semiconductor/Oxide lattice matches for liftoff will be presented in Appendix A.

10.2.3 Physics of Liftoff

The wide range of materials which are expected to exhibit liftoff provides a rich research space to investigate the physics of liftoff. Immediate investigations into epitaxial process can be undertaken using density functional theory to investigate the energy landscape of the individual material systems at minimal cost. Interface sensitive in-situ growth characterization tools may provide some insight into the initial nucleation of layers during growth. Other buried interface techniques will need to be used to gain further insight into the liftoff process. The reverse process of attempting to grow an oxide on a semiconductor crystal may also provide some insight into the physics of liftoff.

10.2.4 Engineering of Liftoff

The liftoff processes performed thus far have used adhesive tapes or polymer carriers, investigating the simplicity of the liftoff process itself and the properties of the resulting films. Besides examining physics of the process and expanding the material systems which have been demonstrated, there are a number of questions of engineering and application that could be explored.

Optimization of liftoff yield while still allowing for further processing is a delicate balance of strong and rigid carriers which are also potentially removable. Some of these are now being investigated (polymers, wafer bonding) while there are others which have yet to be (vacuum, metal foils). Integration into electronic systems may require patterning or lithographic steps, the impact of such lithography on liftoff will also need to be investigated.

10.3 Gold on Spinel

The initial investigation of gold on spinel relied upon the discovery of a reproducible formation process and the measurement and modelling of the nanostructure formation process. The exact role of thickness, temperature, heating and cooling rate, and time spent at temperature were not investigated. A thorough investigation of such parameters has the potential to improve the formation density, uniformity and size. Control of such parameters is essential if such nanostructures are to be used in applications.

Some investigations into the formation of these nanostructures have found that the formation process is much richer than initial models investigations suggested. The spinel substrate, originally thought to be stable and static, appears to undergo significant solid state diffusion under the influence of gold. The substrate material appears to compose a significant portion of the intricate nanostructure. Work preformed by Tahereh Majdi has expanded the effective processing range and provided extensive TEM characterization[138].

Chapter 11

Conclusions

The investigations presented here have provided insight into a number of unique cases of epitaxy. In this work, two themes outside the usual epitaxial process were examined, unusual symmetry and unusual energy relationships between the host substrate and the epitaxial crystal. Examinations of symmetry involved epitaxy of systems where the 2D symmetry net is preserved over the interface, while the two crystals themselves have different symmetries or where symmetry is broken across the interface. Examinations of unusual energy relationships involved polar on non-polar epitaxy of face-centred cubic semiconductors as well as epitaxial growth on oxide substrates.

On the theme of symmetry this work has documented cases where surface reconstructions through steps, a case of symmetry breaking, has resulted in suppression of twinning growth defects, improving epitaxial thin film quality. The role of the asymmetric (211) surface, again a case of symmetry breaking, has shown that interfacial misfit strain can be accommodated even for largely mismatched systems. Investigations into the surface reconstructions of oxide substrates resulted in insight into how the step-flow growth mode induced by steps can preferentially nucleate and grow textured epitaxial thin films to improve film quality. The surface reconstructions of oxide substrates have also been shown to successfully nucleate epitaxial thin films of a different orientation than those nucleated on the bulk substrate, through a transformation of the surface lattice constant, opening up a new field of epitaxial matches with surface reconstructions.

On the theme of energy, this work has demonstrated that epitaxial growth can occur between materials and substrates which are traditionally considered to be weakly bonding. This weak bonding regime was found to be so weak that liftoff of epitaxial thin films and reuse of the resulting substrates was possible. Furthermore, the weak epitaxial regime between noble metals and oxides was explored and demonstrated some novel intricate nanostructure formation in materials which generally considered to be very stable. Finally, investigations into the growth of CdTe nanowires demonstrated a method of surface preparation which can control the nucleation and growth process of these nanowires by modifying surface energies.

The results from these two themes have expanded the conditions under which epitaxial growth can be expected in two key ways, surface reconstructions can provide new surface lattice constants for growth, and weak chemical attraction between materials does not immediately negate good epitaxy. Both these results open up new fields for

research and challenge other fields to provide the necessary supporting measurements to advance these ideas further.

Bibliography

[1] Helmut Föll. *Hyperscript to Semiconductor Technology.* 2013. URL: http://www.tf.uni-kiel.de/matwis/amat/semitech_en/ (visited on 2013-08-15) (cit. on p. 3).

[2] Herbert Kroemer. "POLAR-ON-NONPOLAR EPITAXY". In: *Journal of Crystal Growth* 81 (1987), pp. 193–204 (cit. on pp. 2, 16, 65).

[3] Thierry Duffar and Amal Nadri. "On the twinning occurrence in bulk semiconductor crystal growth". In: *Scripta Materialia* 62.12 (2010-06), pp. 955–960. ISSN: 13596462. DOI: 10.1016/j.scriptamat.2010.02.034 (cit. on p. 12).

[4] S. Takeuchi and K. Suzuki. "Stacking Fault Energies of Tetrahedrally Coordinated Crystals". In: *Physica Status Solidi (a)* 171.1 (1999-01), pp. 99–103. ISSN: 00318965. DOI: 10.1002/(SICI)1521-396X(199901)171:1<99::AID-PSSA99>3.0.CO;2-B (cit. on p. 12).

[5] Mario Einax, Wolfgang Dieterich, and Philipp Maass. "Colloquium: Cluster growth on surfaces: Densities, size distributions, and morphologies". In: *Reviews of Modern Physics* 85.3 (2013-07), pp. 921–939. ISSN: 0034-6861. DOI: 10.1103/RevModPhys.85.921 (cit. on p. 12).

[6] DJ Dunstan. "Strain and strain relaxation in semiconductors". In: *Journal of Materials Science: Materials in Electronics* 8 (1997). DOI: 10.1023/a:1018547625106 (cit. on p. 13).

[7] Douglas J Paul. "Si/SiGe heterostructures: from material and physics to devices and circuits". In: *Semiconductor Science and Technology* 19.10 (2004-10), R75–R108. ISSN: 0268-1242. DOI: 10.1088/0268-1242/19/10/R02 (cit. on p. 13).

[8] Milton Ohring. *Materials Science of Thin Films.* 2nd ed. San Diego: Elsevier Science, 2001. ISBN: 9780080491783 (cit. on pp. 14, 20, 22, 28, 29, 31).

[9] John C. Bean. “The Growth of Novel Silicon Materials”. In: *Physics Today* 39.10 (1986), p. 36. ISSN: 00319228. DOI: 10.1063/1.881067 (cit. on p. 15).

[10] NE Christensen, S Satpathy, and Z Pawlowska. “Bonding and ionicity in semiconductors”. In: *Physical Review B* 36.2 (1987-07), pp. 1032–1050. ISSN: 0163-1829. DOI: 10.1103/PhysRevB.36.1032 (cit. on p. 16).

[11] D. K. Biegelsen, R. D. Bringans, and J. E. Northrup. “Heteroepitaxial growth of polar semiconductors on non-polar substrates”. In: *Materials Science and Engineering: B* 14.3 (1992-08), pp. 317–331. ISSN: 09215107. DOI: 10.1016/0921-5107(92)90315-Z (cit. on p. 16).

[12] J A Venables, G D T Spiller, and M Hanbucken. “Nucleation and growth of thin films”. In: *Reports on Progress in Physics* 47.4 (1984-04), pp. 399–459. ISSN: 0034-4885. DOI: 10.1088/0034-4885/47/4/002 (cit. on pp. 18, 19).

[13] Wikipedia. *Surface energy — Wikipedia, The Free Encyclopedia*. [Online; accessed 30-August-2013]. 2013. URL: http://en.wikipedia.org/w/index.php?title=Surface_energy&oldid=553535131 (cit. on p. 19).

[14] Charles B. Duke. “Semiconductor Surface Reconstruction: The Structural Chemistry of Two-Dimensional Surface Compounds”. In: *Chemical Reviews* 96.4 (1996-01), pp. 1237–1260. ISSN: 0009-2665. DOI: 10.1021/cr950212s (cit. on p. 21).

[15] K Oura, V G Lifshits, A A Saranin, and A V Zotov. *Surface Science: An Introduction*. Advanced Texts in Physics. Springer, 2010. ISBN: 9783642056062 (cit. on pp. 21, 30).

[16] Zhenyu Zhang, Fang Wu, and Max G Lagally. “AN ATOMISTIC VIEW OF Si(001) HOMOEPITAXY”. In: *Annual Review of Materials Science* 27.1 (1997-08), pp. 525–553. ISSN: 0084-6600. DOI: 10.1146/annurev.matsci.27.1.525 (cit. on p. 23).

[17] Max G. Lagally. “Atom Motion on Surfaces”. In: *Physics Today* 46.11 (1993), p. 24. ISSN: 00319228. DOI: 10.1063/1.881367 (cit. on p. 23).

[18] OL Alerhand, A.N. Berker, JD Joannopoulos, David Vanderbilt, RJ Hamers, and JE Demuth. “Finite-temperature phase diagram of vicinal Si(100) surfaces”. In: *Physical Review Letters* 64.20 (1990-05), pp. 2406–2409. ISSN: 0031-9007. DOI: 10.1103/PhysRevLett.64.2406 (cit. on p. 25).

[19] E Pehlke and J Tersoff. "Phase diagram of vicinal Si (001) surfaces". In: *Physical Review Letters* 67.10 (1991), pp. 1290–1293. DOI: 10.1103/PhysRevLett.67.1290 (cit. on pp. 27, 66).

[20] ASTM. *ASTM C71 - Standard Terminology Relating to Refractories.* 2006. DOI: 10.1520/C0071-12 (cit. on p. 27).

[21] Elizabeth a. Wood. "Vocabulary of Surface Crystallography". In: *Journal of Applied Physics* 35.4 (1964), p. 1306. ISSN: 00218979. DOI: 10.1063/1.1713610 (cit. on p. 28).

[22] Vitalij K. Pecharsky and Peter Y. Zavalij. *Fundamentals of Powder Diffraction and Structural Characterization of Materials.* Kluwer Academic Publishers, 2003. ISBN: 9780387095790 (cit. on p. 34).

[23] Bob B. He. *Two-Dimensional X-Ray Diffraction.* Hoboken, NJ, USA: John Wiley & Sons, Inc., 2009-07. ISBN: 9780470502648. DOI: 10.1002/9780470502648 (cit. on pp. 36, 38, 40, 42, 43).

[24] Steffen Weber. *WinWulff.* 2006 (cit. on p. 43).

[25] J. Goldstein, D.E. Newbury, D.C. Joy, C.E. Lyman, P. Echlin, E. Lifshin, L. Sawyer, and J.R. Michael. *Scanning Electron Microscopy and X-ray Microanalysis.* 3rd. Springer Science, 2003. ISBN: 9780306472923 (cit. on pp. 50–52).

[26] Ray F. Egerton. *Physical Principles of Electron Microscopy.* Boston, MA: Springer US, 2005. ISBN: 978-0-387-25800-3. DOI: 10.1007/b136495 (cit. on p. 53).

[27] Helmut Kohl and Ludwig Reimer. *Transmission Electron Microscopy.* Vol. 36. Springer Series in Optical Sciences. New York, NY: Springer New York, 2008. ISBN: 978-0-387-40093-8. DOI: 10.1007/978-0-387-40093-8. URL: http://www.springerlink.com/index/10.1007/978-0-387-40093-8 (cit. on p. 55).

[28] Stephen M Jovanovic. "Pulsed Laser Heteroepitaxy of High Quality CdTe Thin Films on Sapphire Substrates". MA thesis. McMaster University, 2013 (cit. on pp. 57, 98).

[29] P. Willmott and J. Huber. "Pulsed laser vaporization and deposition". In: *Reviews of Modern Physics* 72.1 (2000-01), pp. 315–328. ISSN: 0034-6861. DOI: 10.1103/RevModPhys.72.315 (cit. on p. 58).

[30] G. A. Devenyi, S. Y. Woo, S. Ghanad-Tavakoli, R. A. Hughes, R. N. Kleiman, G. A. Botton, and J. S. Preston. "The role of vicinal silicon surfaces in the formation of epitaxial twins during the growth of III-V thin films". In: *Journal of Applied Physics* 110.12 (2011), p. 124316. ISSN: 00218979. DOI: 10.1063/1.3671022 (cit. on pp. 64, 83).

[31] D. B. Holt. "Antiphase boundaries in semiconducting compounds". In: *Journal of Physics and Chemistry of Solids* 30.6 (1969-06), pp. 1297–1308. ISSN: 00223697. DOI: 10.1016/0022-3697(69)90191-7 (cit. on p. 65).

[32] F. Ernst and P. Pirouz. "The formation mechanism of planar defects in compound semiconductors grown epitaxially on {100} silicon substrates". In: *Journal of Materials Research* 4.4 (1989-01), pp. 834–842. ISSN: 0884-2914. DOI: 10.1557/JMR.1989.0834 (cit. on pp. 65, 73).

[33] C. N. J. Wagner. "No Title". In: *Local Atomic Arrangements Studied by X-Ray Diffraction*. Ed. by J. B. Cohen and J. E. Hilliard. New York: Gordon and Breach, 1966, pp. 224–225 (cit. on p. 65).

[34] H. Toyota, T. Sasaki, Y. Jinbo, and N. Uchitomi. "Growth and characterization of GaSb/AlGaSb multi-quantum well structures on Si (001) substrates". In: *Journal of Crystal Growth* 310.1 (2008-01), pp. 78–82. ISSN: 00220248. DOI: 10.1016/j.jcrysgro.2007.10.008 (cit. on p. 65).

[35] Y. H. Kim, J. Y. Lee, Y. G. Noh, M. D. Kim, S. M. Cho, Y. J. Kwon, and J. E. Oh. "Growth mode and structural characterization of GaSb on Si (001) substrate: A transmission electron microscopy study". In: *Applied Physics Letters* 88.24 (2006), p. 241907. ISSN: 00036951. DOI: 10.1063/1.2209714 (cit. on p. 65).

[36] H. Y. Xu, Y. N. Guo, Y. Wang, J. Zou, J. H. Kang, Q. Gao, H. H. Tan, and C. Jagadish. "Effects of annealing and substrate orientation on epitaxial growth of GaAs on Si". In: *Journal of Applied Physics* 106.8 (2009), p. 083514. ISSN: 00218979. DOI: 10.1063/1.3248372 (cit. on p. 65).

[37] Andre Proessdorf, Frank Grosse, Oleksandr Romanyuk, Wolfgang Braun, Bernd Jenichen, Achim Trampert, and Henning Riechert. “Interface engineering for improved growth of GaSb on Si(111)”. In: *Journal of Crystal Growth* 323.1 (2011-12), pp. 401–404. ISSN: 00220248. DOI: 10.1016/j.jcrysgro.2010.11.167 (cit. on p. 65).

[38] R. Fischer, D. Neuman, H. Zabel, H. Morkoç, C. Choi, and N. Otsuka. “Dislocation reduction in epitaxial GaAs on Si(100)”. In: *Applied Physics Letters* 48.18 (1986), pp. 1223–1225. ISSN: 00036951. DOI: 10.1063/1.96988 (cit. on p. 65).

[39] T. Nguyen, W. Varhue, E. Adams, M. Lavoie, and S. Mongeon. “Growth of heteroepitaxial GaSb thin films on Si(100) substrates”. In: *Journal of Materials Research* 19.8 (2004), pp. 2315–2321. ISSN: 0884-2914. DOI: 10.1557/JMR.2004.0307 (cit. on p. 65).

[40] H Noge. “Molecular beam epitaxial growth of a GaAs layer free from antiphase domains on an exactly (100)-oriented Si substrate preheated at 1000°C”. In: *Journal of Crystal Growth* 83.3 (1987-06), pp. 431–436. ISSN: 00220248. DOI: 10.1016/0022-0248(87)90306-X (cit. on p. 65).

[41] A. Vilà, A. Cornet, J. R. Morante, P. Ruterana, M. Loubradou, R. Bonnet, Y. González, and L. González. “Atomic core structure of Lomer dislocations at GaAs/(001)Si interface”. In: *Philosophical Magazine A* 71.1 (1995), pp. 85–103 (cit. on p. 65).

[42] R. Fischer, H. Morkoç, D. a. Neumann, H. Zabel, C. Choi, N. Otsuka, M. Longerbone, and L. P. Erickson. “Material properties of high-quality GaAs epitaxial layers grown on Si substrates”. In: *Journal of Applied Physics* 60.5 (1986), p. 1640. ISSN: 00218979. DOI: 10.1063/1.337253 (cit. on pp. 65, 66, 83).

[43] J. Hornstra. “Models of grain boundaries in the diamond lattice I. Tilt about ”. In: *Physica* 25.1-6 (1959), pp. 409–422. ISSN: 00318914. DOI: 10.1016/S0031-8914(59)94454-4 (cit. on p. 65).

[44] X. L. Wei and M. Aindow. “Development of anisotropic microtwin distributions in GaAs grown on 4°-off (001) Si by molecular beam epitaxy”. In: *Applied*

Physics Letters 65.15 (1994), pp. 1903–1905. ISSN: 00036951. DOI: 10.1063/1.112834 (cit. on pp. 65, 75, 76).

[45] Q. H. Xie, K. K. Fung, A. J. Ding, L. H. Cai, Y. Huang, and J. M. Zhou. “Asymmetric distribution of microtwins in a GaAs/Si heterostructure grown by molecular beam epitaxy”. In: *Applied Physics Letters* 57.26 (1990), pp. 2803–2805. ISSN: 00036951. DOI: 10.1063/1.103792 (cit. on pp. 65, 75).

[46] K. C. Rajkumar, A. Madhukar, J. K. Liu, and F. J. Grunthaner. “Observation of a correlation between twin orientation and substrate step direction in thin GaAs films grown on intentionally misoriented Si (100)”. In: *Applied Physics Letters* 56.12 (1990), p. 1160. ISSN: 00036951. DOI: 10.1063/1.102549 (cit. on p. 65).

[47] Hanne. Neergaard Waltenburg and JT Yates. “Surface Chemistry of Silicon”. In: *Chemical Reviews* 95.5 (1995-07), pp. 1589–1673. DOI: 10.1021/cr00037a600 (cit. on p. 66).

[48] E. Schroder-Bergen and W. Ranke. “Steps on Si (001) vicinal surfaces tilted by various angles in the [1-10]-, [100]- and [2-10]-zones, inv estigated by high-resolution LEED”. In: *Surface Science* 259 (1991), pp. 323–338 (cit. on p. 66).

[49] T. Sakamoto and G. Hashiguchi. “Si (001)-2× 1 Single-Domain Structure Obtained by High Temperature Annealing”. In: *Japanese Journal of Applied* (1986). DOI: 10.1143/JJAP.25.L78 (cit. on p. 66).

[50] K. Akahane, N. Yamamoto, S. Gozu, and N. Ohtani. “Heteroepitaxial growth of GaSb on Si(001) substrates”. In: *Journal of Crystal Growth* 264.1-3 (2004-03), pp. 21–25. ISSN: 00220248 (cit. on pp. 66, 73, 75, 83).

[51] G. Balakrishnan, S. H. Huang, A. Khoshakhlagh, A. Jallipalli, P. Rotella, A. Amtout, S. Krishna, C. P. Haines, L. R. Dawson, and D. L. Huffaker. “Room-temperature optically-pumped GaSb quantum well based VCSEL monolithically grown on Si (100) substrate”. In: *Electronics Letters* 42.6 (2006), pp. 1–2 (cit. on pp. 66, 83).

[52] S. Hosseini Vajargah, M. Couillard, K. Cui, S. Ghanad Tavakoli, B. Robinson, R. N. Kleiman, J. S. Preston, and G. A. Botton. “Strain relief and AlSb buffer layer morphology in GaSb heteroepitaxial films grown on Si as revealed by high-angle annular dark-field scanning transmission electron microscopy”.

In: *Applied Physics Letters* 98.8 (2011), p. 082113. ISSN: 00036951. DOI: 10.1063/1.3551626 (cit. on p. 66).

[53] J. Britten and Weiguang Guan. "MAX3D - Visualization of Reciprocal Space Volumes". In: *Commission on Crystallographic Computing Newsletter* 8.8 (2007), p. 96 (cit. on pp. 67, 84).

[54] S. Y. Woo, S. H. Vajargah, S. Ghanad-Tavakoli, R. N. Kleiman, and G. A. Botton. "Observation of anti-phase boundaries in heteroepitaxy of GaSb thin films grown on Si(001) by transmission electron microscopy". In: *to be submitted* () (cit. on p. 72).

[55] S. F. Fang, K. Adomi, S. Iyer, H. Morkoç, H. Zabel, C. Choi, and N. Otsuka. "Gallium arsenide and other compound semiconductors on silicon". In: *Journal of Applied Physics* 68.7 (1990), R31. ISSN: 00218979. DOI: 10.1063/1.346284 (cit. on pp. 73, 78).

[56] Y.H. Kim, Y.K. Noh, M.D. Kim, J.E. Oh, and K.S. Chung. "Transmission electron microscopy study of the initial growth stage of GaSb grown on Si (001) substrate by molecular beam epitaxy method". In: *Thin Solid Films* 518.8 (2010-02), pp. 2280–2284. ISSN: 00406090. DOI: 10.1016/j.tsf.2009.09.120 (cit. on p. 73).

[57] J. Tersoff, A.D.W. van der Gon, and R. Tromp. "Critical island size for layer-by-layer growth". In: *Physical Review Letters* 72.2 (1994-01), pp. 266–269. ISSN: 0031-9007. DOI: 10.1103/PhysRevLett.72.266 (cit. on p. 73).

[58] Osamu Oda. *Compound Semiconductor Bulk Materials and Characterizations*. Singapore: World Scientific, 2007, p. 556. ISBN: 981-02-1728-5 (cit. on p. 74).

[59] H. Gottschalk, G. Patzer, and H. Alexander. "Stacking fault energy and ionicity of cubic III-V compounds". In: *Physica Status Solidi (a)* 45.1 (1978-01), pp. 207–217. ISSN: 00318965. DOI: 10.1002/pssa.2210450125 (cit. on p. 74).

[60] D. B. Holt and B. G. Yacobi. *Extended Defects in Semiconductors: Electronic Properties, Device Effects and Structures*. Cambridge University Press, 2007 (cit. on p. 74).

[61] R. D. Bringans, M. A. Olmstead, F. A. Ponce, D. K. Biegelsen, B. S. Krusor, and R. D. Yingling. “The effect of a Ga prelayer on the beginning of GaAs epitaxy on Si”. In: *Journal of Applied Physics* 64.7 (1988), pp. 3472–3475 (cit. on p. 75).

[62] R. a. a. Kubiak. “Enhanced sticking coefficients and improved profile control using boron and antimony as coevaporated dopants in Si-MBE”. In: *Journal of Vacuum Science & Technology B: Microelectronics and Nanometer Structures* 3.2 (1985-03), p. 592. ISSN: 0734211X. DOI: 10.1116/1.583142 (cit. on p. 75).

[63] Yukihiro Kiyota and Taroh Inada. “Sticking coefficient of boron and phosphorus on silicon during vapor-phase doping”. In: *Journal of Vacuum Science & Technology A: Vacuum, Surfaces, and Films* 19.5 (2001), p. 2441. ISSN: 07342101. DOI: 10.1116/1.1387055 (cit. on p. 75).

[64] S. Y. Woo, G. A. Devenyi, S. Ghanad-Tavakoli, R. N. Kleiman, J. S. Preston, and G. A. Botton. “Tilted epitaxy on (211)-oriented substrates”. In: *Applied Physics Letters* 102.13 (2013), p. 132103. ISSN: 00036951. DOI: 10.1063/1.4799278 (cit. on p. 82).

[65] S. L. Wright, M. Inada, and H. Kroemer. “Polar-on-nonpolar epitaxy: Sublattice ordering in the nucleation and growth of GaP on Si(211) surfaces”. en. In: *Journal of Vacuum Science and Technology* 21.2 (1982-07), p. 534. ISSN: 00225355. DOI: 10.1116/1.571755 (cit. on pp. 82, 83).

[66] W. F. Zhao, R. N. Jacobs, M. Jaime-Vasquez, L. O. Bubulac, and D. J. Smith. “Microstructural Characterization of CdTe(211)B/ZnTe/Si(211) Heterostructures Grown by Molecular Beam Epitaxy”. In: *Journal of Electronic Materials* 40.8 (2011-06), pp. 1733–1737. ISSN: 0361-5235. DOI: 10.1007/s11664-011-1673-2 (cit. on pp. 83, 90, 91).

[67] X. J. Wang, Y. Chang, C. R. Becker, C. H. Grein, S. Sivananthan, and R. Kodama. “Microstructure of Heteroepitaxial ZnTe Grown by Molecular Beam Epitaxy on Si(211) Substrates”. In: *Journal of Electronic Materials* 40.8 (2011-05), pp. 1860–1866. ISSN: 0361-5235. DOI: 10.1007/s11664-011-1648-3 (cit. on pp. 83, 90, 91).

[68] N. K. Dhar, M. Zandian, J. G. Pasko, J. M. Arias, and J. H. Dinan. “Planar p-on-n HgCdTe heterostructure infrared photodiodes on Si substrates by molecular beam epitaxy”. In: *Applied Physics Letters* 70.13 (1997), p. 1730. ISSN: 00036951. DOI: 10.1063/1.118683 (cit. on pp. 83, 91).

[69] Y.-Z. Wang, L. Chen, Y. Wu, J. Wu, M.-F. Yu, and L. He. “Heteroepitaxy of CdTe on tilting Si(211) substrates by molecular beam epitaxy”. In: *Journal of Crystal Growth* 290.2 (2006-05), pp. 436–440. ISSN: 00220248. DOI: 10.1016/j.jcrysgro.2006.01.048 (cit. on p. 83).

[70] M. D. Lange, R. Sporken, K. K. Mahavadi, J. P. Faurie, Y. Nakamura, and N. Otsuka. “Molecular beam epitaxy and characterization of CdTe(211) and CdTe(133) films on GaAs(211)B substrates”. In: *Applied Physics Letters* 58.18 (1991), p. 1988. ISSN: 00036951. DOI: 10.1063/1.105041 (cit. on pp. 83, 85, 91).

[71] Y. Nakamura, N. Otsuka, M. D. Lange, R. Sporken, and J. P. Faurie. “Origin of dual epitaxy in the growth of CdTe on (211) GaAs”. In: *Applied Physics Letters* 60.11 (1992), p. 1372. ISSN: 00036951. DOI: 10.1063/1.107294 (cit. on p. 83).

[72] G. H. Olsen and R. T. Smith. “Misorientation and tetragonal distortion in heteroepitaxial vapor-Grown III-V structures”. In: *Physica Status Solidi (a)* 31.2 (1975-10), pp. 739–747. ISSN: 00318965. DOI: 10.1002/pssa.2210310247 (cit. on p. 83).

[73] Ferenc Riesz. “Rotated tilting in lattice-mismatched heteroepitaxial systems”. In: *Journal of Crystal Growth* 140.1-2 (1994-06), pp. 213–218. ISSN: 00220248. DOI: 10.1016/0022-0248(94)90515-0 (cit. on p. 83).

[74] J. E. Ayers, S. K. Ghandhi, and L. J. Schowalter. “Crystallographic tilting of heteroepitaxial layers”. In: *Journal of Crystal Growth* 113.3-4 (1991-09), pp. 430–440. ISSN: 00220248. DOI: 10.1016/0022-0248(91)90077-I (cit. on p. 83).

[75] S.M. Johnson, J.B. James, W.L. Ahlgren, W.J. Hamilton, M. Ray, and G.S. TOMPA. “Heteroepitaxial HgCdTe/CdZnTe/GaAs/Si Materials for Infrared Focal Plane Arrays”. In: *MRS Proceedings* 216 (1990-02). Ed. by A. Katz,

R. M. Biefld, R. L. Gunshor, and R. J. Malik, p. 141. ISSN: 1946-4274. DOI: 10.1557/PROC-216-141 (cit. on pp. 83, 85, 90, 91).

[76] T. Sasaki. "Study of CdTe epitaxial growth on (211)B GaAs by molecular-beam epitaxy". In: *Journal of Vacuum Science & Technology B: Microelectronics and Nanometer Structures* 10.4 (1992-07), p. 1399. ISSN: 0734211X. DOI: 10.1116/1.585875 (cit. on p. 83).

[77] L. Li. "A basic factor of dual epitaxy: the symmetry of similarity of zinc blende structure". In: *Acta Crystallographica Section A Foundations of Crystallography* 51.6 (1995-11), pp. 902–909. ISSN: 0108-7673. DOI: 10.1107/S0108767395008014 (cit. on p. 83).

[78] S. Rujirawat, D. J. Smith, J. P. Faurie, G. Neu, V. Nathan, and S. Sivananthan. "Microstructural and Optical Characterization of CdTe (211)B/ZnTe/Si (211) Grown by Molecular Beam Epitaxy". In: *Journal of Electronic Materials* 27.9 (1998), pp. 1047–1052 (cit. on p. 83).

[79] K.-C. Kim, H. J. Kim, S.-H. Suh, M. Carmody, S. Sivananthan, and J.-S. Kim. "Metalorganic Chemical Vapor Deposition of CdTe(133) Epilayers on Si(211) Substrates". In: *Journal of Electronic Materials* 39.7 (2010-04), pp. 863–867. ISSN: 0361-5235. DOI: 10.1007/s11664-010-1220-6 (cit. on p. 85).

[80] T. J. de Lyon, D. Rajavel, S. M. Johnson, and C. A. Cockrum. "Molecular-beam epitaxial growth of CdTe(112) on Si(112) substrates". In: *Applied Physics Letters* 66.16 (1995), p. 2119. ISSN: 00036951. DOI: 10.1063/1.113922 (cit. on p. 85).

[81] S. Y. Woo, S. Hosseini Vajargah, S. Ghanad-Tavakoli, R. N. Kleiman, and G. A. Botton. "Direct observation of anti-phase boundaries in heteroepitaxy of GaSb thin films grown on Si(001) by transmission electron microscopy". In: *Journal of Applied Physics* 112.7 (2012), p. 074306. ISSN: 00218979. DOI: 10.1063/1.4756957 (cit. on p. 85).

[82] S. Hosseini Vajargah, S. Ghanad-Tavakoli, J. S. Preston, G. A. Botton, and R. N. Kleiman. "Lattice-registered growth of GaSb on Si (211) with molecular beam epitaxy". In: *Journal of Applied Physics* 112.9 (2012), p. 093103. ISSN: 00218979. DOI: 10.1063/1.4761970 (cit. on p. 87).

[83] D. J. Smith, J. J. Kim, M. R. McCartney, and T Aoki. "Atomic-Scale Characterization of II-VI Compound Semiconductors". In: *2012 U.S. Workshop on the Physics and Chemistry of II-VI Materials*. 2012 (cit. on pp. 90, 91).

[84] J. J. Kim, D. J. Smith, R. N. Jacobs, L. A. Almeida, M. Jamie-Vasquez, C. Nozaki, J. K. Markunas, and J. D. Benson. "TEM Characterization of HgCdTe/CdTe Grown on GaAs(211)B Substrates". In: *2012 U.S. Workshop on the Physics and Chemistry of II-VI Materials*. 2012 (cit. on p. 90).

[85] R. Triboulet and P. Siffert. *CdTe and Related Compounds - Physics, Defects, Technology, Hetero - And Nanostructures and Applications: Crystal Growth, Surfaces and Applications*. Elsevier, 2009, p. 104 (cit. on p. 91).

[86] F. Yu. "Tilt angles at the CdTe/CdZnTe, HgCdTe/ CdTe, CdTe/GaAs heterojunctions grown by molecular beam epitaxy". In: *Journal of Crystal Growth* 204 (1999), pp. 35–40 (cit. on p. 91).

[87] S Neretina, RA Hughes, GA Devenyi, NV Sochinskii, JS Preston, and P Mascher. "Atypical grain growth for (2 1 1) CdTe films deposited on surface reconstructed (1 0 0) SrTiO3 substrates". In: *Applied Surface Science* 255.11 (2009), pp. 5674–5681. ISSN: 0169-4332. DOI: 10.1016/j.apsusc.2008.12.050 (cit. on pp. 96, 108, 145).

[88] S. Neretina, R A Hughes, G A Devenyi, N V Sochinskii, J S Preston, and P Mascher. "The role of substrate surface alteration in the fabrication of vertically aligned CdTe nanowires". In: *Nanotechnology* 19.18 (2008-05), p. 185601. ISSN: 0957-4484. DOI: 10.1088/0957-4484/19/18/185601 (cit. on pp. 96, 120).

[89] S. Neretina, RA Hughes, JF Britten, NV Sochinskii, JS Preston, and P. Mascher. "The role of substrate surface termination in the deposition of (111) CdTe on (0001) sapphire". In: *Applied Physics A: Materials Science & Processing* 96.2 (2009), pp. 429–433. ISSN: 0947-8396. DOI: 10.1007/s00339-009-5285-0 (cit. on pp. 96, 97).

[90] S Neretina, R a Hughes, J F Britten, N V Sochinskii, J S Preston, and P Mascher. "Vertically aligned wurtzite CdTe nanowires derived from a catalytically driven growth mode". In: *Nanotechnology* 18.27 (2007-07), p. 275301. ISSN: 0957-4484. DOI: 10.1088/0957-4484/18/27/275301 (cit. on p. 96).

[91] S. Neretina, Q. Zhang, R. a. Hughes, J. F. Britten, N. V. Sochinskii, J. S. Preston, and P. Mascher. "The role of lattice mismatch in the deposition of CdTe thin films". In: *Journal of Electronic Materials* 35.6 (2006-06), pp. 1224–1230. ISSN: 0361-5235. DOI: 10.1007/s11664-006-0245-3 (cit. on pp. 96, 110).

[92] S. M. Jovanovic, G. A. Devenyi, V. M. Jarvis, C. M. Haapamaki, M. Gerber, R. R. LaPierre, and J. S. Preston. "Optical Properties of High Quality Epitaxial CdTe Thin Films on Al2O3 (0001) Substrates". In: *Solar Energy Materials and Solar Cells* SOLMAT-D-13-01231 () (cit. on p. 96).

[93] G. A. Devenyi, S. M. Jovanovic, and J. S. Preston. *ARBITRARILY THIN ULTRA SMOOTH FILM WITH BUILT-IN SEPARATION ABILITY AND METHOD OF FORMING THE SAME.* 2012 (cit. on p. 96).

[94] M D Lange, R Sporken, K K Mahavadi, J P Faurie, Y Nakamura, and N. Otsuka. "Molecular beam epitaxy and characterization of CdTe(211) and CdTe(133) films on GaAs(211)B substrates". In: *Applied Physics Letters* 58.18 (1991), p. 1988. ISSN: 00036951. DOI: 10.1063/1.105041 (cit. on p. 111).

[95] a. Million, N.K. Dhar, and J.H. Dinan. "Heteroepitaxy of CdTe on {211}Si substrates by molecular beam epitaxy". In: *Journal of Crystal Growth* 159.1-4 (1996-02), pp. 76–80. ISSN: 00220248. DOI: 10.1016/0022-0248(95)00777-6 (cit. on p. 111).

[96] S. Rujirawat, L. a. Almeida, Y. P. Chen, S. Sivananthan, and David J. Smith. "High quality large-area CdTe(211)B on Si(211) grown by molecular beam epitaxy". In: *Applied Physics Letters* 71.13 (1997), p. 1810. ISSN: 00036951. DOI: 10.1063/1.119406 (cit. on p. 111).

[97] J.P. Zanatta, P. Ferret, P. Duvaut, S. Isselin, G. Theret, G. Rolland, and a. Million. "Heteroepitaxy of CdTe on Ge(2 1 1) substrates by molecular beam epitaxy". In: *Journal of Crystal Growth* 184-185 (1998-02), pp. 1297–1301. ISSN: 00220248. DOI: 10.1016/S0022-0248(98)80269-8 (cit. on p. 111).

[98] Martin R. Castell. "Scanning tunneling microscopy of reconstructions on the SrTiO3(001) surface". In: *Surface Science* 505 (2002-05), pp. 1–13. ISSN: 00396028. DOI: 10.1016/S0039-6028(02)01393-6 (cit. on p. 113).

[99] Qidu Jiang and Jörg Zegenhagen. "SrTiO3(001)-c(6 × 2): a long-range, atomically ordered surface stable in oxygen and ambient air". In: *Surface Science* 367.2 (1996-11), pp. L42–L46. ISSN: 00396028. DOI: 10.1016/S0039-6028(96)00990-9 (cit. on pp. 114, 116).

[100] HJ Gossmann and LC Feldman. "Initial stages of silicon molecular-beam epitaxy: Effects of surface reconstruction". In: *Physical Review B* 32.1 (1985-07), pp. 6–11. ISSN: 0163-1829. DOI: 10.1103/PhysRevB.32.6 (cit. on p. 117).

[101] Fabien Silly and Martin R Castell. "Selecting the Shape of Supported Metal Nanocrystals: Pd Huts, Hexagons, or Pyramids on $SrTiO3(001)$". In: *Physical Review Letters* 94.4 (2005-02), p. 46103. DOI: 10.1103/PhysRevLett.94.046103 (cit. on p. 118).

[102] S Neretina, R a Hughes, J F Britten, N V Sochinskii, J S Preston, and P Mascher. "Vertically aligned wurtzite CdTe nanowires derived from a catalytically driven growth mode". In: *Nanotechnology* 18.27 (2007-07), p. 275301. ISSN: 0957-4484. DOI: 10.1088/0957-4484/18/27/275301 (cit. on pp. 120, 121).

[103] a. Raab and G. Springholz. "Oswald ripening and shape transitions of self-assembled PbSe quantum dots on PbTe (111) during annealing". In: *Applied Physics Letters* 77.19 (2000), p. 2991. ISSN: 00036951. DOI: 10.1063/1.1323733 (cit. on p. 126).

[104] B. Q. Li and J. M. Zuo. "Self-assembly of epitaxial Ag nanoclusters on H-terminated Si(111) surfaces". In: *Journal of Applied Physics* 94.1 (2003), p. 743. ISSN: 00218979. DOI: 10.1063/1.1581341 (cit. on p. 126).

[105] Bennett L H Massalski T B, Murray J L and Baker H. *Binary Alloy Phase Diagrams*. Metals Park, OH: American Society for Metals, 1986 (cit. on p. 127).

[106] L. Schubert, P. Werner, N. D. Zakharov, G. Gerth, F. M. Kolb, L. Long, U. Gosele, and T. Y. Tan. "Silicon nanowhiskers grown on <111>Si substrates by molecular-beam epitaxy". In: *Applied Physics Letters* 84.24 (2004), p. 4968. ISSN: 00036951. DOI: 10.1063/1.1762701 (cit. on p. 128).

[107] Yiying Wu, Rong Fan, and Peidong Yang. "Block-by-Block Growth of Single-Crystalline Si/SiGe Superlattice Nanowires". In: *Nano Letters* 2.2 (2002-02), pp. 83–86. ISSN: 1530-6984. DOI: 10.1021/nl0156888 (cit. on p. 128).

[108] Dimo Kashchiev. "Dependence of the Growth Rate of Nanowires on the Nanowire Diameter". In: *Crystal Growth & Design* 6.5 (2006-05), pp. 1154–1156. ISSN: 1528-7483. DOI: 10.1021/cg050619i (cit. on p. 128).

[109] Zhuo Chen and Chuanbao Cao. "Effect of size in nanowires grown by the vapor-liquid-solid mechanism". In: *Applied Physics Letters* 88.14 (2006), p. 143118. ISSN: 00036951. DOI: 10.1063/1.2193051 (cit. on p. 128).

[110] C. Ratsch, J. Garcia, and R. E. Caflisch. "Influence of edge diffusion on the growth mode on vicinal surfaces". In: *Applied Physics Letters* 87.14 (2005), p. 141901. ISSN: 00036951. DOI: 10.1063/1.2077851 (cit. on p. 129).

[111] Shunji Watanabe. "Cleaning the surface of SrTiO3(100) and LaAlO3(100) under moderate temperature condition by Bi adsorption/desorption treatment". In: *Journal of Vacuum Science & Technology A: Vacuum, Surfaces, and Films* 9.4 (1991-07), p. 2394. ISSN: 07342101. DOI: 10.1116/1.577283 (cit. on p. 130).

[112] R. Sporken, D. Grajewski, Y. Xin, F. Wiame, G. Brill, P. Boieriu, a. Prociuk, S. Rujirawat, N. K. Dhar, and S. Sivananthan. "Selective epitaxy of cadmium telluride on silicon by MBE". In: *Journal of Electronic Materials* 29.6 (2000-06), pp. 760–764. ISSN: 0361-5235. DOI: 10.1007/s11664-000-0221-2 (cit. on p. 130).

[113] R. Zhang and I. Bhat. "Atomic force microscopy studies of CdTe films grown by epitaxial lateral overgrowth". In: *Journal of Electronic Materials* 30.11 (2001-11), pp. 1370–1375. ISSN: 0361-5235. DOI: 10.1007/s11664-001-0185-x (cit. on p. 130).

[114] Ishwara Bhat and Ruichao Zhang. "Anisotropy in selective metalorganic vapor phase epitaxy of CdTe on GaAs and Si substrates". In: *Journal of Electronic Materials* 35.6 (2006-06), pp. 1293–1298. ISSN: 0361-5235. DOI: 10.1007/s11664-006-0257-z (cit. on p. 130).

[115] U. Krishnamachari, M. Borgstrom, B. J. Ohlsson, N. Panev, L. Samuelson, W. Seifert, M. W. Larsson, and L. R. Wallenberg. "Defect-free InP nanowires grown in [001] direction on InP (001)". In: *Applied Physics Letters* 85.11 (2004), p. 2077. ISSN: 00036951. DOI: 10.1063/1.1784548 (cit. on p. 131).

[116] a Mikkelsen, J Eriksson, E Lundgren, J N Andersen, J Weissenreider, and W Seifert. "The influence of lysine on InP(001) surface ordering and nanowire growth". In: *Nanotechnology* 16.10 (2005-10), pp. 2354–2359. ISSN: 0957-4484. DOI: 10.1088/0957-4484/16/10/060 (cit. on p. 131).

[117] T. Mårtensson, J. B. Wagner, E. Hilner, a. Mikkelsen, C. Thelander, J. Stangl, B. J. Ohlsson, a. Gustafsson, E. Lundgren, L. Samuelson, and W. Seifert. "Epitaxial Growth of Indium Arsenide Nanowires on Silicon Using Nucleation Templates Formed by Self-Assembled Organic Coatings". In: *Advanced Materials* 19.14 (2007-07), pp. 1801–1806. ISSN: 09359648. DOI: 10.1002/adma.200700285 (cit. on p. 131).

[118] M. Copel, M. C. Reuter, Efthimios Kaxiras, and R. M. Tromp. "Surfactants in epitaxial growth". In: *Phys. Rev. Lett.* 63 (6 1989-08), pp. 632–635. DOI: 10.1103/PhysRevLett.63.632. URL: http://link.aps.org/doi/10.1103/PhysRevLett.63.632 (cit. on p. 131).

[119] Gabriel A Devenyi, Jianfeng Li, Robert A Hughes, An-Chang Shi, Peter Mascher, and John S Preston. "Epitaxially driven formation of intricate supported gold nanostructures on a lattice-matched oxide substrate". In: *Nano letters* 9.12 (2009-12), pp. 4258–63. ISSN: 1530-6992. DOI: 10.1021/nl902491g (cit. on p. 136).

[120] Cyril Isenberg. *The Science of Soap Films and Soap Bubbles*. English. New edition. Mineola, N.Y.: Dover Publications, 1992-01-24, p. 220. ISBN: 0486269604 (cit. on p. 140).

[121] Gerald Lim H. W., Michael Wortis, and Ranjan Mukhopadhyay. "Stomatocyte–discocyte–echinocyte sequence of the human red blood cell: Evidence for the bilayer– couple hypothesis from membrane mechanics". In: *Proceedings of the National Academy of Sciences of the United States of America* 99.26 (2002-12), pp. 16766–16769 (cit. on pp. 140, 141).

[122] Udo Seifert. "Configurations of fluid membranes and vesicles". In: *Advances in Physics* 46.1 (1997), p. 13 (cit. on p. 140).

[123] W. Helfrich. "Elastic properties of lipid bilayers: theory and possible experiments". eng. In: *Zeitschrift fur Naturforschung.Teil C: Biochemie, Biophysik, Biologie, Virologie* 28.11 (1973-11), pp. 693–703 (cit. on p. 140).

[124] Ranjan Mukhopadhyay, H. W. Gerald Lim, and Michael Wortis. *Echinocyte Shapes: Bending, Stretching, and Shear Determine Spicule Shape and Spacing*. 2002-04/01. DOI: 10.1016/S0006-3495(02)75527-6 (cit. on pp. 140, 141).

[125] Gerhard Gompper and Michael Schick. *Soft Matter: Volume 4: Lipid Bilayers and Red Blood Cells*. English. Wiley-VCH, 2008-09-09, p. 265. ISBN: 3527315020 (cit. on pp. 140, 141).

[126] Marcel Bessis. *Corpuscles: Atlas of red blood cell shapes*. Berlin and New York: Springer-Verlag, 1974, p. 121 (cit. on p. 140).

[127] Zhong-can Ou-Yang and W. Helfrich. "Instability and Deformation of a Spherical Vesicle by Pressure". In: *Physical Review Letters* 59.21 (1987-11/23), p. 2486. DOI: 10.1103/PhysRevLett.59.2486 (cit. on p. 141).

[128] Zhong-can Ou-Yang and Wolfgang Helfrich. "Bending energy of vesicle membranes: General expressions for the first, second, and third variation of the shape energy and applications to spheres and cylinders". In: *Physical Review A* 39.10 (1989-05/15), p. 5280. DOI: 10.1103/PhysRevA.39.5280 (cit. on p. 141).

[129] Richard S. Millman and George D. Parker. *Elements of differential geometry*. Englewood Cliffs, N.J.: Prentice-Hall, 1977, p. 265. ISBN: 0132641437 (cit. on p. 141).

[130] Takashi Taniguchi. "Shape Deformation and Phase Separation Dynamics of Two-Component Vesicles". In: *Physical Review Letters* 76.23 (1996-06/03), p. 4444. DOI: 10.1103/PhysRevLett.76.4444 (cit. on p. 141).

[131] Kenneth A. Brakke. "The Surface Evolver". In: *Experimental Mathematics* 1.2 (1992) (cit. on p. 141).

[132] Frank Jülicher. "The Morphology of Vesicles of Higher Topological Genus: Conformal Degeneracy and Conformal Modes". In: *Journal de Physique II* 6.12 (1996-12), pp. 1797–1824. DOI: 10.1051/jp2:1996161 (cit. on p. 141).

[133] Fabien Silly and Martin R. Castell. "Fe nanocrystal growth on SrTiO[sub 3](001)". In: *Applied Physics Letters* 87.6 (2005-8 August 2005), p. 063106 (cit. on p. 145).

[134] F. Silly and M. R. Castell. "Growth of Ag icosahedral nanocrystals on a SrTiO3(001) support". In: *Applied physics letters* 87.21 (2005) (cit. on p. 145).

[135] F. Silly and M. R. Castell. "Temperature-dependent stability of supported five-fold twinned copper nanocrystals". eng. In: *ACS nano* 3.4 (2009-04), pp. 901–906 (cit. on p. 145).

[136] P. Buffat and J. P. Borel. "Size effect on the melting temperature of gold particles". In: *Physical Review A (General Physics)* 13.6 (1976), pp. 2287–2298 (cit. on p. 145).

[137] Svetlana V. Yanina and C. Barry Carter. "Terraces and ledges on (0 0 1) spinel surfaces". In: *Surface Science* 513.2 (2002-7), pp. L402–L412 (cit. on p. 145).

[138] Tahereh Majdi. "Novel Self-assembly of Crystalline MgAl2O4 Nanostructures Promoted by Annealing a Gold Overlayer on a (111) MgAl2O4 Substrate". MA thesis. McMaster University, 2013 (cit. on p. 154).

Appendix A

Lattice Matching Calculations

```
function abcf = lattice_checker(film_file, substrate_file)
%Lattice Checker Program, inputs two files of lists of names,
  crystal groups and lattice constants, and outpus fixes within tol
   mistmach
%Written by Gabriel A. Devenyi
%August 10, 2013
tol = 8;
%command_line=argv();
%film_file = command_line(1,1);
%substrate_file = command_line(2,1);


fid = fopen (substrate_file, 'r');
i = 1;
sub_name = char(zeros(10,100));
sub_type = char(zeros(1,100));

while (~feof(fid))
    [a, sub_type(i), sub_a(i), sub_c(i)] = fscanf (fid, '%s␣%s␣%f␣%
      f', 'C');
    sub_name(i,1:length(a)) = a;
    i=i+1;
end

fclose (fid);

fid = fopen (film_file, 'r');
```

```
i = 1;
film_name = char(zeros(10,100));
film_type = char(zeros(1,100));

while (~feof(fid))
    [a, film_type(i), film_a(i), film_c(i)] = fscanf (fid, '%s␣%s␣%
      f␣%f', 'C');
    film_name(i,1:length(a)) = a;
    i = i + 1;
end

fclose (fid);
disp(sprintf('Film,Symmetry,Substrate,Symmetry,Mismatch(%%),Rounded
  ␣Ratio,Original␣Ratio'));
%Iterate through Substrates
for i=1:length(sub_a)

    %Iterate through Films
    for j=1:length(film_a)
        if (strtrim(film_name(j,:)) == strtrim(sub_name(i,:)))
            continue;
        end
        %Cubic on Cubic Check
        if (film_type(j) == 'C' && sub_type(i) == 'C')
            original_ratio = sub_a(i)/film_a(j);

            if (original_ratio < 1)
                ratio = 1/round(1/original_ratio);
            else
                ratio = round(original_ratio);
            end

            %(sub_a(i) - ratio*film_a(j))/(ratio*film_a(j)) * 100;
            (ratio*film_a(j) - sub_a(i)) / sub_a(i) *100;
            if (abs(ans) < tol)
                disp(sprintf('%s,C,%s,C,%g,%g,%g',strtrim(film_name
                  (j,:)), strtrim(sub_name(i,:)), ans, ratio,
                  original_ratio));
            end
        end
```

```
%Cubic on Hexagonal
if (film_type(j) == 'C' && sub_type(i) == 'H')
    original_ratio = sub_a(i)/(film_a(j)*sqrt(2));

    if (original_ratio < 1);
        ratio = 1/round(1/original_ratio);
    else
        ratio = round(original_ratio);
    end

    %(sub_a(i) - ratio*film_a(j)*sqrt(2))/(ratio*film_a(j)*
      sqrt(2)) * 100;
    (ratio*film_a(j)*sqrt(2) - sub_a(i)) / sub_a(i) * 100;
    if (abs(ans) < tol)
        disp(sprintf('%s,C,%s,H,%g,%g,%g',strtrim(film_name
          (j,:)), strtrim(sub_name(i,:)), ans, ratio,
          original_ratio));
    end
end

%Tetragonal on Cubic Check
if (film_type(j) == 'T' && sub_type(i) == 'C')
    original_ratio = sub_a(i)/film_a(j);

    if (original_ratio < 1)
        ratio = 1/round(1/original_ratio);
    else
        ratio = round(original_ratio);
    end

    %(sub_a(i) - ratio*film_a(j))/(ratio*film_a(j)) * 100;
    (ratio*film_a(j) - sub_a(i)) / sub_a(i) *100;
    if (abs(ans) < tol)
        disp(sprintf('%s,T,%s,C,%g,%g,%g',strtrim(film_name
          (j,:)), strtrim(sub_name(i,:)), ans, ratio,
          original_ratio));
    end
end

%Hexagonal on Hexagonal Check
if (film_type(j) == 'H' && sub_type(i) == 'H')
```

```
        original_ratio = sub_a(i)/film_a(j);

        if (original_ratio < 1)
            ratio = 1/round(1/original_ratio);
        else
            ratio = round(original_ratio);
        end

        %(sub_a(i) - ratio*film_a(j))/(ratio*film_a(j)) * 100;
        (ratio*film_a(j) - sub_a(i)) / sub_a(i) *100;
        if (abs(ans) < tol)
            disp(sprintf('%s,H,%s,H,%g,%g,%g',strtrim(film_name
              (j,:)), strtrim(sub_name(i,:)), ans, ratio,
              original_ratio));
        end
    end

    %Hexagonal on Cubic Check
    if (film_type(j) == 'H' && sub_type(i) == 'C')
        original_ratio = (sub_a(i)*sqrt(2))/film_a(j);

        if (original_ratio < 1)
            ratio = 1/round(1/original_ratio);
        else
            ratio = round(original_ratio);
        end

        %(sub_a(i)*sqrt(2) - ratio*film_a(j))/(ratio*film_a(j))
           * 100;
        (ratio*film_a(j) - sub_a(i)*sqrt(2))/(sub_a(i)*sqrt(2))
           * 100;
        if (abs(ans) < tol)
            disp(sprintf('%s,H,%s,C,%g,%g,%g',strtrim(film_name
              (j,:)), strtrim(sub_name(i,:)), ans, ratio,
              original_ratio));
        end
    end

    %Cubic on Tetragonal Check
    if (film_type(j) == 'C' && sub_type(i) == 'T')
        original_ratio = (sub_a(i))/film_a(j);
```

```
                if (original_ratio < 1)
                    ratio = 1/round(1/original_ratio);
                else
                    ratio = round(original_ratio);
                end

                (sub_a(i) - ratio*film_a(j))/(ratio*film_a(j)) * 100;
                if (abs(ans) < tol)
                    disp(sprintf('%s,C,%s,T,%g,%g,%g',strtrim(film_name
                      (j,:)), strtrim(sub_name(i,:)), ans, ratio,
                      original_ratio));
                end
            end

            %Tetragonal on Tetragonal Check
            if (film_type(j) == 'T' && sub_type(i) == 'T')
                original_ratio = (sub_a(i))/film_a(j);

                if (original_ratio < 1)
                    ratio = 1/round(1/original_ratio);
                else
                    ratio = round(original_ratio);
                end

                %(sub_a(i) - ratio*film_a(j))/(ratio*film_a(j)) * 100;
                (ratio*film_a(j) - sub_a(i)) / sub_a(i) *100;
                if (abs(ans) < tol)
                    disp(sprintf('%s,T,%s,T,%g,%g,%g',strtrim(film_name
                      (j,:)), strtrim(sub_name(i,:)), ans, ratio,
                      original_ratio));
                end
            end
        end

    end
```